Università Degli Studi Di Salerno

Facoltà Di Scienze Matematiche, Fisiche, Chimiche E Naturali
Dottorato Di Ricerca In Fisica, Ciclo VI Nuova Serie

PhD Thesis

Development and construction of a Time Of Flight(TOF) system for charged hadron identification in ALICE at LHC

Daniele De Gruttola

Advisor:
Prof. **S. De Pasquale**

PhD Coordinator:
Prof. **G. Vilasi**

Salerno, 2007

Contents

Introductioniii

1 Heavy Ion Physics **1**
- 1.1 QCD 2
  - 1.1.1 QCD Phase Diagram 5
  - 1.1.2 Colour Deconfinement and Chiral Symmetry Restoration 8
  - 1.1.3 The Equation of State 13
- 1.2 QCD Matter in Relativistic Heavy-Ion Collisions 16
  - 1.2.1 Evolution of the Collision 17
- 1.3 QGP Signatures 22
  - 1.3.1 Kinematic Probes 23
  - 1.3.2 Probes of Deconfinement 29
  - 1.3.3 Jet Quenching 35
  - 1.3.4 Elliptic Flow 37
  - 1.3.5 Hanbury-Brown-Twiss Source Radii . . . 40
- 1.4 RHIC Results and Last Models: from QGP to sQGP 42

2 ALICE and the Time Of Flight (TOF) system **46**
- 2.1 A Large Ion Collider Experiment 48
- 2.2 The ALICE Layout 49
  - 2.2.1 Inner Tracking System - ITS 51
  - 2.2.2 Time Projection Chamber - TPC 52
  - 2.2.3 Transition Radiation Detector - TRD . . 53

2.2.4 Time Of Flight - TOF 54
2.2.5 High Momentum Particle Identification Detector - HMPID 56
2.2.6 PHOton Spectrometer - PHOS 56
2.2.7 Forward Detectors 57
2.2.8 ALICE COsmic Rays DEtector - ACORDE 60
2.2.9 Magnet 61
2.3 Particle Identification and Time Of Flight technique 61
2.4 An overview of the TOF detector of the ALICE experiment 65
2.4.1 TOF system 65
2.4.2 Multigap Resistive Plate Chamber 70

3 Configuration of MRPC for the Time Of Flight 80
3.1 Multigap RPC 81
3.1.1 Geometry of MRPC 81
3.1.2 Charge Spectrum 84
3.2 Electronics 87
3.2.1 Front-End Electronics 87
3.2.2 Read-Out Electronics 92
3.3 Some results from beam tests 100
3.3.1 Beam Tests in 2002 101
3.3.2 Beam Tests in 2006 105

4 From the Strips to the Supermodules 110
4.1 Construction of a double-stack MRPC 110
4.1.1 Tests performed on the strips 114
4.2 Modules with MRPCs inside 120
4.2.1 Tests performed on the modules 120
4.3 Supermodules 123
4.3.1 Assembling of a Supermodule 125

4.3.2 Tests before the assembling of the Supermodule 126
4.3.3 Tests on the Supermodule 129
4.3.4 Tests on the FEACs 135
4.4 Commissioning in the magnet 141
4.4.1 First steps of commissioning 142
4.4.2 Fibres and connectors 143
4.4.3 DDL Layout 146

5 A Study on the Pad Clusters Using First Cosmic Muon DATA 149
5.1 Cosmic Rays Run 149
5.2 Reconstruction 155
5.3 New Clusterization Algorithm for TOF Signals . 158
5.3.1 Analysis 164
5.4 Conclusion 168

A Macro for the fit performed with the method of the weighted mean 173
. . . .

Introduction

In the last decades the High Energy Physics has been continuosly developing through the construction of new big accelerators. In particular, in the new ultrarelativistic heavy-ion experiments a very high centre of mass energy is reachable, so that it's possible to explore new regimes, in term of achievable energy densities, of temperature of the system created in the collisions and of available phase-space regions. The Large Hadron Collider (LHC) represents an accelerator machine able to probe deeper into matter than ever before. It will ultimately collide beams of protons at an energy of 14 TeV. Beams of lead nuclei will be also accelerated, smashing together with a collision energy of 5.5 TeV per nucleon pair in the center-of-mass. Four huge detectors, located in the CERN sites, ALICE, ATLAS, CMS and LHCb, will observe the collisions in order to explore Physics at the TeV scale and to look for evidence of Physics beyond the Standard Model.

Crucial problems which will be addressed at the LHC are the connection between phase transitions involving elementary quantum fields, fundamental symmetries of nature and the origin of mass. The experimental programme at the LHC involves the aspects of the symmetry-breaking mechanism through complementary experimental approaches. ATLAS and CMS will search for the Higgs particle, which generates the mass of the electroweak gauge bosons and the bare mass of elementary fermions through spontaneous breaking of the electroweak gauge symmetry. LHCb, focusing on precision measurements with heavy b quarks, will study CP-symmetry-violating processes. ALICE will study the physics of strongly interacting matter at extreme energy densities, where the formation of a new phase of matter, the Quark Gluon Plasma (QGP), is expected. This could be the state of matter that characterized the early stages of Universe, 10^{-5} s after the Big Bang. The QGP should result from a phase transition ordinary matter is expected to undergo when driven to extremely high temperature and energies densities. It's a state in which quarks and gluons are thought to interact freely, not bound to form colour-singlet hadrons and presumably with the quark bare masses restored. Looking at the data from the Relativistic Heavy Ion Collider, it is possible to conclude that the medium created is not the expected QGP, but a strongly coupled or strongly interacting QGP (sQGP). Through this work, the expected signatures of the creation of QGP will be described.

The ALICE Collaboration is presently building a dedicated heavy-ion collisions detector to exploit the unique physics potential of nucleus-nucleus interactions at LHC energies. The aim is to study the role of chiral symmetry in the generation of mass in composite particles (hadrons) using heavy-ion collisions to attain high-energy densities over large volumes and long timescales. ALICE will investigate equilibrium as well as non-equilibrium physics of strongly interacting matter in the energy density regime $\sim 1 - 1000 GeV fm^{-3}$. In addition, the aim is to gain insight into the physics of parton densities close to phase-space saturation, and their collective dynamical evolution towards hadronization (confinement) in a dense nuclear environment. In this way, one also expects to gain further insight into the structure of the QCD phase diagram and the properties of the QGP phase. Then the existence of such a phase and its properties are key issues in QCD for the understanding of confinement and of chiral-symmetry restoration. For this purpose, it's necessary to carry out a comprehensive study of the hadrons, electrons, muons and photons produced in the collision of heavy nuclei. ALICE will also study proton-proton collisions both as a comparison with lead-lead collisions in physics areas where ALICE is competitive with other LHC experiments. A particular attention is turned on the Time Of Flight (TOF) detector; this is an array of 18 big sectors containing the gaseous detector Multigap Resistive Plate Chamber (MRPC) and it is dedicated to the measurement of the time of flight of the charged hadrons produced in the collisions. The very good efficiency and time resolution of this detector and its relative low cost make the TOF an excellent candidate to perform the PID in a well determined range of momentum. In this work all the steps of the production will be presented: from the construction and the tests of the MRPC strips to the assembling of the modules containing the detectors; from the assembling and the tests of the $\sim$9m long TOF supermodules (SM) to the installation and the commissioning of the entire system in the ALICE magnet. All the careful and detailed steps needed to obtain a good system, with high efficiency, optimized occupancy and with a very low quantity of dead channels, will be showed. A study on the cluster pads in order to improve the digits reconstruction has been performed, using important informations as the Time Over Threshold (TOT), i.e. the width of the signal over the front-end electronics threshold. Quantum Chromo Dynamics (QCD) theory is the argument of the first chapter, as an introduction for the QGP Physics; in the second chapter, there is a description of the ALICE layout; the MRPC and the TOF system will be described in the third and fourth chapter. The last chapter of this work is about the alignment and analysis with cosmic rays.

Chapter 1

Heavy Ion Physics

QCD at finite temperature T and/or baryon chemical potential μ_B is of fundamental importance, since it describes the relevant features of particle physics in the early universe, in neutron stars and in heavy-ion collisions. The results of QCD Lattice calculation lead to the equation of state (EoS) of QCD matter which provides a basic input for the analysis of experimental signatures of the possible QGP formation in heavy-ion collisions. Directly addressing the EoS, the hydrodynamics realizes the connection between the matter properties and observables. The hydrodynamic treatment of the whole time evolution of colliding nuclei requires knowledge of the nuclear EoS within a large interval of its thermodynamic variables covering both the quark-gluon and hadronic sectors. In recent years significant progress has been made in understanding the phase diagram of QCD at non-zero baryon chemical potential as the non-perturbative lattice QCD methods were extended to access the relevant regions of the phase diagram[1].

1.1 QCD

A full description of the interactions involving the fundamental constituents of matter is an important issue for particle physics, astrophysics and cosmology, taking into account for example, the recent efforts in the heavy-ion collision experiments, in the study of the early Universe and that of the neutron stars. In order to reach an understanding of these topics, in the early 70s a theory of strong interaction was developed, the Quantum ChromoDynamics (QCD). QCD is a nonabelian gauge theory based on the $SU(3)$ symmetry group. Each quark has three possible "charges" related to the " colour" quantum number and the strong interaction is mediated via the exchange of eight different coloured gauge particles, called gluons. The gluon always carriess a combination of colours and anticolours and the emission of one gluon changes the colour number of the quark (anticolour for the antiquarks). Since the symmetry group of the colour quantum number ($SU(3)_C$) is non-abelian, the gluons also carry a net colour charge themselves and therefore couple to each other. This is the main difference with QED, in which the photon is a neutral particle (and the group is the abelian $U(1)_{em}$). The self-coupling of the gluon is the reason for the strong coupling constant α_S to become large at small energies (large distances) and to decrease at high energies (small distances). This property of QCD is used to explain the observed behaviour of the strong interaction:

Asymptotic freedom: at high energies (or small distances) the strong interaction proceeds via colour fields of reduced strength and the quarks and gluons behave as essentially free, non-interacting particles. This property is needed to explain why in deep-inelastic scattering the hard interaction between the boson and the parton can be calculated with noninteracting partons during the time scale in which the interaction takes place. That is, this property explains the success of the new quark parton model approach (riferimento a feynmann).

Confinement: at low energy (or large distances) the strength of the colour field is increasing (the potential behaves as $V(r) \sim \lambda r$) and in this way the quarks and gluons can never be observed as free particles. If two interacting partons are separated, the energy of the field increases so much that it creates new interacting particles and at the end (that is, at long time scales) we are left with colourless hadrons containing the partons. This is the way QCD explains the confinement of the partons, which are not observed as free particles at long time scales. It should be noted that the outgoing partons can be separated and observed as different objects, although each of these partons will be confined in a different hadron. What are not observed as free particles are coloured partons, although the partons, as well as their quantum numbers, can be studied experimentally. These properties make especially difficult to obtain predictions for the soft limit, where hadrons live and are observed in the experimental setup. Nevertheless, by choosing appropriate observables the perturbative approach can be applied profitably, giving rise to a good predictive power. Different couplings coming from the QCD Lagrangian density, can be related to the following processes:

- a (anti)quark radiating a gluon, which is dictated by the quark-gluon coupling which, in turn, is formally equal to the coupling between an electric charge and the electromagnetic field. The same coupling is related to the process in which a gluon splits into a quark-antiquark pair;
- a gluon splitting into two or three gluons, which is dictated by the self-interaction coupling of the gluon.

These processes are proportional to the strong coupling constant, so if the energy scale associated to the process is large enough, then the coupling is small and the interaction can be described by a perturbative expansion. This expansion allows the equations describing the processes to be solved in the limit where the strong coupling constant is small (hard processes).

On the other hand, if the energy scales are small, i.e. the interacting partons become further apart, then the strong coupling constant becomes very large and the perturbative approach is no longer valid. In order to be able to make predictions for the measurements performed in a collider, QCD should be studied in reactions in which the hard processes are dominant with respect to the non-perturbative ones. Usually the hard process occurs as a first step in the collision and afterwards, the soft, non-perturbative, process gives rise to the final-state hadrons (hadronisation) from the partons taking part in the hard process.

Perturbative QCD is applied to obtain predictions for the parton dynamics, and the results can be considered reliable if the hadronisation process does not hide the properties of the partonic state; that is, if the experimental measurement can be related to the parton dynamics in some direct way.

Even in the region where perturbative QCD can be applied, additional difficulties are present in the calculations. In the same way as in QED, different types of divergences appear when the vacuum fluctuations (UV divergences) or radiation of partons with very small relative transverse momentum with respect to the original parton (IR divergences) are included. Both are dealt with by following the standard regularisation procedures. This mechanism is very often called renormalisation when it is applied to get rid of the UV divergences. To remove the IR divergences the regularisation is made selecting observables which are insensitive to these particular divergences. This type of observable is called infrared-safe. The use of infrared-safe observables allows a complete separation of the hard process from the soft process in a formal way.

When the interaction contains hadrons in the initial state, as in the case of Deep Inelastic Scattering (DIS), it is impossible to be fully insensitive to the soft phenomena (including IR divergences) occurring within the hadrons, or in the steps leading from the free, initial hadron to the hard interaction. In that case, a complete regularisation mechanism is needed to separate (factorise) the theoretical description into a calculable hard and a soft part. This mechanism is called factorisation and is very similar to the renormalisation procedure.

1.1.1 QCD Phase Diagram

Analytic or perturbative solutions in QCD are hard or impossible due to the highly nonlinear nature of the strong force. The formulation of QCD on a discrete rather than continuous space-time naturally introduces a momentum cut off at the order 1/a[1], which regularizes the theory. As a result lattice QCD is mathematically well-defined. Lattice QCD provides the frame-

[1] a is the lattice scale

work for investigation of non-perturbative phenomena such as confinement and quark-gluon plasma formation, which cannot be treated by means of analytic field theories. According to lattice QCD results [2], for net baryon density, QCD matter undergoes a phase transition from a colour-confined hadron gas (HG) to a colour-deconfined quark-gluon plasma (QGP). The difference in the behaviour of strongly interacting matter at high temperatures/densities from what happens at low temperatures/densities is twofold: on one hand, the copious production of resonances in hadronic matter which will occur in a hot interacting gas sets a natural limit to hadronic physics described in terms of hadronic states. On the other, since QCD is an asymptotically free theory, its high temperatures/densities phases are dominated by its main constituents, the partons (quarks and gluons), which act as degrees of freedom, rather than by hadrons. As a consequence, the non-perturbative features characterizing hadronic physics at low energies, confinement and chiral symmetry breaking, are no more valid when strongly interacting matter is heated up or compressed. The nature of the transition from the low temperature/density hadronic state to the high temperature/density regime strongly depends on the parameters of the QCD Lagrangian, in particular on the number of light or even massless quark flavours. Besides, if considering the quark masses as they show on nature, the physical boundary conditions (i.e. the value of the net baryon number density, or chemical potential μ) play a crucial role. As a consequence, it is fundamental to determine wheter the colour-confined hadronic matter turns into a colour-deconfined quark-gluon plasma through either a real phase transition (which could be both of the first and of the second order) or a more or less rapid crossover. At vanishing or small values of μ[2], the strange quark mass becomes the control parameter of the transition. In particular, in the limit of light up

[2] μ is the baryon chemical potential, i.e. the energy needed to create a baryon

and down quark masses the transition is of the first order if the strange mass stays below a certain critical value m^c, while above m^c it becomes a continuos crossover. The value of m^c strongly depends on the masses of the light u and d quarks and it is the value for which the transition is of second order. The figure 1.1 shows how the number of flavours and the values of the quark masses affect the nature of the transition from ordinary matter to QGP. As it can be seen, there is an extended range of quark masses for which the transition to the QGP regime is no more a phase transition but becomes a crossover. The region of first order transition in the low and in the high quark mass ranges are separated from the crossover region through lines (the *chiral critical lines*) corresponding to second order transitions, where the critical quark mass m^c lies. So far, numerical calculations of m^c have been being carried out. To be noted that the dependence of the QCD phase diagram on the baryon chemical potential is, in fact, a multi-parameter issue, since a chemical potential μ_f should be defined for each quark flavour. The quark number density would be a function of μ_f. In the diagram, n_f refers to the number of degenerate quark flavours. T_d is the temperature at which deconfinement is expected to occur, while T_χ corresponds to chiral symmetry restoration; m^c_{PS} indicates the mass of the pseudo-scalar meson (which is the Goldstone-particle corresponding to the broken chiral symmetry of QCD, the pion), Z(2) corresponds to the global symmetry of the 3-dimensional theory controlling the transition in the light quark regime. It has to be noted that Z(2) is not a symmetry of the QCD Lagrangian, but takes the place of the axial $U_A(1)$ symmetry at low temperature. O(4) stands for the symmetry (typical of spin models in three dimensions) which is expected to characterize the behaviour of the chiral order parameter (and its derivative) in the $n_f = 2$ region.

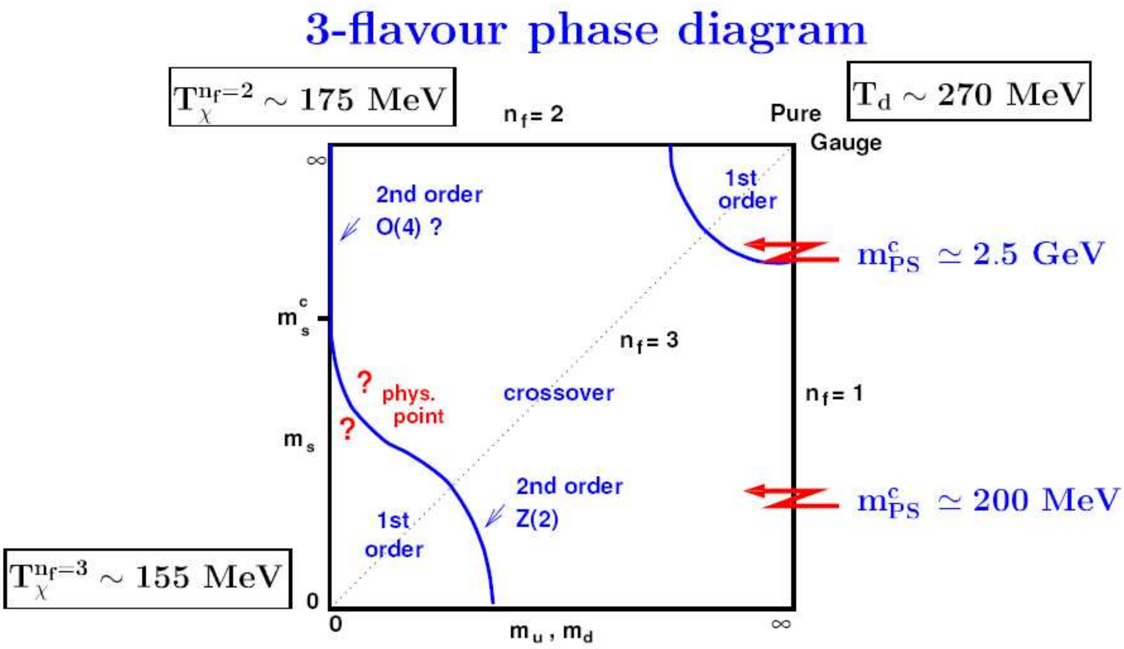

Figure 1.1: The QCD phase diagram of 3-flavour QCD as a function of the quark masses, with degenerate (u, d)-quark masses and a strange quark mass m_s for vanishing chemical potential. The question marks amphasize the importance of the location of the physical point in the QCD diagram due to its extreme complexity and richness

1.1.2 Colour Deconfinement and Chiral Symmetry Restoration

The basic features of the observed hadronic matter are explained from two properties of QCD: confinement and chiral symmetry breaking; they deeply influence the form of the QCD diagram at finite temperatures. The confinement is linked with the colourless nature of hadronic spectra and the *hadronic bag* model: the heavy quark potential is $V_{q\bar{q}} \sim \sigma r$ (where $\sigma \sim (425MeV)^2$ is the quark string tension); at zero temperature the potential rises linearly at large distances[3] and makes quarks

[3]large distances means $r \simeq 1fm$; at larger distances, the spontaneous creation of quark and anti-quark pairs from the vacuum makes the potential tend to a constant value

and gluons to be confined in a hadronic bag. This is the most significant evidence of confinement. The other important propertie of QCD is the chiral symmetry breaking, that accounts for the presence of light Goldstone particles, the pions. If we call ψ and $\bar{\psi}$ the quark and antiquark fields in QCD, the chiral symmetry breaking leads to a nonzero quark-antiquark condensate $\bar{\psi}\psi \simeq (250MeV)^2$, which vanishes inside the hadron bag. Lattice simulations for QCD at high temperature find empirically that chiral symmetry restoration and deconfinement occur at the same temperature T_c. Sufficiently below T_c the equation of state is rather well approximated by a gas of mesons; above T_c the dominant thermodynamic degrees of freedom are gluons and quarks. The change in the relevant number of degrees of freedom occurs rather rapidly and may be associated with a thermodynamic phase transition. At high temperatures, the individual hadronic bags merge to a single one, in which quarks and gluons are able to move freely. To explain this point let's speak about two observables of particular interest in QCD: the expectation value $\langle L \rangle$ of the Polyakov loop operator and the scalar quark density $\bar{\psi}\psi$. The first one is defined as the trace of a path-ordered exponential:

$$L = \frac{1}{3} tr \left(\mathcal{P} e^{-ig \int_0^{1/T} A_0(x,\tau) d\tau} \right) \tag{1.1}$$

$A_0(\mathbf{x}, \tau)$ is the gluon field in the four space-time coordinates $(\mathbf{x}, \tau)$, which satisfies periodic boundary conditions in the Euclidean time τ with period $1/T$ (being T the temperature of the system), and g is the coupling constant. The Polyakov loop operator characterizes the behaviour of the heavy quark free energy at large distances and it is an order parameter for deconfinement in the $SU(3)$ Gauge theory (valid in the heavy quark mass limit $m_q \to \infty$). L will acquire a non zero expectation value if the center symmetry is spontaneously broken. So in a pure lattice gauge theory, the Polyakov loop has a deep physical interpretation, since its expectation value is related to the free energy of a single isolated quark; hence the fact that the Polyakov loop acquires a non zero expectation value can be considered as a signature of deconfinement and the phase transition which separates the regime in which the center symmetry is unbroken from the broken symmetry phase will be the deconfinement transition. General arguments show that, for dimension $d > 1$, finite temperature gauge theories admit such a deconfinement transition for some critical value of the temperature $T = T_c$, separating the high temperature, deconfined phase ($T > T_c$) from the low temperature, confining domain ($T < T_c$). In fig 1.2 we can see that the derivative of $\langle \mathrm{L} \rangle$, i.e. susceptibility χ_L^3, shows a peak and changes sign at a certain critical value; this means that quark confinement is broken at T_c.

The second important observable is the scalar quark density $\bar{\psi}\psi$; in fig 1.3 we can see that the expectation value of this quantity is nonvanishing at low temperature ("chiral condensate") and it approaches zero while temperature increases.

We can also see the trend of the chiral susceptibility $\chi_m = \frac{\partial}{\partial m_q}\langle\bar{\psi}\psi\rangle$ that shows a peak at T_c as $\langle L \rangle$. In the QCD Lagrangian ($\mathcal{L}_{QCD}$) the up and down masses are very small, so neglecting them is a good approximation; in absence of quark masses $\mathcal{L}_{QCD}$ is invariant under separate flavour rotations of right-handed and left-handed quarks, that means chiral symmetric. A dynamic mass of the order 300 MeV for the quarks is generated when this chiral symmetry is broken, i.e. when chiral condensate has a nonvanishing expectation value (at T=0). At this dynamic mass corresponds a " constituent mass " in vacuum with a value of order 300 MeV for the up and down quraks and about 450 MeV for the strange[4]. It's important to note (fig 1.3) that

[4]the s bare mass in $\mathcal{L}_{QCD}$ is about 150 MeV

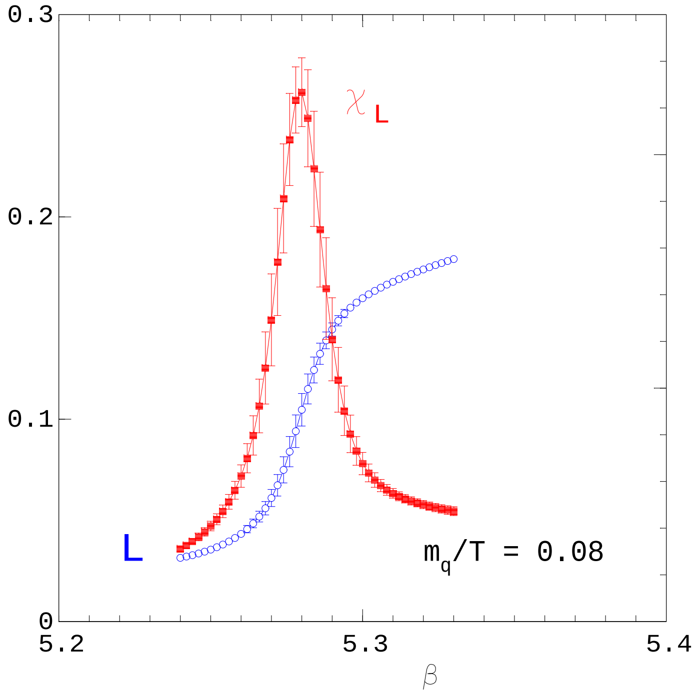

Figure 1.2: Polyakov loop expectation value $\langle L \rangle$ and its temperature derivative (Polyakov loop susceptibility χ_L) as a function of the lattice coupling $\beta = 6/g^2$ which is monotonically related to the temperature T (larger β correspond to larger T)

above T_c the dynamically generated mass melts away and the quarks become light again; this means that the chiral symmetry of QCD is restored.

In all lattice QCD calculations, starting from different values for the quark masses and then extrapolating to zero, the result is that deconfinement and chiral symmetry restoration occur at the same critical value of the temperature T_c, as can be seen in fig 1.2 and fig 1.3. So the transition from the low temperature hadronic phase to the QGP phase occurs just at T_c and it's characterized by sudden changes in the non-perturbative vacuum structure, like a sudden decrease of the chiral condensate, as well as a drastic change of the heavy-quark free energy (heavy-quark potential). So we can consider the QGP transition

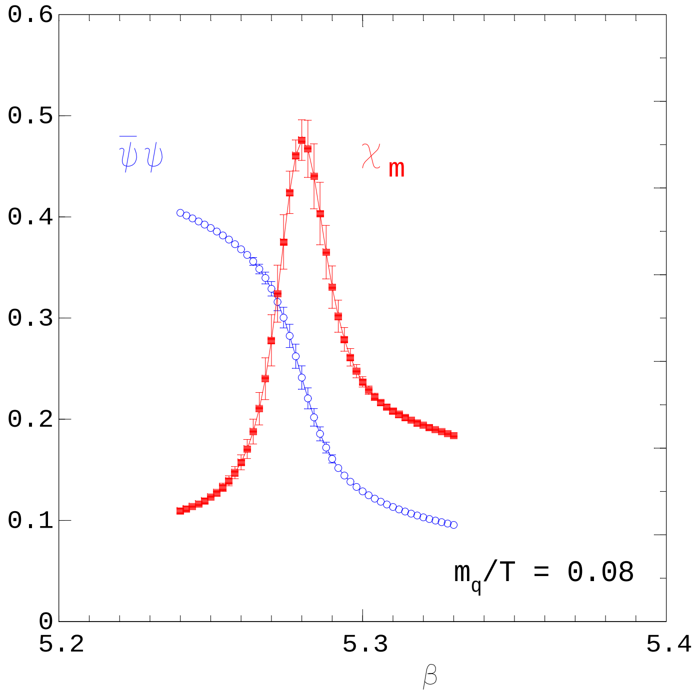

Figure 1.3: the chiral condensate $\langle\bar{\psi}\psi\rangle$ and the negative of chiral susceptibility χ_m as a function of temperature

as chiral-symmetry restoring and deconfining at the same time. The two effects strongly affect the properties of both light- and heavy-quark bound state and this is very important for the signatures of the experiment (as we will explain later). Beacause of deconfinement there is a great quantity of gluons which can produce extra quark-antiquark pairs; this leads to an equilibrium state of quarks, antiquarks and gluons. Moreover the threshold for a quark-antiquark pair formation is reduced by melting of the quark masses at high temperature (above T_c). As the strange quarks have a constituent mass well above T_c, but a current mass comparable with the critical temperature, during a heavy-ion collision (in which T_c is reached), thermal processes are likely to balance strange and anti-strange abundances. Another important point for the signatures is that heavy-quark free energy shows a temperature dependence for $T > 0.6\,T_c$: while the temperature increases, it becomes easier to separate heavy quarks at infinite distance. For example, at $T \simeq 0.9\,T_c$, the free energy difference for a heavy quark pair separated by a distance similar to the J/ψ radius (∼0.2 fm) and a pair separated to infinity is only 500 MeV; this energy is compatible with the average thermal energy of a gluon. As a consequence, the bound $c\bar{c}$ states are expected to disappear at high temperature. At the end another consequence of chiral symmetry restoration is a change in the light-meson spectra, since hadronic correlation functions constructed from light quark flavours show a drastically different behaviour below and above T_c.

1.1.3 The Equation of State

Reaching a quantitative understanding of the equation of state (EOS) of QCD is one of the central goals in finite temperature field theory. The intuitive picture of the high temperature phase of QCD behaving like a gas of weakly interacting quarks and gluons is based on leading order perturbation theory. However, the well-known infrared problems of QCD [3] result in a poor convergence of the perturbative expansion of the thermodynamic potential even at temperatures very much higher than T_c [4, 5]. Although the newly developed techniques of resummed perturbation theory have led to much progress in perturbative calculations [6], non-perturbative effects dominate the equation of state in the temperature regime attainable in heavy ion experiments. In fig 1.4 we can see the the temperature dipendence of the pressure in the cases of pure gauge and different number of degenerate quarks flavours [7].

At high temperature the pressure p and the energy density ϵ are directly proportional to the basic degrees of freedom contributing the thermodynamic properties of the plasma; so, bea-

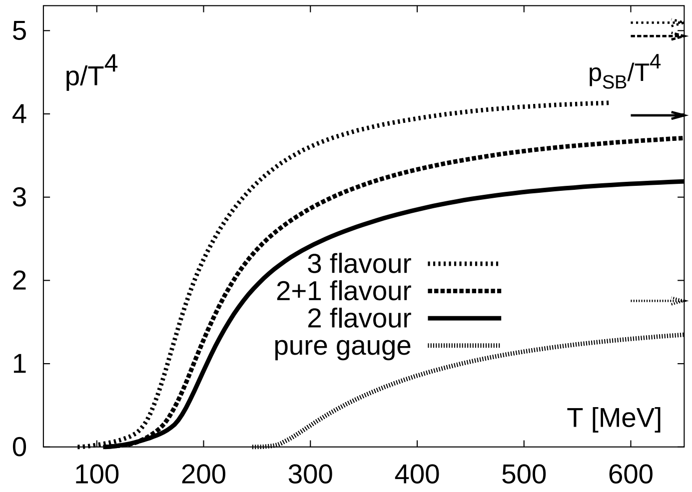

Figure 1.4: the pressure in QCD with two and three degenerate quarks flavours as well as with two light quarks and a heavier (strange), compared with pure gauge

cause of asymptotic freedom, these observables would be expected to show ideal gas behaviour. If n_f is the number of quark flavours, for example, the asymptotic behaviour of the pressure would be given by the Stefan-Boltzmann law

$$\lim_{T\to\infty} \frac{p}{T^4} = (16 + 10.5n_f)\,\frac{\pi^2}{90}. \tag{1.2}$$

As said before, perturbative calculations fail to study bulk thermodynamics when deviating from ideal gas behavioiur and so we need lattice calculations, based on the following relations:

$$\frac{p}{T^4} = \frac{1}{VT^3}\ln Z(T, V, \mu_f), \tag{1.3}$$

$$\frac{\epsilon - 3p}{T^4} = T\frac{\mathrm{d}}{\mathrm{d}T}\left(\frac{p}{T^4}\right)\Big|_{fixed \mu/T}. \tag{1.4}$$

In these relations, T is the temperature, V is the volume, μ_f is a set of chemical potentials, $(f = 1, ..., n_f)$ different quark flavours and $Z(T, V, \mu_f)$ is the grand canonical partition function

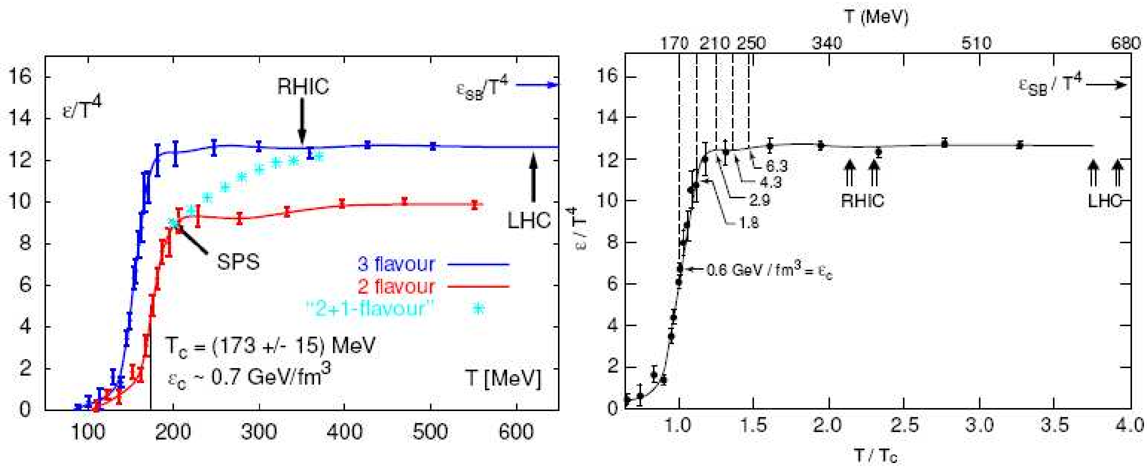

Figure 1.5: energy density in units of T^4 for QCD with two and three degenerate quark flavour. For $T<4T_c$ the lattice data remain about 20% below the Stefan-Boltzmann limit, indicated by the arrow in the upper-right corner of the graph. Near Tc the ratio ϵ/T^4drops rapidly by more than a factor 10, as a consequence of hadronization

suitable for elementary particles interacting only through the strong force [7]. We can see that at high temperature the value of p/T^4 depends from the number of degrees of freedom; as one can see in fig. 1.3, the transition region shifts to smaller temperatures as the number of quark flavours increases.

From eq. 1.4 it's possible to obtain the results of lattice calculations for the energy density; for a massless gas of quarks and gluons the energy density is proportional to T^4 and the proportionality constant strongly depends on the number of massless degrees of freedom. As a consequence of the 15 MeV of uncertainty on the determination of T_c, the value of the critical energy density for deconfinement ϵ_c could be in a range from $\sim$ 1 GeV/fm^3 to 500 MeV/fm^3; an easy value to handle and to quote is ϵ=1 GeV/fm^3 since it corresponds to the density in the centre of a proton. In the right panel of fig. 1.5 we can see the importance of the factor T^4 in terms of energy density; in fact, to reach, for example, $2\,T_c$ in order to approach the edge of the transition region, energy density value is about 23 GeV/fm^3, that means $\sim$40 times the critical value ϵ_c. During the last few years at the Relativistic Heavy Ion Collider (RHIC) at BNL in Au+Au collisions (at $\sqrt{s}_{NN}$= 130 GeV) such energies have been achivied; it will be possible to reach even higher energy densities ($\sim$500 GeV/fm^3) with Large Hadron Collider (LHC) at CERN.

1.2 QCD Matter in Relativistic Heavy-Ion Collisions

QCD allows to study the phase transition of hadronic matter from ordinary conditions to extreme conditions of temperature and energy density; in this study, also cosmological and astrophysical implications are involved, since the phase transition is believed to have happened in the first stage of the evolution of the Universe (during the first 10^{-5} seconds after the Big Bang); it's also supposed that the transition may even happen in the core of neutron stars. But the system exhisting during the early Universe and in the neutron stars and that predicted from lattice QCD calculations are very different from the system created in a heavy-ion collision; in fact the small size of the available nuclei sets the scale for the temporal and spacial extent of the system created in the collision. The incoming system has an asymetry due to the direction of its momentum, that is in the direction of the incoming beams; this asymmetry is reflected in the evolution of the system. What remains is just a bulk of hadronic and leptonic residues. So, the main experimental and theoretical aim is to look at the experimental observables related to the products of the collision, in order to reconstruct the properties of the earlier stages of the system. We can have informations about the chromoelectric field fluctuations in the QGP, looking at leptonic probes; we can study the chemical composition of the QGP, looking at the very abudant hadronic probes; we can also have indirect informations related to the chiral symmetry restoration, thanks to some decays.

1.2.1 Evolution of the Collision

The fireball created in an ultrarelativistic heavy-ion collision is the environment in which all processes providing hints about the possible formation of the QGP happen. It is therefore crucial to understand the dynamics of this hot and dense system. The fireball evolution is reconstructed between two stages, the freeze-out, which is accessible by hadronic observables, and the initial collision for which the overlap geometry can be calculated [8]. A schematic evolution of the system is the following: the two colliding nuclei deposit energy into the reaction zone which materializes in the form of quarks and gluons which strongly interact with each other. This early, very dense state (energy density about 3-4 GeV/fm^3, mean particle momenta corresponding to $T\sim$ 240 MeV) suppresses the formation of charmonia, enhances strangeness and begins to drive the expansion of the fireball. Subsequently, the plasma cools down and becomes more dilute. At an energy density of 1 GeV/fm^3 ($T\sim$ 170 MeV) the quarks and gluons hadronize and the final hadron abundances are fixed. At an energy density of order 50 MeV/fm^3 (T = 100-120 MeV) the hadrons stop interacting, and the fireball freezes out. At this point it expands with more than half the light velocity.

The Early Stage of the Collision

It's possible to divide a heavy-ion collision in three phases: thermalization, expansion and decoupling. Before the thermalization (before the QGP creation) hard particles with a large mass or large transverse momenta [5] are produced; this can be studied with perturbative QCD, since their creation involves large momentum transfers [6]. High-p_t quark and gluon jets, due to their hard production scales, materialize very early during the collision and are thus embedded into and propagate through the dense environment of the fireball as it forms and evolves. In particular, they are expected to suffer a loss of energy as they traverse the dense medium created in the collision zone. The loss of energy is supposed to be proportional to energy density, therefore through this interaction, they measure the property of the environment and are sensitive to the formation of a QGP [9].

Because of the presence of the electric charge in the medium (quarks and antiquarks), direct photons are produced during the first stage of the collision [10]; these photons can be real or virtual. The virtual photons can materialize in lepton-antilepton pairs, called dileptons. Direct photons can escape from the interacting region without rescattering and so they carry the signatures of the initial phase of the collision and in particular of the momentum distributions of their parent quarks and antiquarks.

Thermalization and Expansion

The key difference between elementary particle and nucleus-

[5] p_t>> 1 GeV/c
[6] of the order of $Q^2 \sim {p_t}^2$>>1 GeV^2

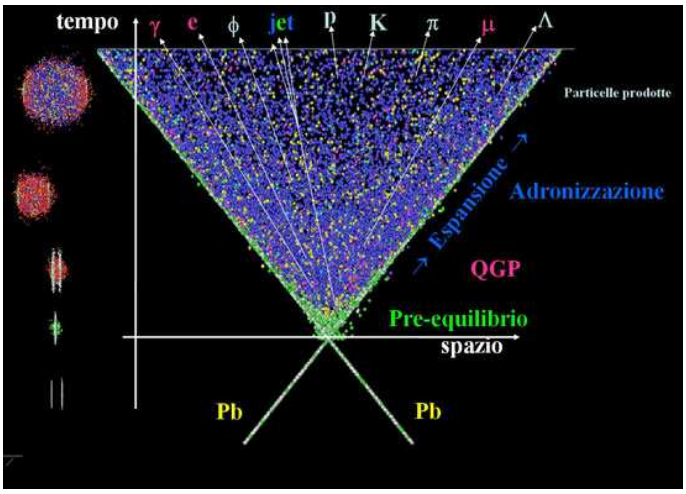

Figure 1.6: space-time evolution of a Pb-Pb collision

nucleus collisions is that the quanta created in the primary collisions between the incoming nucleons can't right away escape into the surrounding vacuum, but rescatter of each other. In this way they create a form of dense, strongly interacting matter which, when it thermalizes quickly enough and at sufficiently large energy density, is a quark-gluon plasma. This is why with heavy-ion collisions we have a chance to recreate the matter in the very early universe whereas with high energy collisions between leptons or single hadrons we don't. The produced partons rescatter both elastically and inelastically. Both types of collisions lead to equipartitioning of the deposited energy, but only the inelastic collisions change the relative abundances of gluons, light and strange quarks. From the phenomenology of *pp* collisions it is known [11, 12] that the produced hadron abundances are distributed statistically, but that strange hadrons are systematically suppressed[7]. In a heavy-ion collision, if the reaction zone thermalizes at energy density higher than ϵ_c such that gluons are

[7]probably because strange quarks are not present in the initial state and their large constituent mass of $\simeq$ 450 MeV makes them hard to create from the vacuum as the produced partons hadronize.

deconfined and chiral symmetry is restored, strange quarks are much lighter ($m_s \simeq 150$ MeV) and can be relatively easily created by secondary collisions among the many gluons, leading to chemical equilibration between light and strange quarks [13]. The observed strangeness suppression in *pp* collisions should thus be reduced or absent in relativistic heavy-ion collisions [14]. A thermalized system has thermal pressure which, when acting against the surrounding vacuum, leads to collective (hydrodynamic) expansion of the collision fireball. As a consequence, the fireball cools and its energy density decreases. When the latter reaches $\epsilon_c \simeq 1$ GeV/fm^3, the partons convert to hadrons. During this phase transition the entropy density drops steeply over a small temperature interval. Since the total entropy cannot decrease this implies that the fireball volume must increase by a large factor while the temperature remains approximately constant. The growth of the fireball volume takes time, so the fireball ends up spending significant time near T_c. Furthermore, while the matter hadronizes its speed of sound $c_s = \sqrt{\partial p/\partial \epsilon}$ is small [2], causing inefficient acceleration so that the collective flow[8] does not increase during this period. This may be visible in the direct photon spectrum. The direct photon spectrum and the centre-of-mass energy dependence of the collective flow would then be affected by the consequent softness of the equation of state.

[8]the collective flow is an unavoidable consequence of quark-gluon plasma formation in heavy-ion collisions. Since a quark-gluon plasma is by definition an (approximately) thermalized system of quarks and gluons, it has thermal pressure, and the pressure gradients respect to the surrounding vacuum causes the quark-gluon plasma to collectively expand, originating the collective flow.

Chemical and Thermal Freeze-out

After hadronization, two kinds of processes occur: *chemical* and *thermal* or *kinetic freeze-out*. The hadrons go on rescattering with each other, continuing building up expansion flow; the chemical freeze-out occurs when the rates for inelasting scatterings become too small to change the chemical composition of hadronic system (i.e. the identity of the hadrons) and to allow further expansion. The thermal freeze-out, instead, takes place when the distances among hadrons become larger than the range of strong interactions and also the elastic processes stop. This happens later than the ceasing of inelastic processes, because of the small inelastic cross section respect to the total one[9]. At kinetic freeze-out all hadrons, including the unstable resonances, have an approximately exponential transverse momentum spectrum reflecting the temperature of the fireball at that point, blueshifted by the average transverse collective flow[10]. The unstable resonances decay, however, producing daughter particles with, on average, smaller transverse momenta. The experimentally measured spectra off stable hadrons cannot be understood without adding these decay products to the originally emitted spectra. Since most resonances decay by emitting a pion, this effect is particularly important for the pion spectrum which at low p_t are completely dominated by decay products. This seriously affects the slope of their spectrum out to $p_t \simeq$ 700 MeV, making it steeper than the blueshifted thermal spectrum of the directly emitted hadrons.

[9]elastic processes include resonant processes such as π+N$\rightarrow$ $\Delta\rightarrow\pi$+N where two hadrons form a short-lived resonance which subsequently decays back into the same particles (possible with different electric charge assignments). Such processes don't change the finally observed chemical composition, but they contribute to the thermalization of the momenta and have large resonant cross sections.

[10]the transverse flow is the component of the flow velocity in the plane perpendicular to the beam axis.

1.3 QGP Signatures

Ultra-relativistic heavy-ion collisions offer the unique opportunity to probe highly excited dense nuclear matter under controlled laboratory conditions. One of the main driving forces for these studies is the expectation that an entirely new form of matter may be created in such reactions. This form of matter, called the quark gluon plasma (QGP), is the QCD analogue of the plasma phase of ordinary atomic matter. However, unlike such ordinary plasmas, the deconfined quanta of a QGP are not directly observable because of the fundamental confining property of the physical QCD vacuum. What is observable are hadronic and leptonic residues of the transient QGP state. The QGP state formed in nuclear collisions is a transient rearrangement of the correlations among quarks and gluons contained in the incident baryons into a larger but globally still color neutral system with however remarkable theoretical properties, such as restored chiral symmetry and deconfinement. The task with heavy-ion reactions is to provide experimental information on this fundamental prediction of the standard model [15]. The strategy should consist in a systematic variation of an external parameter (such as the centrality[11] of the collision and the beam energy) with the consequent measurement of excitation functions of several signals which in the case of a phase transition show *simultaneously* an anomalous behaviour. A lot of problems occur in trying to investigate the properties of the QGP in laboratory: if the plasma is created, it has a very limited lifetime, a few fermi in diameter and about 5 fm/c in duration;

[11]In high-energy physics experiments, the centrality of a collision is determined by the distance between the center of the two colliding nuclei (i.e. the impact parameter) in such a way that the smaller the impact parameter, the more central the collision. As a consequence, centrality is strongly related to the geometry of the collision, and in particular to the number of partecipating nucleons. Moreover, since the inelastic cross-section σ^{inel}_{A+A} is a function of the impact parameter [16], the centrality is often defined in terms of percentage of σ^{inel}_{A+A}.

furthermore, the background (coming from the hot hadronic gas phase that follows hadronization) would screen the signals from the QGP and these would be also significantly modified by the interaction occurring later in the hadronic phase. Nevertheless, some physical observables have been identified as promising signatures of the QGP. We could divide the signatures in different categories that we will explain in the next sections: kinematic probes, probes of deconfinement, jet quenching, elliptic flow, Hanbury-Brown-Twiss source radii.

1.3.1 Kinematic Probes

Thermodynamic properties can be extracted from the collision observables. Usually, the temperature T, entropy density s, and energy density ϵ are identified with the average transverse momentum $< p_T >$, the hadron rapidity distribution dN/dy[12], and the transverse energy dE_T/dy, respectively [17]. If a phase transition occurs (i.e. a rapid change in the number of degrees of freedom) one expects a monotonously rising curve interrupted by a plateau, which would be caused by the saturation of $<p_T>$ during the mixed phase (QGP + hadronic phases). After the transition, the mean transverse momentum rises again, altough according to detailed hydrodynamical studies the plateau is washed out due to collective flow [18, 19].

[12]Being E the particle energy and p_z the momentum component along the z axis (usually the beam direction), then the rapidity y is defined as:

$$y = \frac{1}{2} \ln \left(\frac{E + P_z}{E - p_z} \right).$$

To be noted that if $p{>>}m$ (where p and m are the momentum and the mass of the particle), the rapidity coincides with the pseudorapidity η = - ln tan$\theta/2$ (where cosθ=p/p_z).

Particle Spectra

The shape of particle spectra is strongly influenced by collective (transverse) flow that feeds from resonance decays; this effect could be seen in a shoulder-arm shape of the transverse momentum spectra [20]. It is useful and practical to study the transverse mass (m_T=$\sqrt{m^2 + p_T{}^2}$, where p_T is the transverse momentum of the particle); this parameter reflects the transverse flow created after the impact between the two nuclei. If rescattering among the fireball constituents results in thermalization and collective flow and if all the hadrons decouple (i.e. stop interacting) simultaneously, the shape of all hadrons m_T spectra are characterized by only two parameters, the freeze-out temperature T_f and the mean transverse flow velocity $\langle v_T \rangle$ at freeze-out. We can observe different behaviours of hadron spectra depending on relativistic or non-relaticicistic region; in the relativistic region (m_T>>m) we know that all hadron spectra follow the same exponential ("m_T scaling effect"), that is $dN/(m_T dm_T dy) \sim m_T{}^{1/2} \mathrm{e}^{-m_T/T}$, from which the fireball temperature T can be directly extracted. Moreover, the effect of the flow on the spectra in this p_T regime can be expressed by the formula:

$$T \approx T_f \sqrt{\frac{1+v_T}{1-v_T}} \tag{1.5}$$

where T is the inverse slope of the particle spectra; at large values of m_T the spectra of all hadrons have the same slope T. Instead, in the non-relativistic region, where m_T<<m, the particles mass becomes a crucial parameter and the relation

$$T \approx T_f + \frac{1}{2} m \langle v_T \rangle^2 \tag{1.6}$$

hold true. The collective flow contribution contained in the spectra, which results for example in an inverse slope for pro-

tons of ~
and look
nation of
of T. T
servables
(Hanbur
have to b
of the sp
concerni

Fig.
for charg

Figure 1.7: inverse slopes T of the measured m_T-distributions from 158 AGeV/c Pb+Pb collisions for various hadron species and in different experiments, plotted as a function of the rest mass [21]

The ρ Particle and the Lepton Pairs

Studying the ρ meson it is possible to obtain informations concerning what happens immediately after the collision and just before hadron decoupling. A first generation of ρ particles decays in dilepton pairs (e^+e^- or $\mu^+\mu^-$) which escape from the fireball without interacting again. After these decays, a second generation of ρ mesons is produced by $\pi\pi$ resonant scattering; these second ρ decay, in turn, into lepton pairs. So, the measure of the number of extra dileptons with the invariant mass of the ρ meson can be considered as a first measure of the fireball lifetime. Besides, lepton pairs from hadronic sources in the invariant mass range between 0.5 and 1 GeV are important signals of the very highly dense medium which is formed during the collision. They provide important informations on possible medium modifications of hadronic properties. For example, it could occur a broadening of the ρ peak in the e^+e^- spectrum, because the pions not only strongly rescatter each other, but also with the baryons in the hadronic resonance gas; this modifies their spectral densities, and smears the ρ resonances in the $\pi\pi$ scattering cross section. The pions are the most abundant particles in the hadron gas and their intense rescattering allows the fireball to reach and almost maintain a local thermal equilibrium, to build up thermodynamic pressure and to collectively explode. [13]

[13]The outnumbering of the dileptons from the broadened ρ with respect to those from unmodified ρ emitted at thermal freeze-out would indicate that the hadronic rescattering stage has lasted several ρ lifetimes.

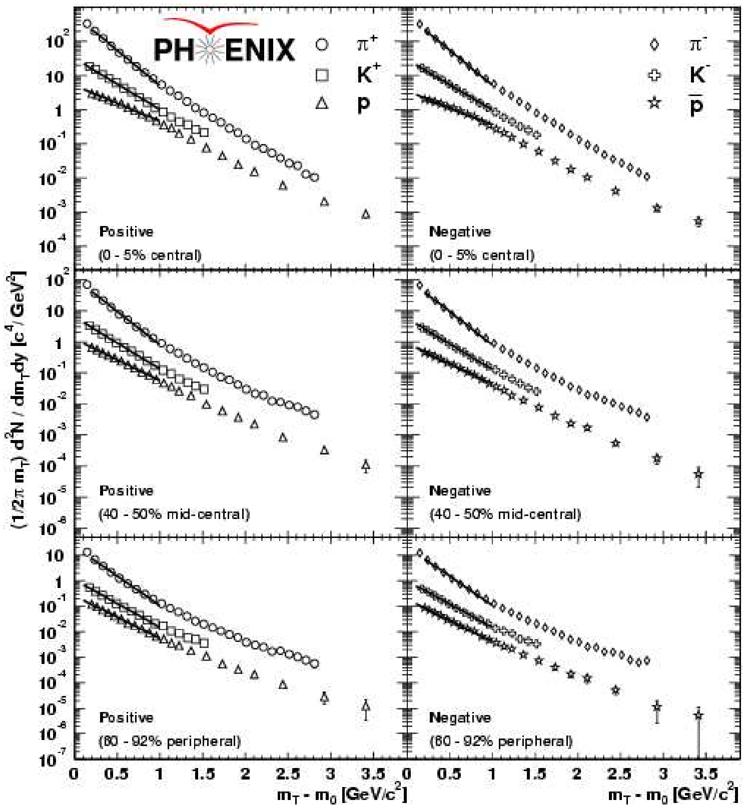

Figure 1.8: transverse mass (minus the rest mass) distributions for $\pi^{\pm}$,$K^{\pm}$,p,$\bar{p}$ for different centralities in Au+Au collisions at $\sqrt{s_{NN}}$=200 GeV obtained from the PHENIX experiment [20]

Direct Photons

Informations about high-p_T hadrons and about thermodynamic state of the plasma can be obtained from another important effect of heavy-ion collisions: the direct photons. A heavy-ion collision is characterized by a large amount of direct (thermal) photons produced, coming from various processes, the most important of which are $q\bar{q}\rightarrow\gamma g$ (annihilation) and $gq\rightarrow\gamma q$(Compton scattering)[14]. Measurements of direct photon

[14]There are other processes that contribute to the observed rate of direct photons, such as initial state momentum broadening of the incoming particles (Cronin effect), additional fragmentation contributions [22, 23] or additional scatterings in the thermalized matter of the final state.

production allow a more definite discrimination between initial and final state suppression of high-p_T hadrons due to the fact that photons, once produced, are essentially unaffected by the sorrounding matter. Hence, photons produced directly in initial parton scatterings will not quench unless the initial parton distributions themselves are suppressed in the nucleus. The second important point is that the production rate of thermal photons and their momentum distribution are strongly affected by the momentum distributions of the quarks, antiquarks and gluons in the plasma. As a consequence, the photons may carry information about thermodynamic state of the plasma at the moment of their creation. The main hadronic background processes which can interfere with the detection of direct photons are pion annihilation $\pi\pi\rightarrow\gamma g$ [24, 25], dominant during the plasma phase, and Compton scattering $\pi\rho\rightarrow\gamma\pi$, which mostly occur during the thermal hadron gas phase. Screening effects are responsible for photon spectra of almost equal intensity and shape at T_c for both the hadronic phase and the QGP phase, but if a very hot plasma is formed, a clear signal of photons from the QGP could be visible for transverse momenta p_T in the range 2÷5 GeV/c [26, 27][15]. Fig. 1.9 shows the direct photon momentum distribution as measured from the data taken by the PHENIX experiment [28] during the second RHIC run for Au+Au collisions at $\sqrt{s_{NN}}$=200 GeV. The perturbative QCD lines reported are described in [29].

[15] Separate contributions from different stages of the system evolution are difficult to distinguish because of transverse flow effects, which are important up to momenta ~ 5 GeV.

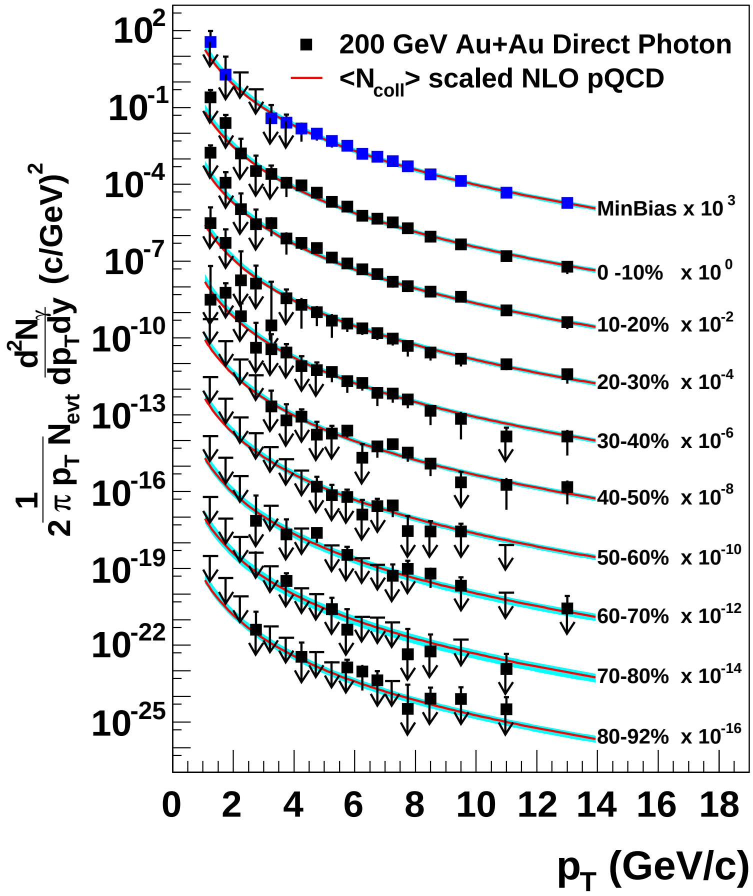

Figure 1.9: direct photon invariant yields as a function of transverse momentum for nine different centrality selections and minimum bias Au+Au collisions at $\sqrt{s_{NN}}$=200 GeV. See [29] for more details.

1.3.2 Probes of Deconfinement

It is very important to identify the observables which can be considered as QGP signatures and that can distinguish the heavy-ion collisions from nucleon-nucleon collisions, during which the formation of a deconfined phase is impossible. Two very important signatures are the *strangeness enhancement* and the *c*-$\bar{c}$ *bound states suppression.*

Charmonium and Open Charm Production

Charmonium production in hadronic processes [30] and nuclear [31] collisions is usually described as made up of three different stages: the creation of a $c\bar{c}$ pair, the formation of a bound $c\bar{c}$ state and its subsequent interaction with the sorrounding medium. Because of this interaction, a suppression of the finally observed bound $c\bar{c}$ states occurs with respect to the initially created number, which is proportional to the number of Drell-Yan lepton pairs. The formation of a highly dense intermediate medium can be proved looking at the entity of the suppression; if, going from peripheral to central collisions, a rapid increase of the suppression is noted, this is attributed to a QGP state [32]. Charmonium suppression is due to the formation of the highly dense gluon system resulting from deconfinement. In a medium of charged particles, the interactions of one charge will be reduced or cancelled out by the surrounding charges. This effect is known as Debye screening, and while originally defined for electromagnetic plasmas, it has been extended to plasmas of colour charge as well. It is parametrized by the Debye screening radius λ_D, the radius at which the effective charge of a particle is reduced by a factor of $1/e$. Outside the medium, $c\bar{c}$ states can be reasonably represented by a potential model, with the potential energy

$$V(r) = kr - \frac{\alpha_{eff}}{r} \tag{1.8}$$

Inside the QGP, however, the linear term will disappear as T approaches the critical temperature T_c and a screening factor will be introduced to the Coulombic term, giving rise to the modified potential

$$V(r) = -\frac{\alpha_{eff} e^{-r/\lambda_D}}{r} \tag{1.9}$$

where λ_D is determined by the temperature of the medium. The net result is the potential well becoming much shallower, until even small perturbations can knock the $c\bar{c}$ out of the bound state. Qualitatively, we can think of this change as the short-range strong interactions in the medium dominating the long-range interactions. The key is that the relative scale of long-range versus short-range for the $c\bar{c}$ changes when it is immersed in the plasma, such that the binding interaction is no longer dominant [33]. This is expressed pictorially in fig. 1.10.

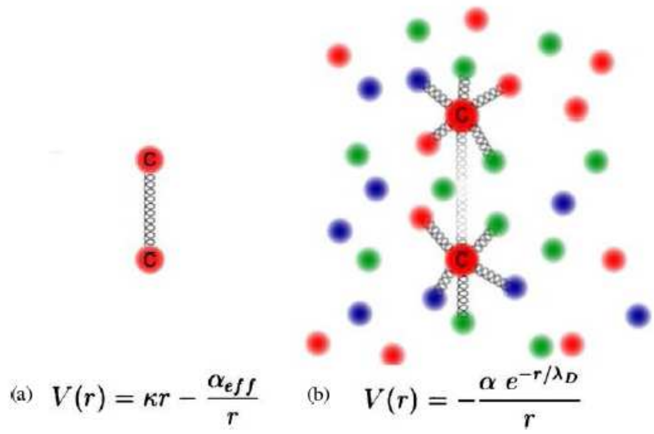

Figure 1.10: J/ψ in (a) vacuum and (b) the QGP.

So Debye-screening causes the suppression, preventing the quarks c and $\bar{c}$ from binding into a charmonium state (J/ψ, χ_c, ψ'). It has to be noted that the states to be suppressed while increasing the energy achieved are the losely bound ψ' and χ_c, followed by the strongly bound J/ψ. Another important process has to be taken on account: the open charm production. A D-meson pair should be created by collisions of $c\bar{c}$ with comoving hadrons; the D-meson multiplicity is determined by the number of $c\bar{c}$ quarks in the early parton stage before hadronization. As a result, the production of open charm is carried mainly by the D meson in the final state. Other contributions to charmonium suppression may come from nuclear shadowing of soft gluons, initial state scatterings of partons resulting in a widened transverse momentum distribution and as a function state absorption on nucleons [34]. Owing to its finite size, the formation of a $c\bar{c}$ bound state requires a time of the order of 1 fm/c [35], after which the J/ψ may still survive, if it escapes from the region of high density and temperature before the $c\bar{c}$ pair has been separated by one more than the size of the bound state [36]. This could happen if the QGP cools very fast, or if the J/ψ momentum is sufficiently high.

In fig. 1.11 it is showed the experimental results concrening J/ψ suppression obtained from Pb+Pb collisions by the NA50 experiment, as well as those from NA38 with ligther incident ions; the higher the energy density, the more the J/ψ production rate differs from the nuclear absorption regime. Now we have some models that predict that, at energies as high as those available at RHIC and in a very near future at LHC, an enhancement of heavy quarkonia should occur as a consequence of $c\bar{c}$ coalescence[16]in the QGP[37], as well as to a detailed balance of $D+D \leftrightarrow J/\psi+X$ [38] and/or statistical J/ψ production [39]. In addition initial state effects of shadowing and possible parton saturation may play an important role in charm production.

Strangeness Enhancement

Strangeness enhancement was among the first signatures proposed for the possible observation of a QGP and it can be studied through the production of strange particles as $\phi(s\bar{s})$, K$(u\bar{s})$,

[16]coalescence is the process that occurs at high denisities: hadronization is not due to fragmentation, but to a statistical recombination of nearest quarks

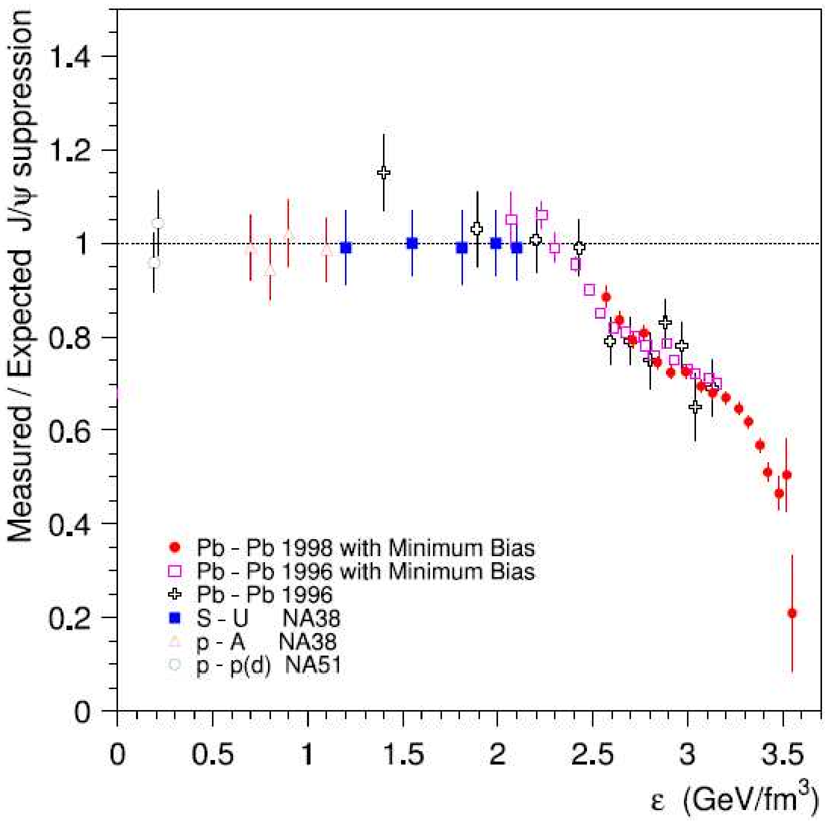

Figure 1.11: the anomalous J/ψ suppression as a function of the energy density reached in the heavy-ion collision. Suppression is obtained from the measured cross sections divided by the values expected from nuclear absorption. The latter are deduced from a fit to measurements on interactions of incident protons with various targets (open circles and triangles) and on sulfur-uranium collisions (closed black squares). As can be seen from the figure, in lead-lead interactions J/ψ is suppressed normally, i.e. according to pure nuclear absorption, for energy densities than 2.2 GeV/fm^3. For higher density values, a peculiar abnormal suppression pattern is observed, as can be expected from charmonium melting due to deconfinement

$\Lambda(uds)$. There is more than one reason for which strangeness enhancement can occur in heavy-ion collisions. On one hand, $s\bar{s}$ pairs can be created by gluon fusion, due to colour deconfinement that leads to a large gluon density. On the other, the production threshold for strange quarks is reduced by chiral symmetry restoration that makes the strange mass relatively light (see Sec. 1.1.2). Another important feature is that in a baryon rich environment as that created in heavy-ion collisions, the baryon stopping is large. If the hadronic matter is deconfined during the collision, the volume of the central fireball will be already occupied by many u and d quarks coming from the interacting nuclei. As a consequence, while the production of u and d quarks is suppressed because of Pauli principle, the production of s will be relatively enhanced. Fig. 1.12 shows the K/π ratio as obtained by the STAR experiment at RHIC as a function of collision energy compared with p+p data from [40] and p+$\bar{p}$ from [41].

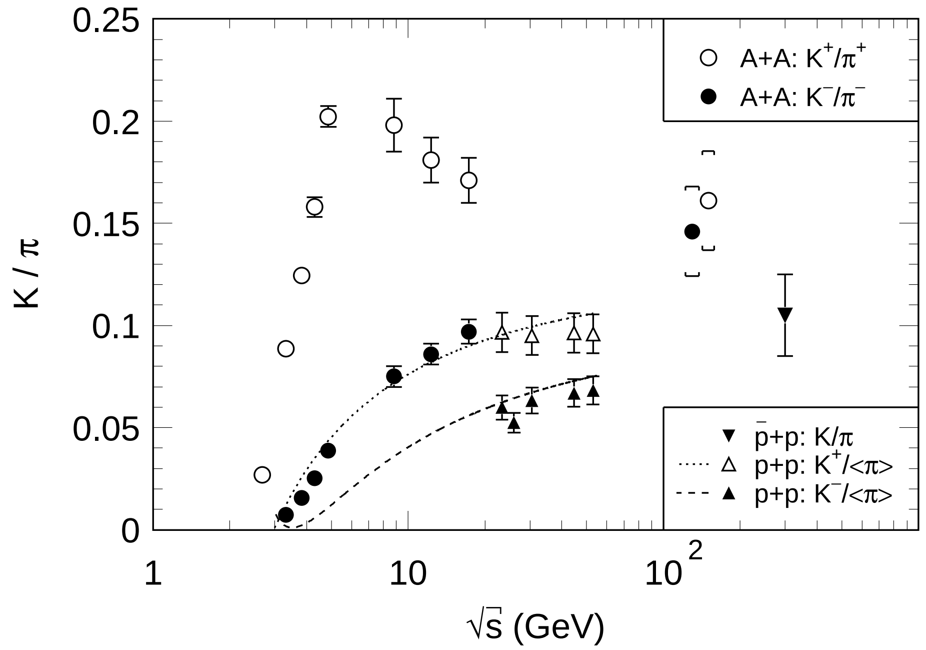

Figure 1.12: mid-rapidity K/π ratios vs. $\sqrt{s_{NN}}$. The curves refer to p+p data [40]. See [42] for more details.

Multistrange particles are also abundantly produced in heavy-ion collisions during the QGP hadronization phase [43]. As a consequence, after the gluon processes $gg \rightarrow s\bar{s}$, quark recombination leads to the emergence of particles such as $\Theta(sqq)$ and $\bar{\Omega}$ ($\bar{s}\bar{s}\bar{s}$) which otherwise would be improbably produced; so, enhancement of these particles can be considered as a QGP signature. In fig. 1.13 it is showed the rise of enhancement with strange content, with the p+Be reaction system taken as reference. The QGP prediction that enhancement grows with strangeness and antiquark content is confirmed in fig. 1.13 (respectively left and right) [44].

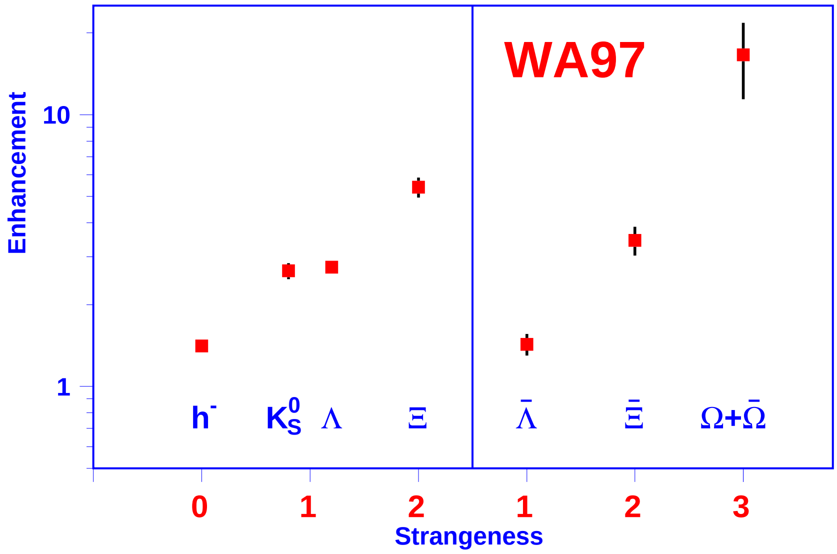

Figure 1.13: strangeness abundance enhancement in Pb+Pb collisions at $\sqrt{s_{NN}}$=158 GeV with respect to the yield in p+Be collisions, scaled with the number of wounded nucleons [44]

1.3.3 Jet Quenching

During hard scattering processes, thanks to fragmentation process, cones of hadrons (jets) can be formed. The propagation of partons through a hot and dense medium modifies their transverse momentum due to induced radiative energy loss, a phenomenon called jet quenching. This can be studied by measuring the p_T distribution of hadrons coming from high-p_T jets. In fact, when a hard collision producing two jets occurs near the edge of the nuclear overlap region, jet quenching might lead to complete absorption of one of the jets, while the other escapes. This signature can be found by studying the number of correlated jets at different angular separations.

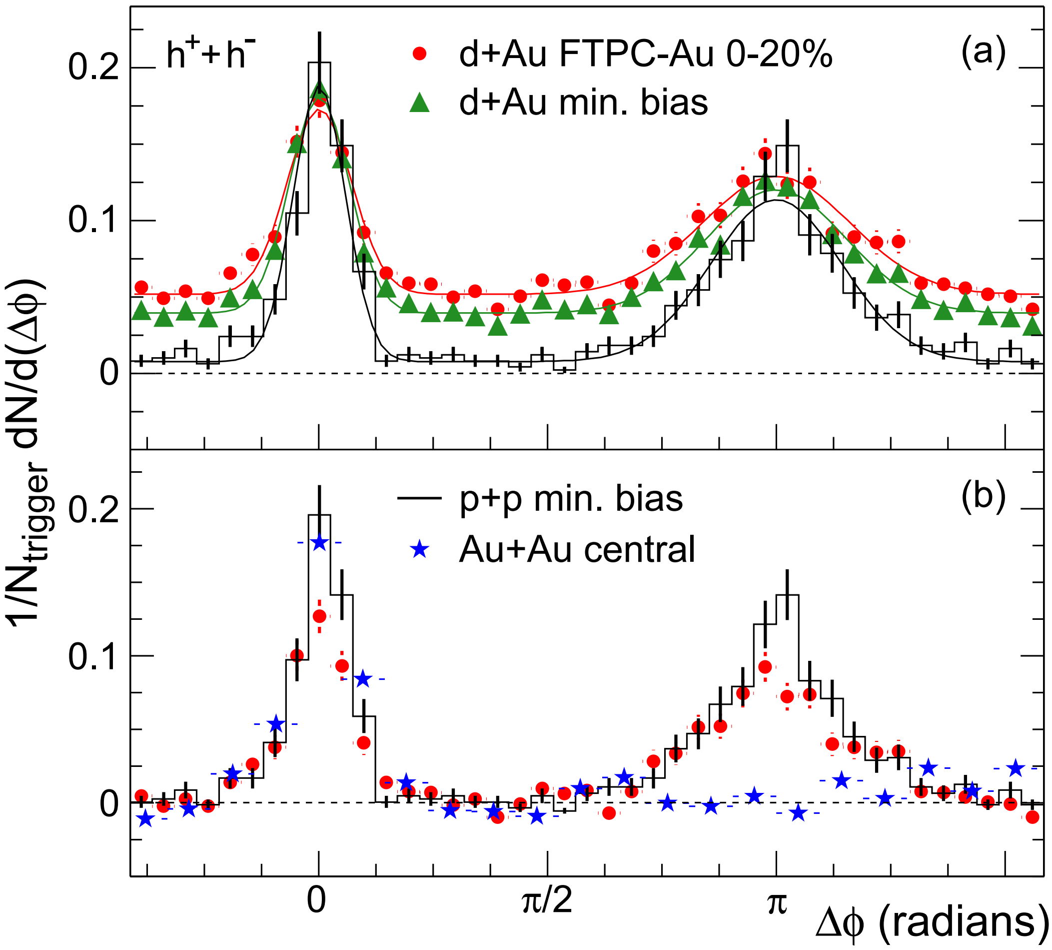

Figure 1.14: top: two particle azimuthal correlations in p+p as well as in minimum bias central d+Au collisions, [45] (curves are fitted as described in [46]); bottom: comparison of two-particle azimuthal distributions for p+p, central d+Au and Au+Au collisions [45].

Since energy loss in a hot and dense medium through gluon bremsstrahlung is expected to be larger in a system of deconfined colour charges than in hadronic matter, this is considered an effective signature of the formation of a QGP. Studies of the angular correlation of high-p_T particles, with respect to a high-p_T trigger particle selected in each event, have been carried out by the STAR experiment at RHIC [46], as shown in fig. 1.14. For p+p and d+Au collisions, these studies show the characteristic near-side and back-to-back correlation of high-p_T particle jets. On the contrary, when looking at Au+Au ollisions, while the near-side correlation still remains, the back-to-back is almost completely suppressed; in fact, as said before, jet quenching is due to the interaction with the dense medium: while the away-side jets has to transverse it, the same-side jet is not quenched, due to surface emission. The results of STAR concerning the pathlenght dependence of radiative energy loss are showed in fig 1.15.

In particular it is possible to note that in peripheral collisions the suppression of the back-side jet is influenced by the relative orientation of the back-to-back pair with respect to the reaction plane[17], as a consequence of elliptic flow (see Sec. 1.3.4) [47].

1.3.4 Elliptic Flow

Elliptic flow in heavy-ion collisions measures the anisotropy of particle momentum distributions in the plane perpendicular to the beam direction. It results from the initial spatial anisotropy in non-central collisions and is thus sensitive to the properties of

[17]The reaction plane is defined by the impact parameter direction and the beam direction.

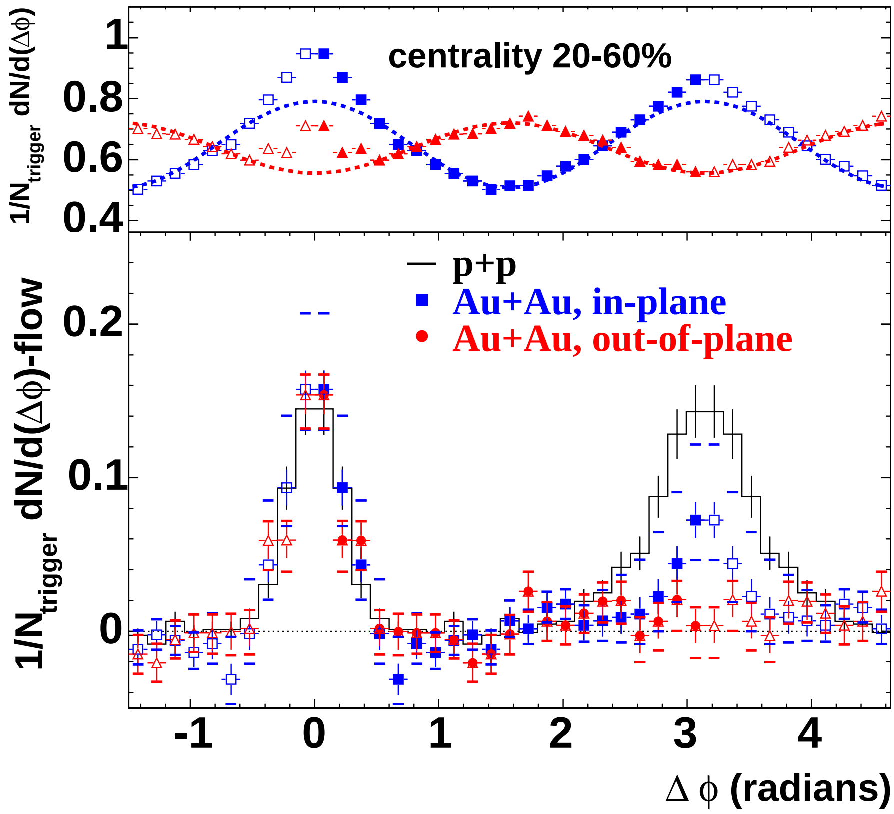

Figure 1.15: top: azimuthal distributions of associated particles for trigger particles in-plane (squares) and out-of-plane (triangles) for Au+Au collisions at centrality 20-60%. Open symbols are reflections of solid symbols around Δ_ϕ=0 and Δ_ϕ=π. The elliptic flow contribution is shown by dashed lines. Bottom: distributions after subtracting elliptic flow, and the corresponding measurement in p+p collisions (histograms) [47].

the hot dense matter formed during the initial stage of heavy ion collisions [48]. Hydrodynamic models predict a large anisotropy in the momentum range p_T<2 GeV/c; this anisotropy is thought to be indicative of early thermal equilibriuum, while the mass dependence of this effect is argued to be a consequence of the formation of a QGP. At large momenta, anisotropy measurements are also important for jet quenching studies (see Sec 1.3.3). As we said before, the spatial anisotropy can be translated into a momentum anisotropy, that can be measured using a Fourier expansion:

$$\frac{d^2n}{p_T dp_T d\phi} \propto \left(1 + 2\sum_n \nu_n \cos n(\phi - \Psi_R)\right) \tag{1.10}$$

where Ψ_R is the reaction plane angle and $\nu_2 = \langle({p_x}^2 - {p_y}^2)/({p_x}^2 + {p_y}^2)\rangle$ has been called "elliptic flow" [49].

Let's represent a non-central $A+A$ collision as an "almond shaped" particle emission source: along the short axis (i.e. in-plane with respect to the reaction plane) the pressure gradient is larger than along the long axis (i.e. out-of-plane), resulting, eventually, in an ellipsoidal final transverse momentum space. This p_T dependence of ν_2 is generated at very early stages of the collision, as predicted by thermodynamic models. In particular, we note that ν_2 is driven by pressure anisotropies, due to spatial deformation of the reaction zone; this deformation quickly disappears and then the elliptic flow is sensitive to the equation of state only during the early expansion stage ($\sim$5 fm/c in semicentral Au+Au collisions [50]).

In fig. 1.16 is showed the dependence of ν_2 on transverse momentum for different species of particles, as measured by STAR and PHENIX experiments at RHIC [53]. It is important to distinguish three different features characterizing ν_2. First, particles exhibit a thermodynamic behaviour in the low p_T region, which means that a common expansion velocity can be identified and that the heavier the particle, the larger the momentum from hydrodynamic motion[18]. Second, at intermediate p_T, ν_2

[18] To be noted that the mass splitting strongly depends on the equation of state [52] and

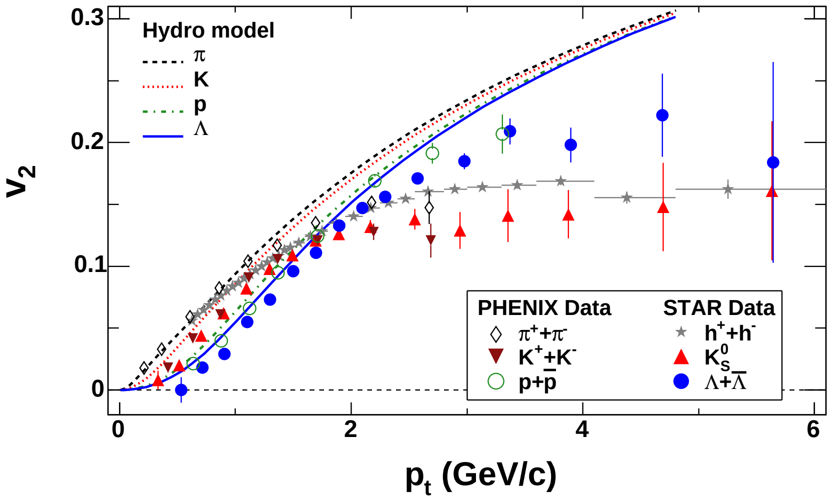

Figure 1.16: the minimum bias ν_2 as a function of p_T; the STAR K^0_s and Λ+$\bar{\Lambda}$ data are from [50], while the PHENIX data can be found in [51]. Hydrodynamic calculations are from [52].

does not strongly depends on p_T. Finally, the ν_2 saturation values for baryons are higher than those from mesons and baryons group togheter, as mesons do. However, the idea that the parton energy loss in the medium created during the collision could be the mechanism underlying the angular anisotropy ν_2 (that is, the effective particle emission should occur from a shell area of the whole volume, because of the quenching of the partons inside the dense medium) is still under discussion.

1.3.5 Hanbury-Brown-Twiss Source Radii

In Astrophysics a method, based on the Hanbury-Brown-Twiss (HBT) effect, is used to measure the size of the stars.

the equation of state including a phase transition describes the observed data better than one without phase transition.

It is based on the fact that the amplitudes of two indistinguishable processes interfere. If an object emits two identical bosons or fermions with momenta $\mathbf{k_1}$ and $\mathbf{k_2}$ which are registered by two detectors, the dependence of the cross section $d^6\sigma/d^3_{k_1}d^3_{k_2}$ on the relative distance between the detectors or on the relative momentum of the registered particles is an image of the emitting source. In heavy-ion physics the situation is much more difficult:

a) there is nothing like a static source which emits particles. The system has a complicated geometrical structure and expands in space and time. Therefore, not only one parameter like in astrophysics the rms radius of a star but the functional dependence of several parameters on time are encoded in the data;

b) there is no unique definition of when a particle is emitted, because the emission is in reality a disconnection from the expanding system. Usually one assumes that after its last collision the particle can be considered as emitted. The space-time point of the last collision is called the freeze-out point;

c) there are long-range Coulomb forces which change the particle momenta after emission [54].

Anyway, informations about the space-time evolution of the system, about the freeze-out volume and about the reaction geometry of heavy-ion collisions can be obtained from studies concerning intensity between identical particles (such as $\pi\pi$, KK and pp pairs[19]). HBT measurements can provide two correlation functions from which it is possible to obtain the longitudinal and the transverse radii, the lifetime and the flow pattern of emitting source (i.e. fireball) at freeze-out[56]. For example, the inverse width R_{out} of the “out” correlation function and R_{side} of the “side” correlation function can be used to extract a measure for the duration of the particle emission $(R^2_{out} - R^2_{side})$

[19]The effect has also been observed in p+$\bar{\text{p}}$ annihilations[55]

and the transverse size of the source (R_{side}) [57, 58]. Besides, the lifetime of the mixed phase after the collision can appear in an enhancement of the ratio of the inverse width (R_{out}/R_{side}) of the two-particle correlation functions in the out- and side-directions [57]. Fig. 1.17 shows the HBT dependence on the transverse mass as recently obtained by STAR at RHIC, from which dynamical information on the particle emitting source can be obtained.

1.4 RHIC Results and Last Models: from QGP to sQGP

The expectations that QGP could be a gas of weakly interacting quark and gluons was washed out by very first experimental data of RHIC. Collective phenomena, such as radial and elliptic flow, reveal "hydro" properties of the QGP, which behave like a good liquid rather than a dilute gas of quasiparticles [60]. The idea was introduced, that plasma at RHIC should be in strongly coupled regime, "sQGP". Although at $T > T_c$ quarks are deconfined, the energy needed for separation of quarks close to T_c is huge (see fig. 1.18a, up to U$\sim$4 GeV). One implication is simple: the charges simply cannot get separated until very high T; the second: as the ratio $U/T \sim 10$ goes into the Boltzmann exponents, any perturbative approach is completely hopeless. There are several reasons which demand such a radical change, from traditional weak coupling to strong coupling methods [61]:

a) collective phenomena observed at RHIC lead to view QGP as a near perfect liquid;

b) Feshbach-type resonances due to marginal states may lead

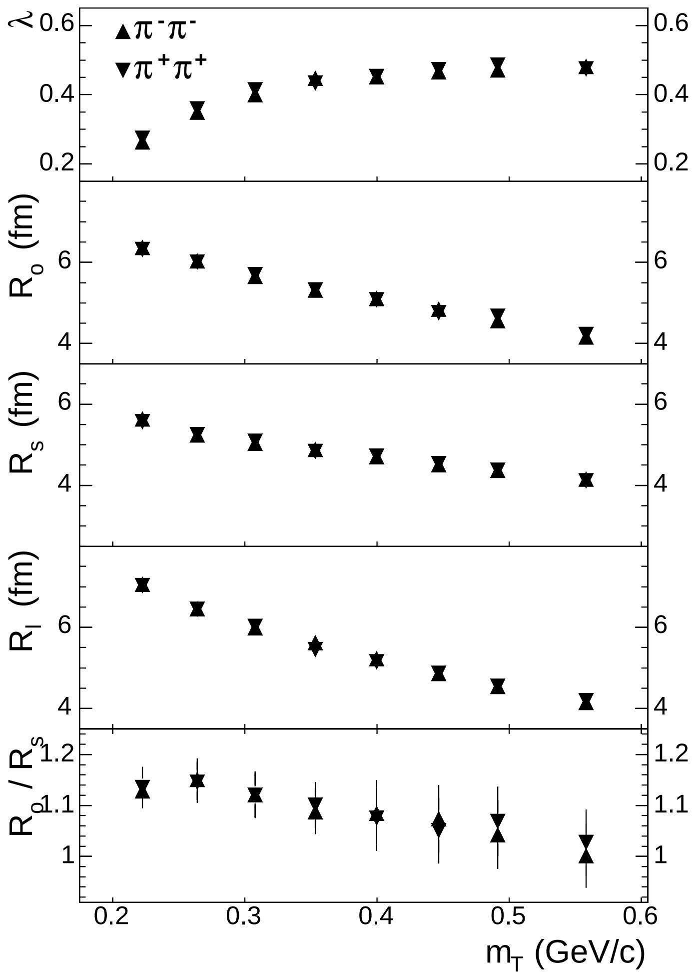

Figure 1.17: HBT parameters for 0-5% most central Au+Au events for $\pi^+\pi^+$ and $\pi^-\pi^-$ correlation functions as obtained by STAR at RHIC. For more details see [59].

to large cross sections;

c) classical electromagnetic plasma can be a good liquid too, if sufficiently strongly coupled;

d) a close relative of QCD, the $\mathcal{N}$=4 supersymmetric Yang-Mills gauge theory can be studied in a strongly coupled $g^2N_c\to\infty$ regime at finite T via the AdS/CFT correspondence: the results are very close to what was observed at RHIC.

It is possible to do a lot of remarks about sQGP, looking at some theories and at the RHIC data:

a) the departure of elliptic flow data from the hydro prediction happens only at rather high p_t~1.5-2 GeV , from which the estimated viscosity-to-entropy ratio η/s=0.1-0.2 is more than an order of magnitude lower than in pQCD;

b) another transport coefficient, the charm diffusion constant D_c deduced from single electron R_{AA}[62, 46, **?**] and ν_2, is also an order of magnitude lower than pQCD estimates;

c) new hydrodynamical phenomenon suggested recently, the *conicalflow*, maybe explains why secondaries from a quenched jet fly preferentially to large angle ≈ 70 degrees consistent with the Mach angle for (time-averaged) speed of sound;

d) combining lattice data on quasiparticle masses and interparticle potentials, one indeed finds a lot of bound states and resonances at $T>T_c$;

e) the same approach explains why η_c , J/ψ remains bound till near $3T_c$, as was directly observed on the lattice;

f) this approach was experimentally demonstrated to work for ultra-cold trapped fermionic atoms Li^6, turning it to near perfect liquid as well when the Feshbach resonance leads to the scattering length $a\to\infty$. Experiments on oscillations found a sharp minimum in damping near the resonance, reducing it by about 2 orders of magnitude. According to studies in two lowest modes are well described by hydro with "*quantum viscosity*" $\eta \approx 0.3\ \hbar$n, in a way nearly as low as that of sQGP;

g) heavy-light resonances in sQGP can explain the value of the charm diffusion constant;

h) the interaction parameter Γ[20] in sQGP is obviously not small. At such Γ the classical strongly coupled e.m. plasma is a good liquid: the same was found in classical version of sQGP

[20] $\Gamma=\langle PE\rangle/\langle KE\rangle$ is defined as the ratio between the average potential energy and the average kinetic energy

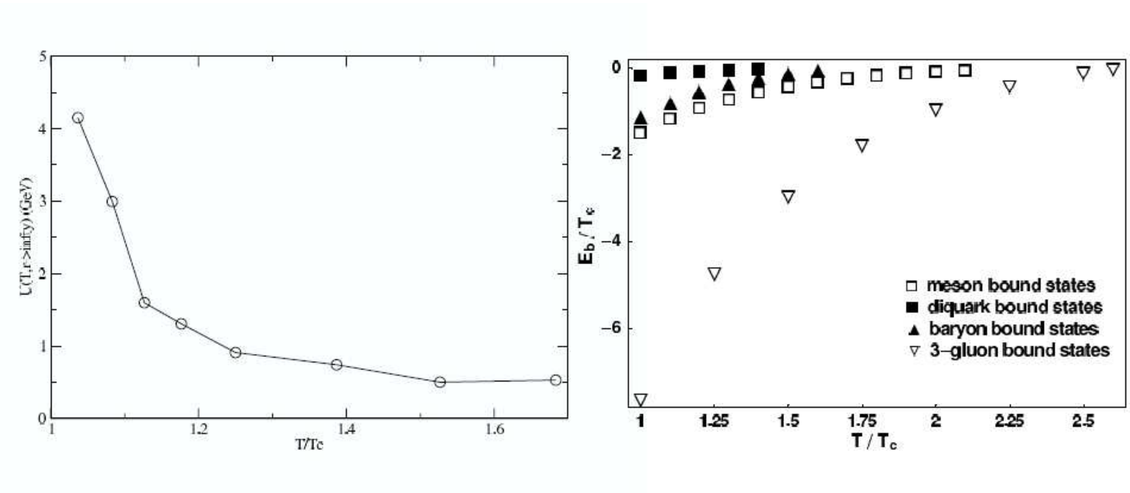

Figure 1.18: a) the separation energy U($T, r \rightarrow \infty$) - U(T, r=0.2 fm) in GeV vs T/T_c, calculated from the free energy by removing the entropy term; b) dependence of various states' binding energy (in units of T_c) on the temperature.

as well;

i) the EoS for finite T N=4 SUSY YM is similar to what is seen on the lattice in the RHIC domain, namely $p/p_{ideal} = [(3/4) + O((g^2 N_c)^{-3/2})]$;

l) at infinite coupling there is a finite limit of viscosity $\eta/s \Rightarrow 1/4\pi$, again close to the RHIC value;

Chapter 2

ALICE and the Time Of Flight (TOF) system

The experiments devoted to the study of heavy-ion physics received a big boost in the last decades, using the existing accelerator facilities, such as the Brookhaven AGS and CERN SPS. The first approches to this kind of physics investigation has been done using fixed-target experiments (such as WA98, NA50 and NA57 at the SPS). Foloowing the encouraging results of these experiments, the need for the construction of accelerators dedicated to heavy-ion collisions has been underlined. In the summer 2000 the *Relativistic Heavy-Ion Collider* (RHIC, [63]) at Brookhaven has started its activities, while it is presently under construction the *Large Hadron Collider* (LHC, [64]) at CERN. At RHIC four experiments are installed: PHENIX, STAR, BRAHMS and PHOBOS; the d+Au and p+p collisions and expecially the Au+Au collisions at $\sqrt{s_{NN}} = 200$ GeV have offered the opportunity to explore new ranges of energies and centralities and to integrate the data from the past experiments. In the future, with a program concerning Pb+Pb collisions at $\sqrt{s_{NN}} = 5{,}5$ TeV, new frontiers can be reached; four experiments will be operating on the LHC facility: ALICE, ATLAS (A Toroidal LHC ApparatuS), CMS (Compact Muon Spectrometer) and LHCb (LHC beauty). In table 2.1 we show a comparison among some important collision parameters for SPS, RHIC and LHC[1]. The LHC values stay well above those referred to the other accelerators, while the formation time τ_0 is ~ 3 times smaller.

Collisions Parameter	SPS	RHIC	LHC
$\sqrt{s_{NN}}$ (GeV)	17	200	5500
$dN_{ch}/d\eta$	500	850	$2 \div 8\times10^3$
ϵ (GeV/fm^3)	2.5	$4 \div 5$	$15 \div 40$
V_f (fm^3)	10^3	7×10^3	2×10^4
τ_{QGP} (fm/c)	≤ 1	$1.5 \div 4.0$	$4 \div 10$
τ_0 (fm/c)	~ 1	~ 5	≤ 0.2

Table 2.1: central collision parameters for the SPS, RHIC and LHC accelerators

This improvement with respect to SPS and RHIC allows LHC to investigate new regimes in heavy-ion particle physics, in terms of centre-of-mass energy, the energy density, the lifetime and the volume of the deconfined system created in the collision. Another difference between the past accelerators and LHC will be the charged particle multiplicity, that is 600 at RHIC and will range from 1500 to 4000 at LHC [65, 66, 67]. Finally it is interesting to note the value of the expected luminosity for Pb+Pb collisions at LHC that is 10^{27} cm$^{-2}s^{-1}$, which means a rather low minimum-bias intaraction rate of about 8 kHz.

[1] $\sqrt{s_{NN}}$ is the energy per nucleon pair in the centre-of-mass, $dN_{ch}/d\eta$ is the charged particle multiplicity density per pseudorapidity unit, ϵ refers to the energy density at initial thermalization, V_f is the volume at freeze-out, τ_{QGP} indicates the duration of hte QGP phase, and τ_0 is the time of initial thermalization.

2.1 A Large Ion Collider Experiment

The ALICE detector is designed to address and correlate a wide palette of physics observables, related to heavy-ion collisions with an energy value in centre-of-mass of 5.5 TeV per nucleon pair. Here there is a list of the observables that ALCE can provide:

- hadrons ratios;
- transverse momentum p_T spectra (temperature and dynamical fluctuations, collective flux and jet quenching);
- particles interferometry (expansion development);
- multiplicity fluctuations;
- direct photons (thermic radiation);
- vector mesons (ρ, ω, ϕ, J_ψ) decays in leptons pairs (resonances parameters, chiral symmetry restoration and deconfinement);
- *open charm* (D$\rightarrow$Kπ) and *beauty* production;
- $\phi \rightarrow K^+K^-$ decay.

It is very interesting the study of the particle correlation, because this allows to obtain informations about the dynamic evolution of the system, such as the decoupling time, the duration of the particles emission and the existence of collective fluxes. The particle identifiaction (PID) has a very important role in an experiment like ALICE; moreover the hadron identification event-by-event allows us to perform measurements with a big statistics:

- the transverse momentum p_T distribution for pions, kaons and protons;

- the ratio π/K/p.

It is very important to investigate the QGP signatures, as said in chapter1. In ALICE there are two detectors dedicated to PID:

- a Time Of Flight (TOF) system, optimized for a big acceptance and for a high K/π discrimination power in the range $0.5 \div 2.5$ GeV/c and K/p up to 4 Gev/c;
- a more little system, used for inclusive measurements, for the π/K/p identification in a range $1.5 \div 5$ GeV/c.

In particular, the TOF will cover a hadrons momentum range from $\sim$ 0.5 GeV/c (above limit of ITS and TPC for the energy loss measurements dE/dx, for K/π discrimination) to 2.5 GeV/c (statistic limit in single events). In fig. 2.1 the discrimination π/K/p vs momentum for the TOF, for a distance of 3.7 m from the vertex is showed; this is for a particle emitted with an angle of 90° and for different values of time resolution. To allow a 3σ separation, in the selected momentum range, a global time resolution of 100 ps is needed for the TOF system.

2.2 The ALICE Layout

The ALICE experimental apparatus consists of two main components: a central detector and a muon arm. The central detector, covering mid-rapidity ($|\eta|$<0.9) over full azimuth, is contained inside a magnetic field |B|<0.5 T; it is mainly addressed to particle tracking and PID. The muon arm, covering the pseudorapidity interval -2.4 < η < -4.0, consists of a hadron

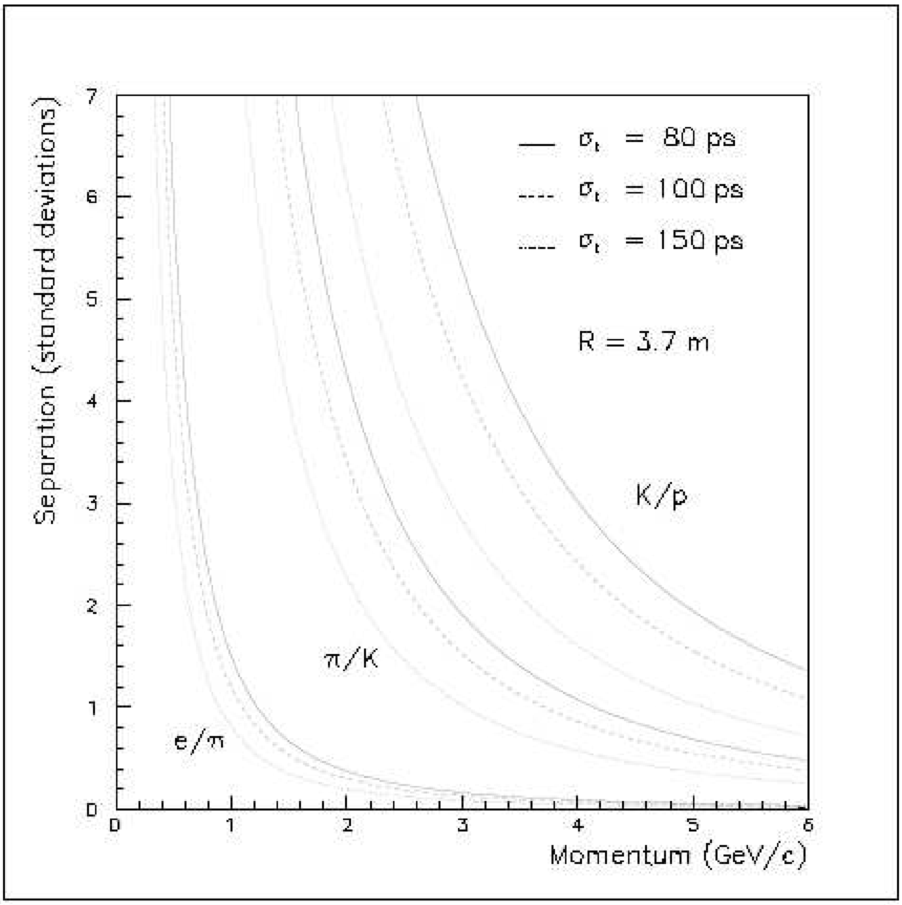

Figure 2.1: particles discrimination with TOF technique for different time resolution of the detector.

absorber positioned very close to the interaction region, a spectrometer made of a dipole magnet with a field integral of 3 Tm and five tracking stations, a second iron filter and two trigger stations. Besides the central detector and the muon arm, the ALICE apparatus also includes a set of forward detectors. The apparatus is completed by an array of scintillators for triggering on cosmic rays (ALICE COsmic Rays DEtector, ACORDE).

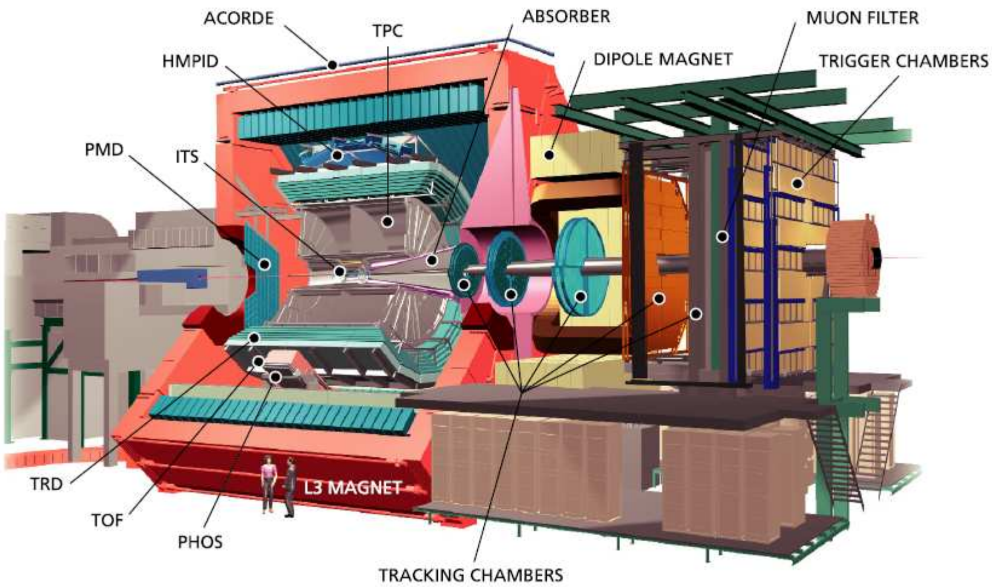

Figure 2.2: layout of ALICE detector; for the sake of visibility, the HMPID detector is shown in the 12 o'clock position instead of the 2 o'clock position in which it is actually positioned

2.2.1 Inner Tracking System - ITS

The basic functions of the Inner Tracking System (ITS) are achived with six barrels of high resolution detectors mounted within the radial distance between 4 and 45 cm; these functions are:

- primary vertex with a resolution better than 100 μm ;
- secondary vertex reconstruction of charm and hyperon decays;
- tracking and PID of low-momentum particles;
- reconstruction of momenta of particles with low energy and their identification with energy loss measurements $\mathrm{d}E/\mathrm{d}x$, in the dead regions of TPC.

The number of layers and their position has been optimized for efficient pattern recognition and impact parameter resolution. Because of the high particle density, the four innermost layers (r $\leq$ 24 cm) must be truly two-dimensional devices, e.g. silicon pixel (SPD) and silicon drift (SDD) detectors. The outer superlayer at r $\approx$ 45 cm will be equipped with double-sided silicon micro-strip (SSD) detectors. With the exception of the two innermost pixel planes, all layers will have analog readout for indipendent particle identification via $\mathrm{d}E/\mathrm{d}x$ in the non-relativistic region, which will give the inner tracking system a stand-alone capability as a low-p_T ($p \leq 500$ MeV/c for kaons and pions and $p \leq 1$ GeV/c for protons) particle spectometer.

2.2.2 Time Projection Chamber - TPC

As said before, the charged particle multiplicity will be 1500 $\div$ 4000 at LHC; so, an efficient and robust tracking is needed, leading to the choice of a TPC as the main tracking system. The Time Projection Chamber (TPC) is cylindrical in shape and has an inner radius of about 85 cm, an outer radius of about 250 cm and an overall lenght along the beam direction of 500 cm. The detector is made of a large field cage, filled with 88 m^3 of Ne/CO_2 (90%, 10%), which is needed to transport the primary electrons over a distance of up to 2.5 m on either side of the central electrode to the end-plates. Multi-wire proportional chambers with cathode pad readout are mounted into 18 trapezoidal sectors of each end-plate. They have an overall active area of 32.5 m^2. Because of the radial dependence of the track density, the readout is segmented radially into two readout chambers with slightly different wire geometry adapted to the varying pad sizes mentioned below. In total, the TPC has about 560000 readout channels, provided with highly-integrated electronics. The inner radius of the TPC ($r_{min} = 85$ cm) is given by the maximum acceptable hit density (0.1 cm^{-2}). The outer radius ($r_{max} = 250$ cm) is determined by the lenght required for a dE/dx resolution $< 7\%$. With this resolution, in addition to its tracking function, the TPC can serve as a detector for electron identification up to momenta of ~ 2.5 GeV/c. Moreover, the TPC will provide PID for low-p particles (for example in the range $0.4 < p < 0.5$ GeV/c for pions). The design of the readout and of the end plates, based on ongoing developments for other heavy-ion TPCs, as well as the choice of the operating gas, has been optimized for good double-track resolution.

2.2.3 Transition Radiation Detector - TRD

The Transation Radiation Detector (TRD) provides the identification electron identification in the central barrel for momenta greater than 1 GeV/c, where the discrimination e/π via dE/dx in the TPC is no longer sufficient. Moreover, the TRD can provide a discrimination electrons/hadrons between $\sim$ 1 GeV/c and $\sim$ 100 GeV/c. Since the TRD is a fast tracker, it can be used as an efficient trigger for high-transverse-momentum electrons. Such a trigger will considerably enhance the recorded Υ yields in the high-mass part of the dilepton continuum as well as high-p_T J/ψ. The coverage in pseudo-rapidity matches the coverage of the other central barrel detectors, $|\eta|\leq 0.9$. The TRD fills the radial space between the TPC and the TOF detectors. For the quality of electron identification, the TRD consists of six individual layers. To match the azimuthal segmentation of the TPC, there are 18 sectors. There is a 5-fold segmentation along beam direction, z. In total there are $18 \times 5 \times 6 = 540$ detector modules. Each module consists of a radiator of 4.8 cm thickness, a multi-wire proportional readout chamber and a front-end electronics for this chamber. Each chamber has 144 pads for the induced signal readout, in the direction of the amplification wires, rφ, and between 12 and 16 pad rows in the z direction. The gas mixture in the readout chambers is Xe/CO_2 (85%, 15%). At extreme multiplicity ($dN_{ch}/d\eta = 8000$) the pixel occupancy will be 34%. A space-point resolution in the bend direction of 400 μm can be achieved for low multiplicity ($dN_{ch}/d\eta = 2000$) at $p_T = 1$ GeV/c. For full multiplicity this resolution is degraded to 600 μm after unfolding.

2.2.4 Time Of Flight - TOF

The Time Of Flight (TOF) detector[2] of ALICE is a large-area array that covers the central pseudo-rapidity region ($|\eta| \leq 0.9$) for PID in the intermediate momentum range (few hundred MeV/c to few GeV/c). It has a modular structure corresponding to 18 sectors in the azimuthal angle φ ($0° \leq \varphi \leq 360°$) and to 5 segments in the longitudinal coordinate along the beam axis z. The whole device is locate inside a cylindrical volume with an internal radius of 370 cm and an external radius of 399 cm. Three different types of modules are needed to cover the full lenght of the cylinder. They all have the same structure and width ($\sim$ 128 cm) but differ in lenght. The actual dimensions are de-

[2] a detailed description is the subject of the next chapter

fined in such a way that the joining areas of the modules are aligned with the dead of the other detectors projected from the interaction point, thus creating a configuration of minimal disturbance for the external detectors. The central module is 1.17 m long, the intermediate ones are 1.57 m long and the external ones are 1.77 m long. The overall TOF barrel is $\sim$ 745 cm. The granularity of the TOF detector is given by the requirement to identify, on an event-by-event basis, as many charged particles as possible up to the highest expected charged-particle multiplicity density ($dN_{ch}/d\eta = 8000$). Detailed simulation studies have shown that, with the chosen pad size of 3.5×2.5 cm^2 and the tilted-strip geometry, the occupancy of the detector is $\sim$ 16%, at the highest charged particle density (including secondary particles) with a magnetic field of 0.2 T. Lower values of the particle or higher values of the magnetic field improve the occupancy ($\sim$ 7% for $dN_{ch}/d\eta = 4000$ and B = 0.2 T; $\sim$ 13% for $dN_{ch}/d\eta$ =8000 and B = 0.4 T) as expected. The detector has about 1.6×10^5 readout channels. Since the two main requirements for the TOF detector are a time resolution lower than 100 ps and a very high granularity, a gauseous detector has been chosen. The TOF technology is based on the double-stack Multigap Resistive Plate Chamber (MRPC); the gas mixture in the active area of the detector is $C_2F_4H_2/C_4H_{10}/SF_6$ (90%, 5%, 5%).

2.2.5 High Momentum Particle Identification Detector - HMPID

The High Momentum Particle IDentification (HMPID) is dedicated to inclusive measurements of identified hadrons for p_T up to 5 GeV/c in a small acceptance window. It was designed as a single-arm array with an acceptance of 10% of the central barrel. The HMPID is based on proximity-focusing Ring Imaging Cherenkov (RICH) counters and consists of seven modules of about 1.5×1.5 m^2 each, mounted in an independent support cradle at a distance of about 4.8 m from the vertex. The cradle will be fixed to the space frame in the two o'clock position. The detector has in total about 1.6×10^5 readout pads and 48 channels are multiplexed to one 12-bit ADC. Besides, Cherenkov photons are detected by a photon counter which uses the new technology of a thin layer of CsI deposited onto the pad cathode of a Multi-Wire Pad Chamber (MWPC).

2.2.6 PHOton Spectrometer - PHOS

The PHOton Spectrometer (PHOS) is a high resolution spectrometer which will detect electromagnetic particles over a limited acceptance at central rapidity and provides photon identification as well as neutral meson identification through the two-photon decay channel. The aim of the PHOS is to test the thermal and dynamical properties of the very first stages of the collision and to study jet quenching as a QGP signal. PHOS is subdivided into five indipendent units (modules), positioned on the bottom of the ALICE setup at a distance of 460 cm from the interaction point. It will cover approximately a quarter of a unit in pseudo-rapidity ($|\eta| \leq 0.12$) and 100° in azimuthal angle. Its total area will be ~ 8 m^2. Each channel consists of $22 \times 22 \times 180$ mm^3 lead-tungstate crystal, $PbWO_4$ (PWO), coupled to a 5×5 mm^2 Avalanche Photo-Diode (APD) and a low-noise preamplifier. The total number of crystals in PHOS is 17920 representing a total volume of ~ 1.5 m^3. Each PHOS module is equipped with charged particle veto detector, a Multi-Wire Proportional Chamber (MWPC) with cathode-pad readout.

2.2.7 Forward Detectors

Some smaller detectors will be placed at large rapidity values, far away from the interaction point.

- **Forward Muon Spectrometer**

  As said in the previous chapter, the study of the spectrum of heavy quark vector mesons (J/ψ, ψ', Υ, Υ', Υ'') is an important point in the search for the formation of a deconfined state. It is possible to have informations about this spectrum and about the ϕ meson via the $\mu^+\mu^-$ decay channel, using the Muon Spectrometer, placed in the region $2.5 < \eta < 4.0$. In fig. 2.3 the dimuon mass spectra in two different mass regions is showed. The spectrometer consists of the following components: passive front absorber to absorb hadrons and photons from the interaction vertex; high-granularity tracking system of ten detection planes; large dipole magnet; passive muon filter wall, followed by four planes of trigger chambers; inner beam shield surrounding the beam pipe to protect the chambers from particles produced at large rapidities. The design of the tracking system is driven by two main requirements: a spatial resolution of about 100 μm and the capability to operate in a high-particle-multiplicity environment. For central Pb+Pb collisions, a few hundred particles are expected to hit the muon chambers, with a maximum hit density of about 5 $\times$ 10^{-12} cm^{-2}. Moreover, the tracking system has to cover a total area of about 100 m^2. All these requirements can be fulfilled by the use of cathode pad chambers. They are arranged in five stations: two are placed before, one inside and two after the dipole magnet. Each station is made of two chamber planes; each chamber has two cathode planes, which are both read out to provide two-dimensional hit information. The first station needs to be flush with the absorber to measure the exit points of the muons as precisely as possible. To keep the occupancy at a 5% level, a large segmentation of the readout pads is needed; more the distance from the beam, more the dimension of the pads and the total number of channels is about one million. The trigger system consists of four Resistive Plate Chamber (RPC) planes arranged in two stations, one metre apart from each other, placed behind the muon filter. The total active area is 150 m^2.

- **Zero Degree Calorimeter - ZDC**

  Zero Degree Calorimeter (ZDC) will detect spectator nucleons. It will be placed at 116 m from the interaction point. It is composed by two calorimeters: one, placed at zero degree relative to the LHC beam axis, for neutrons and one, placed on the side where positive particles are deflected, for protons. The calorimetry technique used is the following: incident particles generate a shower in a dense absorber (the "passive" material); the shower produce Cherenkov radiation in some quartz fibres (the "active" material) all placed

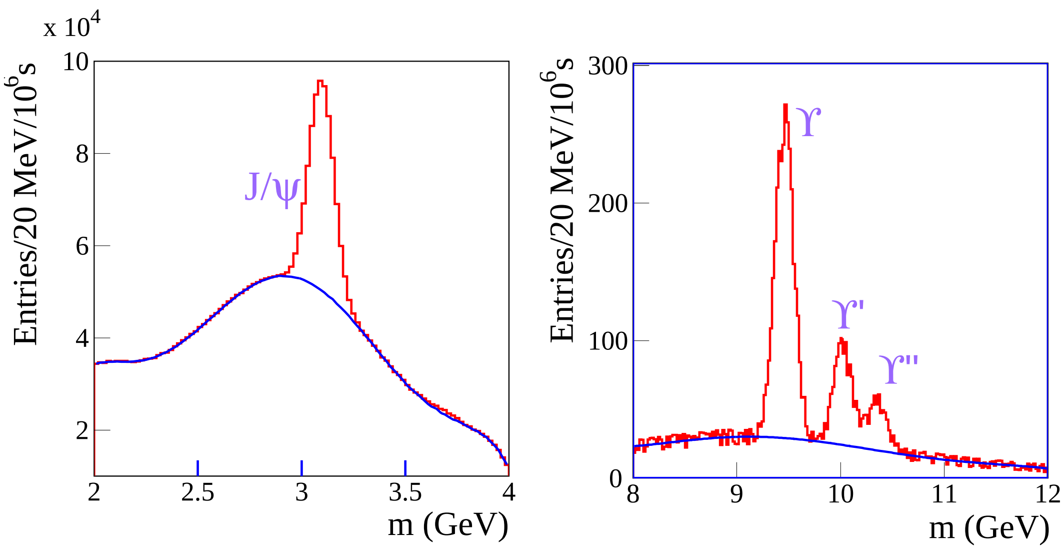

Figure 2.3: opposite sign dimuon mass spectra in the region $2 < m < 4$ GeV (left) and $8 < m < 12$ GeV (right) for the 10% most central Pb+Pb reactions [68]; the centrality definition in terms of percentage refers to the total Pb+Pb inelastic cross-section σ^{inel}_{Pb+Pb}.

inside in the absorber.

- **Photon Multiplicity Detector - PMD**

  The Photon Multiplicity Detector (PMD) will measure the multiplicity and spacial (η - ϕ) distribution of photons on an event-by-event basis; besides it will carry out informations about the formation of the Disoriented Chiral Condensate (DCC) [69], about event-by-event fluctuations, flow, transverse electromagnetic energy and reaction plane. PMD is located at 360 cm from the interaction point, on the opposite side of the forward muon spectrometer, covering the region $2.3 < \eta < 3.5$. It has about 2.2×10^5 readout channels using an electronics similar to that of the muon tracking chambers.

- **Forward Multiplicity Detector - FMD**

  The Forward Multiplicity Detector (FMD) consists of five silicon-strip ring counters placed on both sides of the interaction point, covering the pseudo-rapidity range -3.4 $< \eta <$ -1.7 and 1.7 $< \eta <$ 5.1 for charged-particle multiplicity measurements. It has in total about 5×10^4 channels.

- **V0 Detector**

  The V0 detector is made of two scintillator arrays located asymmetrically on each side of the interaction point at 355 cm and -90 cm, respectively. It rejects the beam-gas interactions by measuring the time difference between the two arrays and measures the charged-particle multiplicity using the signal amplitude. The V0 signals partecipate in the L0 decision (fast trigger in ALICE).

- **T0 Detector**

  The T0 detector consists of two arrays of 12 Cherenkov counters each, read out by fine-mesh photomultiplier tubes. The arrays are placed on both sides of the interaction point, at 350 cm and -70 cm. This detector has to provide the start-time signal for the TOF detector, discriminate against beam-gas interactions and sample particle multiplicity; it provides inputs for the level 0 trigger (L0) decision too. In addition, the T0 detector sends the pre-trigger signal to the TRD.

2.2.8 ALICE COsmic Rays DEtector - ACORDE

The use of large underground high-energy physics experiments, for cosmic ray studies, has been used, in the past, at CERN, in order to measure, precisely, the inclusive cosmic ray flux in the energy range from $2 \times 10^{10} \div 2 \times 10^{12}$ eV. ACORDE will act as L0 cosmic ray trigger and, together with other ALICE apparatus, will provide precise information on cosmic rays with primary energies around $10^{15} \div 10^{17}$ eV. ACORDE is an array of plastic scintillator modules placed on the top 3 sides of the central ALICE magnet.

2.2.9 Magnet

The optimal choise for ALICE is a large solenoid with a weak field. The choise of a weak and uniform solenoidal field together with the continuous tracking in the TPC eases the task of pattern recognition. The field strenght of 0.2 T is a compromise between momentum resolution, low momentum acceptance and tracking efficiency. The inner radius of the magnet must be large enough to accomodate a single-arm electromagnetic calorimeter for prompt photon detection, which must be placed at a distance of ~ 5 m from the vertex because of the particle density. The magnet of the LEP L3 experiment fulfills all these requirement.

2.3 Particle Identification and Time Of Flight technique

Particle identification (PID) is an important design feature in most experiments. The techniques used should be non destructive and should in addition introduce as little radiation length

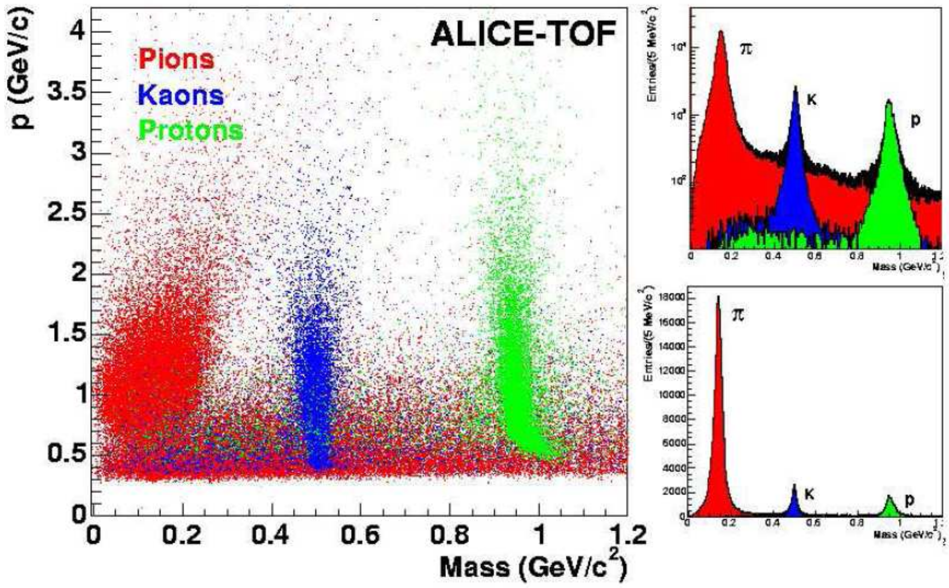

Figure 2.4: Pion-Kaon separation by different PID methods: the length of the detectors needed for 3 sigma separation.

or interaction length as possible. A graphic representation of the different identification techniques is given in figure 2.4.

The simultaneous measurement of the momentum of the particle together with its mean energy loss, dE/dx, in the tracking chambers has been used to estimate the mass of the particle. The dE/dx detectors have gradually improved. By including the particle energy loss measurements in the silicon vertex detectors, the usefulness of the method has been greatly enhanced towards lower momenta. Another technique for PID exploits the Cherenkov effect through the Ring Imaging Cherenkov detectors: the velocity v of a charged fundamental particle is determined by an indirect measurement of the Cherenkov angle, θ_c, i.e. the angle between the emitted Cherenkov radiation and the particle path; it exploits more or less all the properties of Cherenkov radiation (that is, the existence of a threshold, the dependence upon the numbers of photons, the dependence on the charge of the particle and the dependence of the Cherenkov angle. A very powerfull PID technique is the Time Of Flight technique, that is based on the measure of the time of flight of a charged particle that passes through the detector with a velocity v on a known distance L.

ALICE has two detector systems dedicated exclusively to PID: a TOF array optimized for large acceptance and average momenta below 2.5 GeV/c and a small system specialized in higher momenta (HMPID). Track finding in heavy-ion collisions at the LHC presents a big challenge, due to the extremely high track density. In order to achieve a high granularity and a good two-track separation, three-dimensional hit information is used, wherever feasible, with many points on each track and a weak magnetic field. The need for a large number of points on each track has led to the choise of a TPC as the main tracking system.

All the basic physics goals, briefly recalled above, demand a TOF detector with outstanding intrinsic characteristics. The TOF rapidity acceptance has to be large enough to cover the full central accepatance of ALICE, in order to allow a significant study of the observables of interest on an E-by-E basis. This implies that a large number of hadrons of average momenta $\sim$ 1 GeV/c should be measured.

To evaluate the influence of different parameters of the TOF system on the PID quality, let us consider the following expression:

$$m = p\sqrt{\frac{t^2}{l^2} - 1} \tag{2.1}$$

where m is the mass of the particle, p the momentum, t the time-of-flight and l the track lenght. From this expression, it is possible to obtain the mass resolution:

$$\frac{dm}{m} = \frac{dp}{p} + \gamma^2 \left(\frac{dt}{t} + \frac{dL}{L} \right) \tag{2.2}$$

where γ=1/$\sqrt{1-\beta^2}$ is the Lorentz of the particle. Due to the fact that, in the most of the cases $\gamma^2 \gg 1$, if p is known with an accurancy dp/p=1% and if dL/L=10^{-3}, then dm/m is determined by the time resolution of the detector. The difference between the time-of-flight of two particles with the same momentum and the same track lenght, is ($p \gg m$):

$$c\Delta t = \frac{L(m_1^2 - m_2^2)}{2p^2} \tag{2.3}$$

It is simple to show that the $\partial m/m$ resolution has three main contributions:

$$\frac{\partial m}{m} = \frac{\partial p}{p}$$
$$\frac{\partial m}{m} = \left(\frac{E}{m}\right)^2 \frac{\partial t}{t}$$
$$\frac{\partial m}{m} = \left(\frac{E}{m}\right)^2 \frac{\partial l}{l}$$

and that at relatively high momenta, it is driven much more by the errors on the time-of-flight and track lenght than by the error on the momentum determination. The capability to discriminate two particles in a TOF system is given by:

$$n_{dt,1-2} = \frac{L(m_1^2 - m_2^2)}{2p^2 c dt} \tag{2.4}$$

where $n_{dt,1-2}$ is the separation expressed as standard deviations.

2.4 An overview of the TOF detector of the ALICE experiment

The separation of kaons from pions up to 2.5 GeV/c or protons from kaons up to 4 GeV/c requires a global time resolution $\simeq$ 100 ps, while a high segmentation is required to match the high multiplicity that characterizes heavy-ion collisions at the energies of LHC. The TOF chooses as detector the Multigap Resistive Plate Chamber (MRPC), offering an excellent time resolution combined with a high efficiency. The TOF detector was proposed in 1999 with the purpose of providing the ALICE experiment with the best instrument for identifying charged particles over the full central region, in the intermediate momentum range above the ITS/TPC PID capability and partly overlapping the HMPID higher momentum range.

2.4.1 TOF system

The physics goals of the TOF detector have dictated the following requirements:

- large acceptance ($\sim$ the two central rapidity units)
- high efficiency ($> 95\%$)
- excellent intrinsic time resolution (< 100 ps)
- high granularity/low occupancy ($\sim 10^5$ channels)
- rate capability adequate to the ALICE environment ($\leq$ 50Hz/cm^2)
- good uniformity of response
- modularity and simplicity of construction

Detector Layout

During the intensive R&D activity of the last years, several details of the final detector has been studied and the final model of the detector uses strips of the gaseous detector MRPC, with ten gaps in the double-stack configuration (see next chapter). The ALICE TOF is arranged in 18 supermodules, covering 360^o in azimuth and $|\eta| < 1$, for a total area of $\simeq 150$ m^2. Each supermodule is made of five modules, containing a number of MRPC strips ranging from 15 to 19 (see fig 2.5 for a complete vision of the TOF system). Each MRPC strip (whose dimensions are 120×13 cm^2) contains two stacks of resistive glass plates, spaced one from other with equal sized spacers, creating a series of uniform gas gaps with voltage applied to the external surfaces. Electrodes are connected to the outer surfaces of the stack of resistive plates while all the internal plates are left electrically floating. The MRPC stack is made of six glasses forming five gaps. Each gap has a width of 250 μm and is filled with a gas mixture $C_2F_4H_2$ (90%)-C_4H_{10} (5%)-SF_6(5%). The total number of TOF MRPC strips is 1638.

Detector Performance

During last years several beam-tests have been performed to improve the detector performance and to select the construction procedures. In fig. 2.6 it is showed the efficiency and the time resolution as a function of the applied voltage; the efficiency exceeding 99.5 % and the time resolution as low as 50 ps of the MRPC strips are key ingredient for the TOF successful charged particle identification. Also an ageing test has been performed to the CERN GIF and no efficiency or time resolution degradation occurred (see next chapter for detailed beam-tests description).

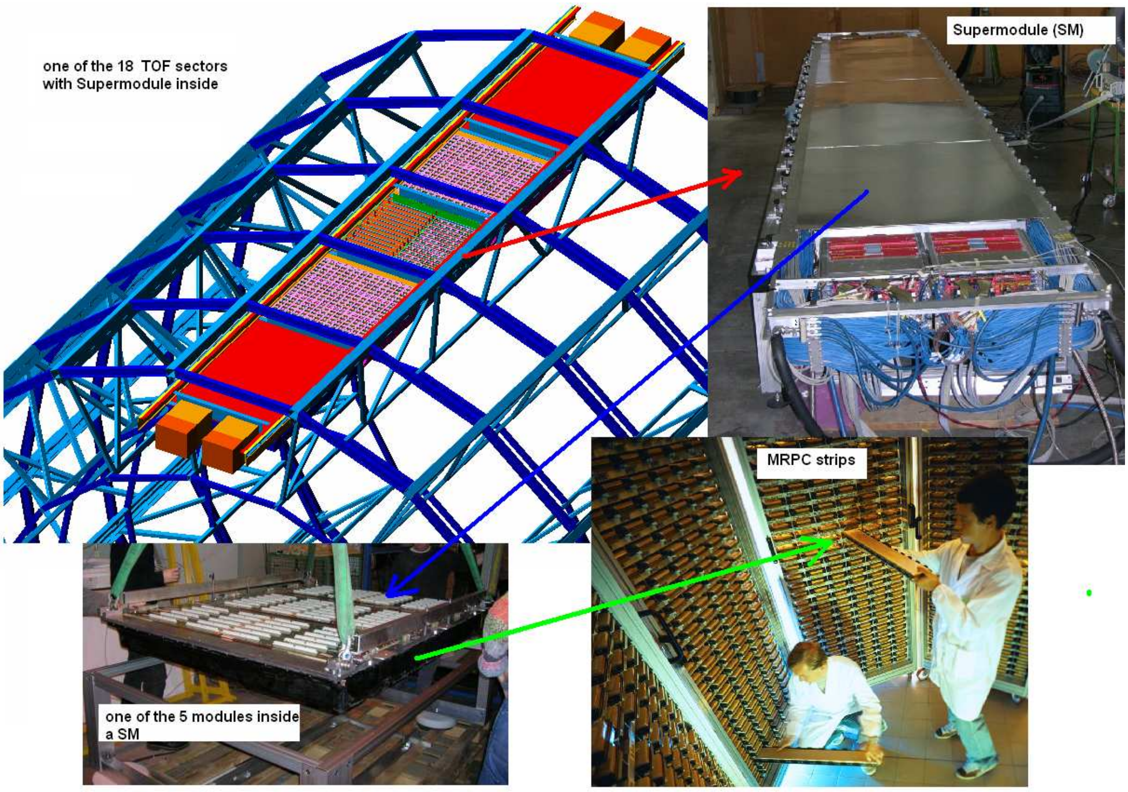

Figure 2.5: the frame that hosts the TOF system, divided in 18 sectors; one SM is shown in a sector of the frame and separately in the construction area; also one of the 5 modules composing a SM and the MRPC strips (in the storage strucutre) are visible

Detector Electronics

The front-end electronics of the TOF is based on Front-End ASIC (FEA) card, based on a dedicated chip (NINO ASIC); Each FEA hosts three NINO ASICs (see fig 2.7), reading 8 MRPC channels (pads) each. The NINO ASIC is extremely fast and low noise and it matches with the pad capacitance and provides a differential LVDS output. Each FEA is equipped with a VHDCI (Very High Density Cable Interconnect) connector: a dedicated 24 pair cable transmits the hits to the TDC readout electronics.

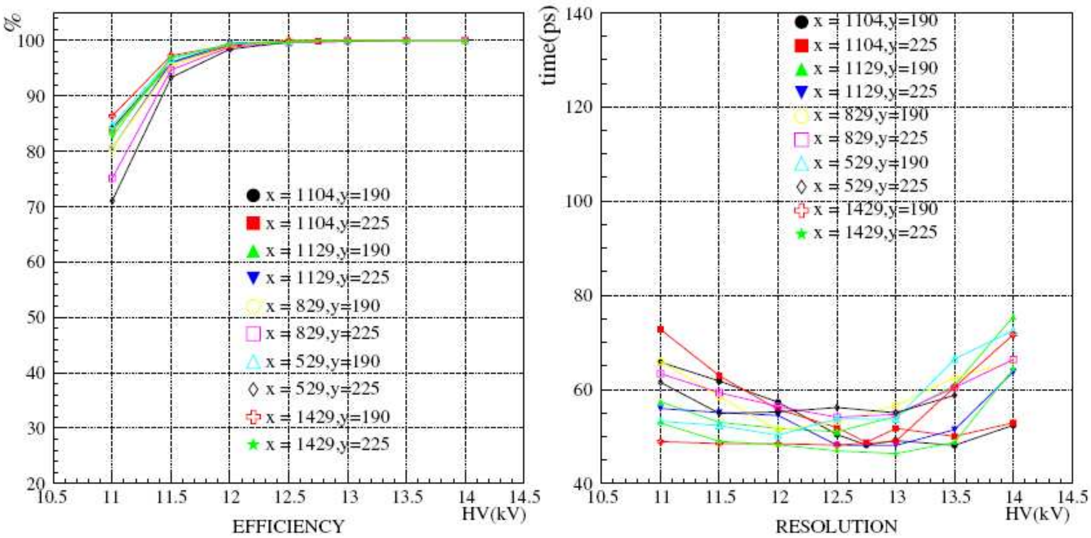

Figure 2.6: MRPC efficiency (left) and time resolution (right) measured at one of the beam-tests at CERN Protosynchrotron (PS)

Each supermodule is equipped with two VME (Virtual Machine Environment) crates per side. Each crate pair is equipped with these boards:

- 19 TDC Readout Modules (TRM), each one hosts 30 8-channel HPTDC (High Performance TDC) chips, developed by CERN microelectronics group (the resolution of the chip is 25 ps)
- 2 Data Readout Module (DRM) that perform the readout
- 1 Clock and Pulser Distribution Module (CPDM) for that provides the LHC clock to the supermodule and a pulse directly to the pads of the MRPC strips
- 2 Local Trigger Module (LTM) that provide the voltage threshold to the FEAs, performs detector monitoring (temperature, low voltage, thresholds) and handles the signals to be sent to the TOF trigger main board

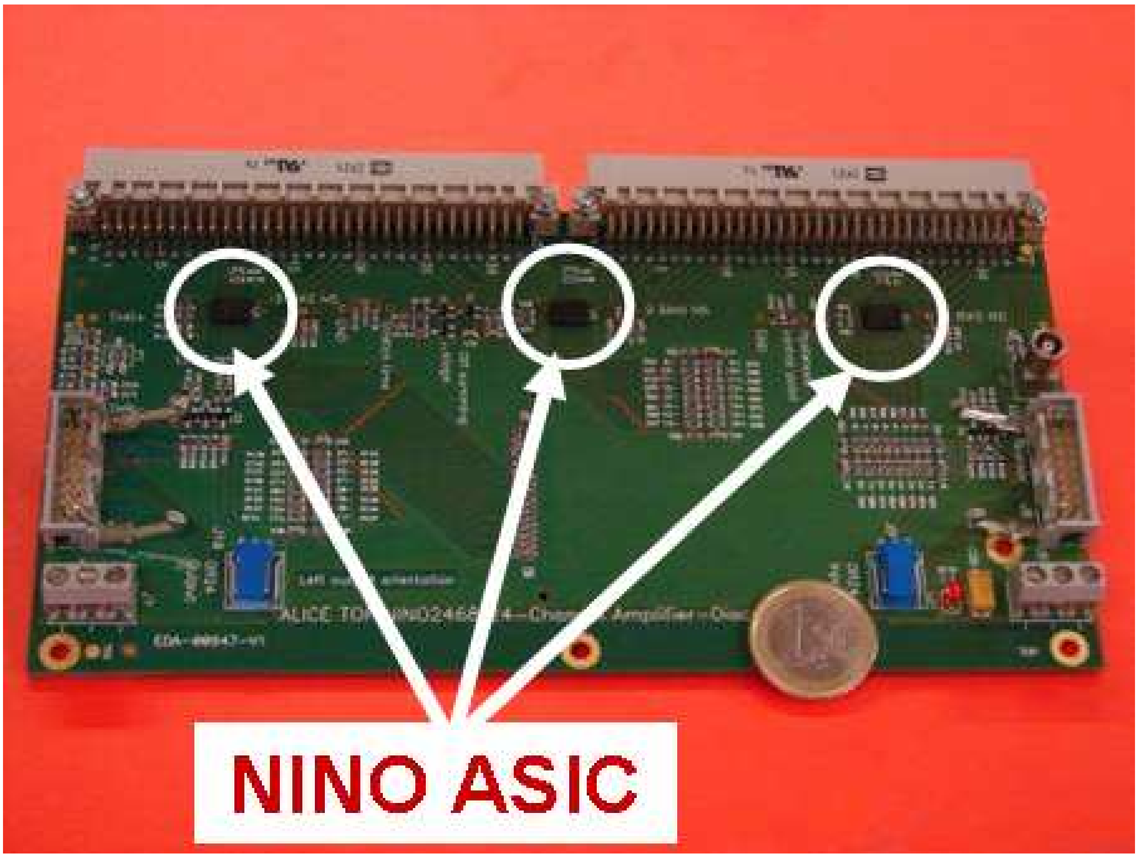

Figure 2.7: the Front-End ASIC card hosting NINO ASIC chips for the signal discrimination and amplification)

Detector Construction

The construction of the detector is a complex sequence of steps: the production and the test of a very large number of MRPC strips (1638 strips constructed in the INFN-Bologna laboratories); the production of the front-end and the readout electronics; the construction and the test of the modules containing the MRPC strips; the assembly of the modules to have the final configuration of the supermodules; the test of the supermodules (see the next chapter); the last step is the installation of the supermodules in the ALICE pit and the tests after the installation. All the 18 supermodules have been constructed and installed in the pit.

In table 2.2 an overview of the TOF parameters is showed.

2.4.2 Multigap Resistive Plate Chamber

The requirements of ALICE experiment make the use of scintillators and phototubes prohibitive for a TOF system that has to cover $\sim$ 176 m^2, because of the price. Gaseous detectors were obvious candidates and the MRPC strips are the last step of R&D started with Pestov counter, Parallel Plate Chamber (PPC) and Resistive Plate Chamber (RPC). All these gaseous detectors are of the parallel plate chamber design. The key aspect of these detectors is the that the electric field is high and uniform over the whole sensitive gaseous volume of the detector. Any ionisation produced by a through-going charged particle will immediately start a gas avalanche process which will eventually generate the observed signals on the pick-up electrodes[3].

History Of Parallel Plate Chamber Design

Pestov Spark counter

The Pestov Spark Counter is a single-gap, gaseous parallel-plate detector working in the streamer/spark mode. It features the use of a semi-conductive anode and of a special gas mixture that keeps the discharge local and enables a high global counting

[3]there is no time drift associated with the movement of the electrons to a region of high electric field; thus the time jitter of these devices is caused by the fluctuations in the growth of the avalanche

Pseudo-rapidity coverage	$-0.9 < \eta < 0.9$
Azimuthal coverage	2π
Radial position	3.70 < r < 3.99
Lenght	7.45 m
Segmentation in ϕ	18-fold
Segmentation in z	5-fold
Total number of modules	90
Central module (A)	117×128 cm^2
Intermediate module (B)	157×128 cm^2
External module (C)	177×128 cm^2
Detector active area	141 m^2
Detector thickness radially	$X/X_0 = 20\%$
Number of MRPC strips per module	15(A),19(B),19(C)
Number of readout pads per MRPC strip	96
Module segmentation in ϕ	48 pads
Module segmentation in z	30(A),38(B),38(C) pads
Readout pad geometry	3.5×2.5 cm^2
Total number of MRPC strips	1638
Total number of readout pads	157 248
Detector gas: $C_2H_2F_4$,i-C_4F_{10},SF_6	90%, 5%, 5%
Gas volume	16m^3
Total flow rate	2.7 m^{3}h^{-1}
Working pressure	<3 mbar
Fresh gas flow rate	0.027 m^{3}h^{-1}
Number of readout channels	157 248
Number of front-end analogue chips (8-ch)	19 656
Number of front-end boards	6552
Number of HPTDC chips (8-ch, 24.4 ps bin width)	19 656
Number of HPTDC readout boards (TRM)	684
Number of readout boards (DRM) and crates	72
Occupancy for $dN_{ch}/d\eta = 8000$, B = 0.4 -0.2 T	13% - 16%
Occupancy for pp	6×10^{-4}
π, K identification (with contamination <10%)	0.2-2.5 GeV c^{-1}
p identification (with contamination <10%)	0.4-4.5 GeV c-1
e identification in pp (with contamination <10%)	0.1-0.5 GeV c^{-1}
Event size for $dN_{ch}/d\eta = 8000$	100 kB
Event size for pp	<1 kB

Table 2.2: overview of TOF parameters (A, B, C are central, intermediate and external modules)

rate capability[4]. The time resolution improves with decreasing gap size.

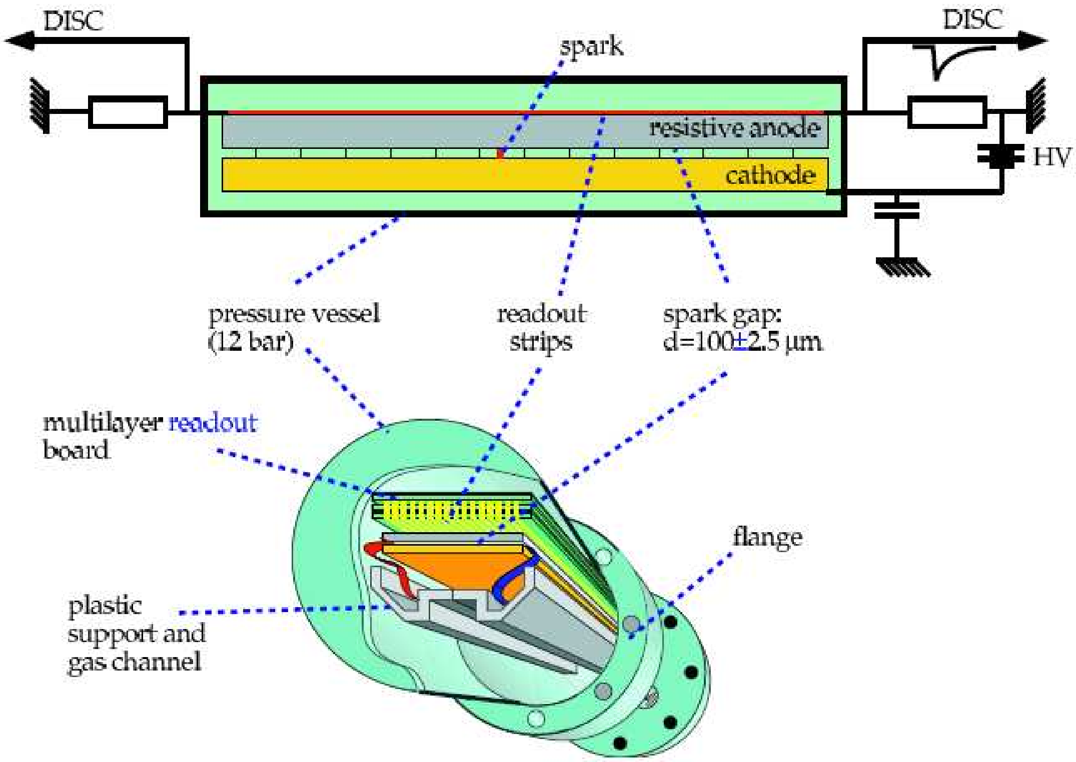

Figure 2.8: a) layout of the Pestov spark counter, with a schematic view of electrodes, 100μm spark gap, the pressurized gas and the indication of the readout scheme via lines

The counter operates at a pressure of $\sim$ 12 bar, which yields 4-5 primary electrons from a minimum ionizing particle. A voltage of up to 6 kV is applied to the electrodes. The spark, initiated in the gap after the crossing of a charged particle, discharges only over a limited area of the semi-conductive anode ($\sim$ l-2 mm^2), while the remaining area of the anode remains sensitive to other charged particles[70].

[4]the first version of the detector had conductive electrodes; in this kind of counter, a dead time of more than 1 ms (needed to remove ions from the gap) limited the counting rate

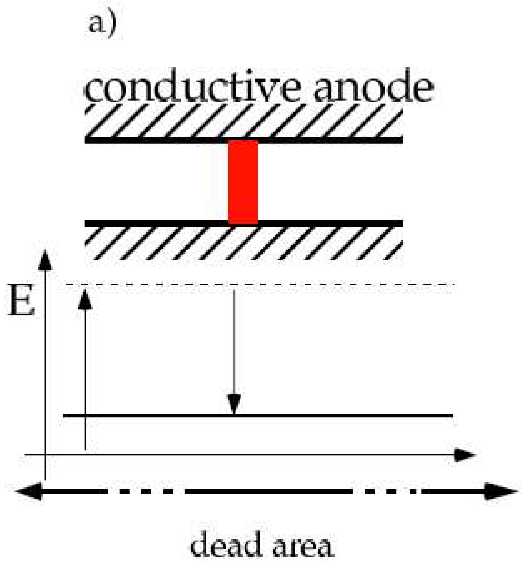

Figure 2.9: a) spark and associated breakdown of the electric field and the corresponding dead area for a normal conducting anode; b) same for spark gap with a semiconductor anode

In figure 2.8 a layout of Pestov spark counter is showed, while in figure 2.9 it is possible to see the two different performances of the counter, with conductive (a) and resistive (b) anode.

Parallel Plate Chamber (PPC)

A Parallel Plate Chamber (PPC) is a single-gap gaseous detector operated in avalanche mode. It consists normally of two planar electrodes made of metal, or metallized ceramic or plastic, kept apart at a fixed distance of 0.5-2 mm using precise spacers, with 5-10 μm accuracy. The inner surfaces of the electrodes are carefully polished so that the electric field produced will have excellent uniformity. The electrode sizes range from 10 $\times$ 10 mm^2 to 100 $\times$ 100 mm^2 or even larger; the total detector thickness is usually a few millimeters, depending on the design and the materials. The high electric field of 2-6 kV/mm between the electrodes allows the immediate Townsend avalanche amplification of the primary ionization, at any point within the sensitive volume. The motion of the electrons in the avalanche induces a very fast signal (rise time less than 1 ns) on the electrodes. This fast signal is followed by a slow signal that lasts for several microseconds, which corresponds to the motion of positive ions. Depending on the gas filling, a gain of 10^3-10^4 can be reached with a very low spark probability. The advantages of the PPC technique include a very fast response and a high rate capability of 10^7 Hz/cm^2 . Thanks to these features, PPCs were widely studied for LHC applications at CERN during the early 1990s, particularly for the very forward muon calorimetry and the forward muon trigger. The use of PPCs as efficient detectors for MIPs (with the added possibility of high resolution timing) was not under investigation for two main reasons:

1. the PPC signals are small, about 1-10 fC. The amplitude spectrum in case of pure avalanche amplification has a hyperbolic-shape with maximum of events being close to zero. This made detection of MIPs rather inefficient; typically, with a gas mixture containing CO_2, i-C_4H_{10} and CH_4, the maximum efficiency was 50-80%, without any observable plateau. Front-end electronics, needed for accurate timing measurements, are much noisy and thus would further reduce the efficiency.

2. The PPC's basic disadvantage is that sparks occur; this limits the gain and makes the PPC sensitive to a low energy background.

A scheme of a PPC is showed in figure 2.10.

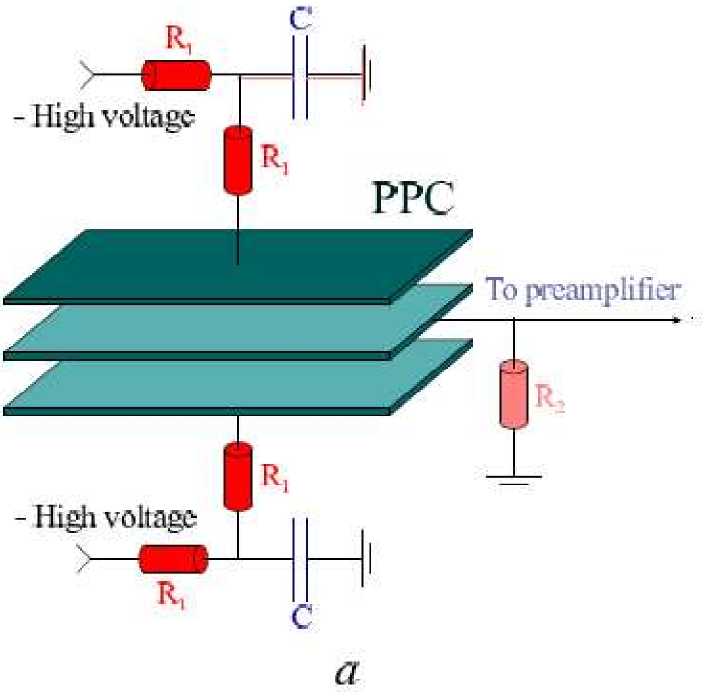

Figure 2.10: scheme of a Parallel Plate Chamber

From the Resistive Plate Chamber (RPC) to the Multigap RPC

The Resistive Plate Chamber (RPC) is a parallel plate chamber with resistive electrodes (rather than the metallic plates used in PPCs). These resistive electrodes quench the streamers so that they do not initiate a spark breakdown. Thus RPCs can be operated at much higher gains in avalanche mode (this is the mode used with PPCs); streamer mode operation is also possible. Resistive plate chambers are well known for their use, for large area coverage, for muon detection. The LAA project at CERN has studied resistive plate chambers, over a few years, with the goal of improving their operation characteristics so they could be used in future hadron colliders. One of the earlier attempts to improve the 2 mm gap resistive plate chamber was to increase the size of the gas gap. This device (known as the “

wide gap RPC") had a gas gap of 6 to 8 mm. It had many advantageous features when compared to the conventional 2 mm gap chamber. One obvious feature was that the gap tolerance was less critical for a wide gap compared with smaller gaps, which resulted in a corresponding easing of problems with the construction. Another advantage of the wide gap was that it allowed the use of a " light" gas (high fraction of Argon). This light gas mixture had a much lower electronegativity compared to the Freon-rich mixtures used in 2 mm gap chambers. The problem with electronegative gases is that there is a much-increased ionic current[5]; this compromises the rate capability. Indeed the wide gap chamber had a rate capability a factor 10 higher than the 2 mm gap RPC. The only disadvantage of the wide gap RPC was a significant worsening of the time resolution. It became clear that, ideally, one wants to keep the advantages of the wide gap (looser mechanical tolerance, improved rate capability) but, at the same time, dramatically improve the time resolution. The route to an improved time resolution is smaller gas gaps. The Multigap Resistive Plate Chamber (MRPC) is a solution that offers both small gas gaps and a large total gas gap. In figure 2.11 it is showed a scheme of a RPC, compared with a MRPC.

It is possible to note (a) a wide gap RPC and (b) a 3-gap multigap design. In both cases the total gas gap is similar ($\sim$ 9 mm), but the multigap is split into 3 sub-gaps of 3 mm each. The intermediate plates are electrically floating and achieve the correct voltage by electrostatic effect. They are kept at the correct voltage by the flow of electrons and positive ions, created by avalanches in the gas gaps. In fact, there is a strong feedback mechanism that forces the gas gain to be equal in all subgaps. There is a further advantage in subdividing the gas gap into many small gaps. A through-going particle produces individual and separate clusters of primary ionisation; each of these clus-

[5] a higher charge produced in the gas gap

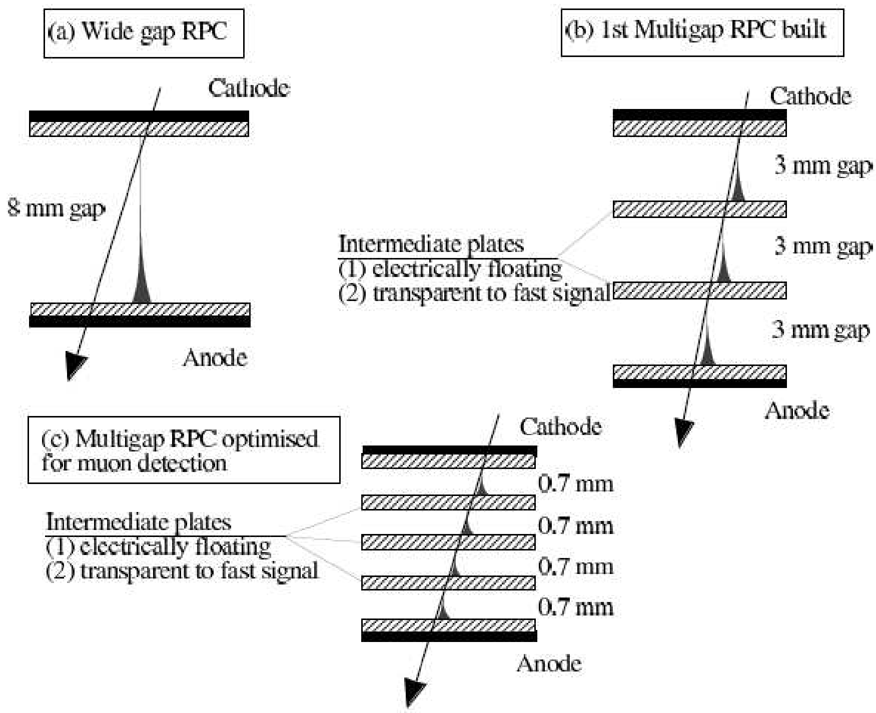

Figure 2.11: scheme of (a) wide gap RPC,(b) first MRPC and (c) MRPC optimised for muon detection

ters will start an avalanche and the final signal will be the sum of all avalanches. These avalanches are not independent and the resultant signal is as if there was only one large " merged" avalanche - instead of the sum of many small discrete avalanches. The conclusion is that inherent fluctuations within the avalanche mechanism dominate for a single gap, while for the multigap the signal is truly the sum of independent avalanches (since the avalanches occur in independent subgaps). The resultant signal thus is the average of many avalanches and has, as a direct consequence, an influence on the shape of the charge spectrum: the single wide gap RPC has a charge spectrum of an exponential shape, while a multigap has a Γ function shaped charge spectrum, similar to a Landau distribution. An exponential-shaped charge spectrum makes life very difficult for detector builders, since one is forced to keep the threshold as low as possible, to avoid a large reduction in efficiency. The charge spectrum from the multigap has a peak well separated from zero, and thus the setting of the threshold is far less critical. This improvement of the shape of charge spectrum further improves the high rate capability of this device. The original LAA-multigap design had 3 gaps of 3 mm. This had a time resolution of $\sigma \sim 2$ ns. After some years of R&D a time resolution < 50 ps has been reached. The cross-section of the final design of an ALICE TOF strip is shown in figure 2.12; this is a 10 gap MRPC, arranged into 2 stacks of 5 gaps, whose size is 250 μm. The High Voltage (HV)is applied by a resistive layer on the outer layers with a resistivity of 5 MΩ/square.

In summary, the multigap RPC allows the simultaneous read-out of many gaps; each gap is separated from its from its neighbour by a sheet of resistive material. These sheets, since they are highly resistive, are transparent to the fast signals generated by the avalanche. There are no electrical connections made to these sheets; they are electrically floating - however there is a strong feedback mechanism where the stable state is equal gain in all sub-gaps.

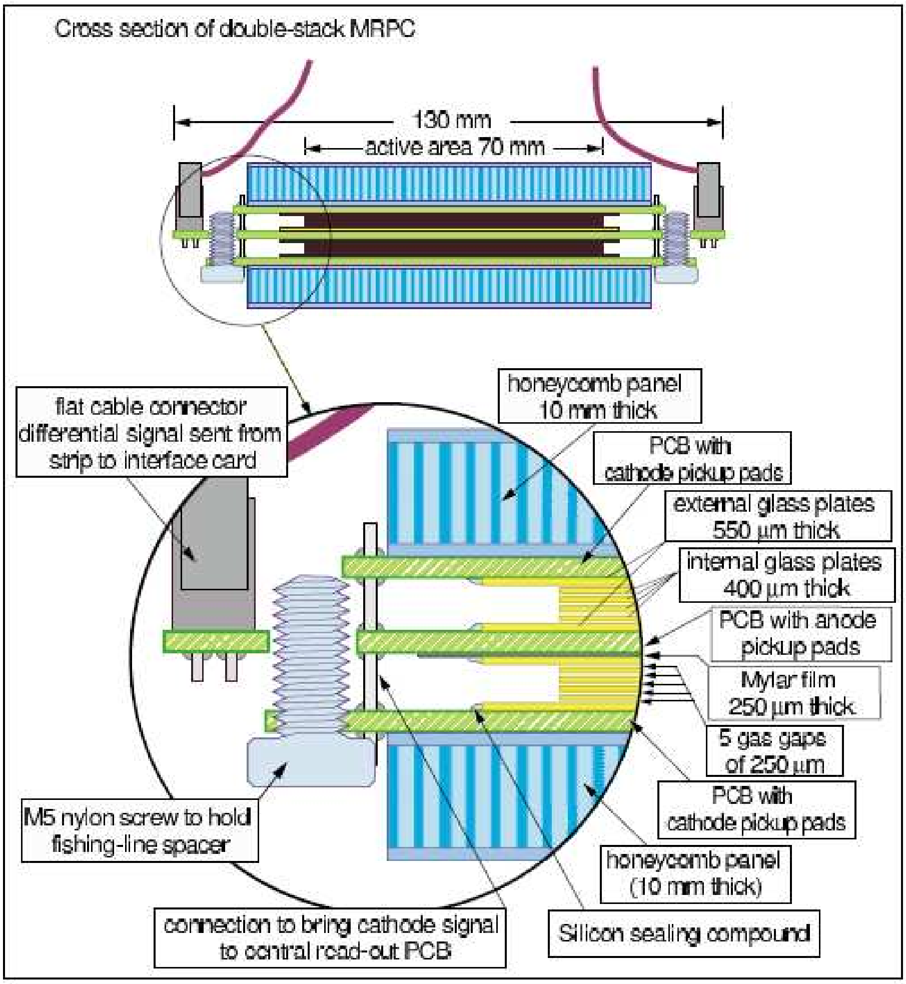

Figure 2.12: cross section of ALICE TOF MRPC strip

Chapter 3

Configuration of MRPC for the Time Of Flight

Charged particle identification is a key tool to study heavy-ion collisions at high energy. The ALICE experiment will take data at LHC, where Pb ions will collide with an energy of 5.5 TeV per nucleon pair, producing several thousands of particles per unit of rapidity. ALICE will use several techniques for identifying charged particles, including a Time-of-Flight (TOF) detector. The 3σ separation of kaons from pions up to 2.5 GeV/c or protons from kaons up to 4 GeV/c requires a global time resolution 100 ps, while a high segmentation is required to match the high multiplicity that characterizes heavy-ion collisions at these energies. The TOF chooses as detector the Multigap Resistive Plate Chamber (MRPC), offering an excellent time resolution combined with a high efficiency. The particular configuration of double stack with ten gaps has been chosen; moreover, an elaborate front-end and read-out electronics has been developed.

3.1 Multigap RPC

RPCs have good performances, but some improvements have leaded to MRPC, because of necessity:

- to increase the limit of the rate capability (from 10 Hz/cm^2 to 500 Hz/cm^2)
- to improve the time resoultion (to 1 ns of RPC till 40 ps of the current chambers)
- to increase the gain, but at the same time, to quench the avalanches
- to reduce the current between the electrodes

3.1.1 Geometry of MRPC

In fig 3.1 a scheme of MRPC with 5 gaps is shown; it's also shown the voltage distribution on the resistive plates. Electrodes are connected to the outer surfaces of the stack of resistive plates while all the internal plates are left electrically floating. There are two features of the MRPC which are important to note:

a) the internal plates take the correct voltage initially by electrostatics and are kept at the correct voltage due to the flow of electrons and ions generated in the avalanche process;

b) even though there are many gaps, there is a single anode and cathode read-out electrode. Avalanches in any of the gaps induce the signals on these electrodes.

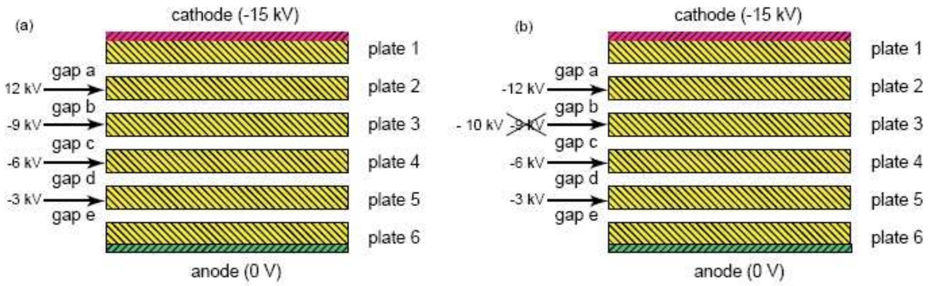

Figure 3.1: a) scheme of MRPC with 5 gaps and voltage distribution; b) rearrangement of the voltage

It is often questioned whether the electrically-floating internal sheets of glass will remain at the correct voltage. In an ideal case shown schematically in fig 3.1a, the voltage across each gap is the same. Since each gap has the same width, on average each will produce the same number of avalanches from the through-going flux of charged particles. This implies that the flow of electrons and ions into the resistive plates bounding a particular gas gap will be the same for all gaps.

Each intermediate plate will receive a flow of electrons (and negative ions) into one surface balanced by a flow of positive ions into the opposite surface. Thus the net charge to an individual intermediate plate is zero; this is a stable state. However, let us now consider the case where one of the intermediate plates has an " incorrect" voltage (as shown schematically in fig 3.1 where the voltage on plate 3 has shifted from -9 kV to -10 kV). Using the labelling shown in the figure, this shift of voltage decreases the field in gap b and increases the field in gap c. Thus the flow of electrons from gap b into plate 3 will be reduced, and the flow of positive ions from gap c will be increased; i.e. there will be a net flow of positive charge that will make the voltage on plate 3 more positive. This is just what is needed, thus one finds that the voltages are automatically adjusted to give equal gain in all gaps.

In fig 2.12 of previous chapter it is showed the cross section of a MRPC. This is a 10 gap MRPC, arranged into 2 stacks of 5 gaps. The gap size is 250 μm; this gap is created by nylon fishing line that runs across the width of the glass plate. This fishing line crosses the stack every 2.5 cm and is aligned such that the fishing line is in exactly the same position in all gaps. The internal resistive sheets are 400 μm thick glass sheets, while the outer plates of each stack are 550 μm thick glass. All the glass is " soda-lime" float glass. The high voltage is applied by a resistive layer on the outer layers with a resistivity of 5 MΩ/square. This resistive layer is acrylic paint loaded with metal oxides.

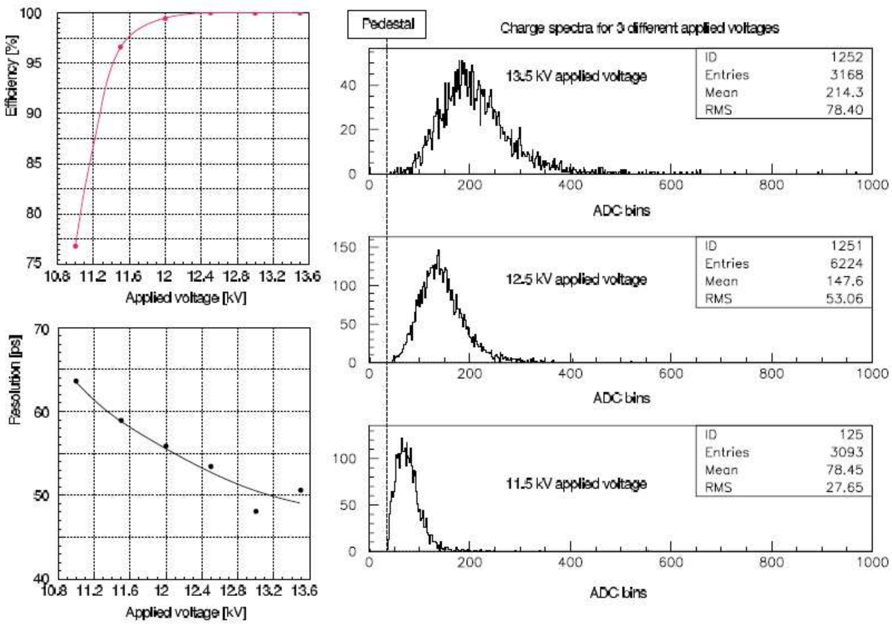

Figure 3.2: performance of ALICE TOF strip; the efficiency and time resolution versus applied voltage are shown on the left-hand side; charge spectra for three applied high voltages are shown on the right-hand side

The reason for the 10 gaps is to increase the efficiency and to enhance the shape of the charge spectrum. In fig 3.2 we show the performance of a typical strip. The efficiency has a plateau of 99.98 %, which is remarkable since the path length of the through-going charged particle through the gas is only 2.5 mm.

3.1.2 Charge Spectrum

As we can see in the previous chapter, if the number of electrons in an avalanche exceed 10^8 (Raether limit) a *streamer* could start; so, for a RPC that works in avalanche mode, the electric field is such as the gain ($\sim$ e$^{\alpha d}$) does not exceed 10^8. The greatest value for αd is $\sim$ 18 and the ratio between fast signal and total signal is 1/αd $\sim$ 5%. The fast signal is processed by the *front-end* electronics in order to generate a *hit*, but the rate capability of the RPC is affected by the total charge that crosses the resistive plates. So the total charge produced in a gas gap has to be minimized in order to allow the use at high rates. Let's consider a RPC with a 2 mm gas gap; a charged particle that crosses the gas volume has to produce a ionization *cluster* in a point rather close to the cathode, in order to produce a signal that can be detected; for this reason a heavy gas has to be used to have a high efficiency. Heavy hydrocarbons cannot be used because they are flammable and so gas like freon are used. Beacause of its electronegativity, the α coefficient is modified; infact, we have to consider not only the Townsend coefficient α, but also the attachment coefficient η and so we have α_{eff}=α-η. For a RPC with a 2 mm gas gap working in avalanche mode, and with αd $\sim$ 18 and $\alpha = 10$ mm^{-1}, the electric field is 47 kV/cm. If the applied voltage fluctuates $\pm$1%, the gain increases from 10^8

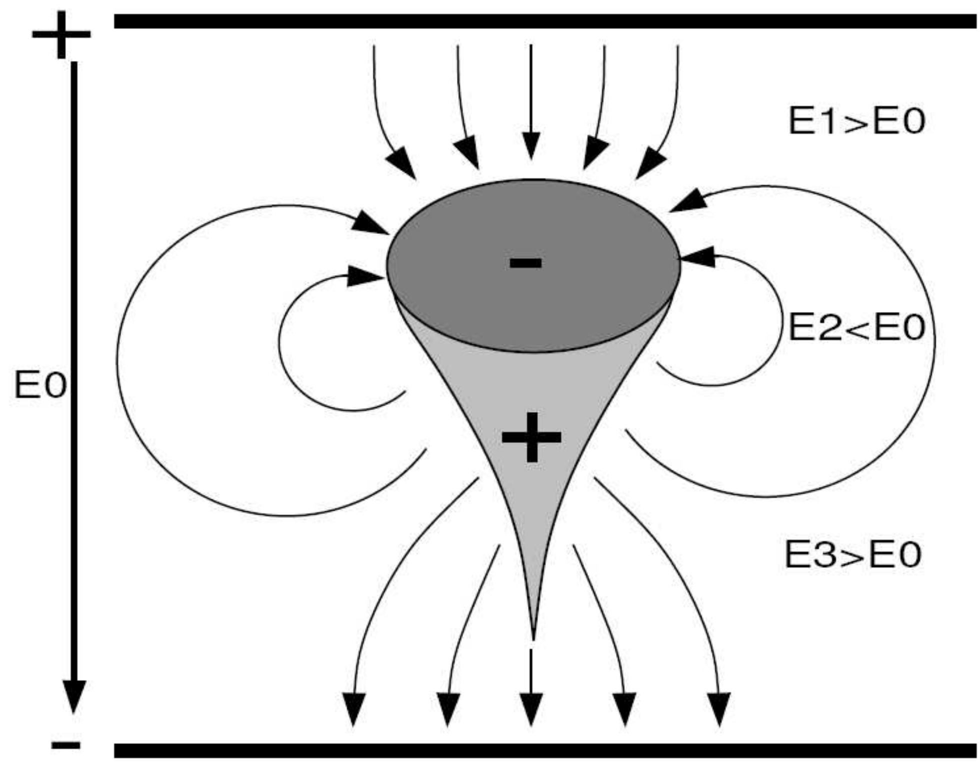

Figure 3.3: scheme of the effect of the charges inside the avalanche on the electric field of a MRPC

to 2×10^9 (20 times higher). In a MRPC, the efficiency plateau starts at electric field $\sim$ 96 kV/cm and the respective value for Townsend coefficient is $\alpha = 127.6$ mm^{-1}, for a gas mixture with 90% of $C_2F_4H_2$, 5% of isobutan and 5% of SF_6. So, if a single electron that crosses through a 250 μm gas gap, an avalanche with 7×10^3 electrons is produced. This value is really over the 10^8 limit, but the detector still works in avalanche mode. To consider the effect of the positive ions on the charge spectrum is very important to understand this phenomenon. In fig 3.3 the electric field of the charges inside the avalanche affects the applied electric field E_0.

The electric field E_2 seen from a charge inside the avalanche is reduced because of the presence of positive ions, while E_1 on the top of the avalanche and E_3 on the bottom increase. A lower

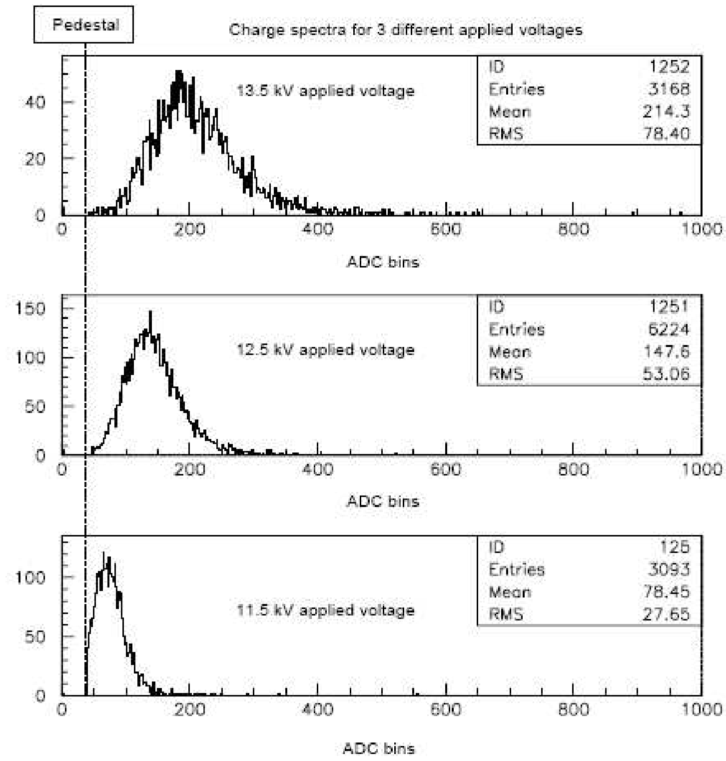

Figure 3.4: total charge produced in the gap versus the applied voltage

value of the electric field implies a smaller effective Townsend coefficient and so a smaller gas gain. Therefore the most of the electrons are in a region of the gas gap where the electric field is lower. This effect is due to the positive ions: they remain in the gas gap longer than electrons, because of their slower drift velocity towards the cathode. The effect is also due to electrons, that reach the anode and accumulate on it, lowering the electric field. This saturation effect reduces the total charge in the gap and explains an important point: the total charge in a MRPC with ten 250 μm gaps is some pC and it grows with applied voltage as showed in fig 3.4[1].

This implies a better rate capability for the MRPC, infact it

[1]for bigger values of the electric field, we observe the production of a *steamer*

can work at rate 1 kHz/cm^2, without worsening performances[2].

3.2 Electronics

As said before, the time resolution required for the ALICE TOF system has to be less than 100 ps. The choices made for the *front-end* and the *read-out* electronics is very important, in order to satisfy this requirement and the need to manage 157248 channels in the 18 sectors.

3.2.1 Front-End Electronics

A simulation of the induced signals on the pick up pads of the strips has shown that it is possible to minimize the edge-effects by using a differential amplifier. The front-end cards are based on this kind of amplifier. Initially a planar device reading out anode pads on one side with the return path to the cathode pads through the metallic box of the detector was developed. This scheme introduced extra noise that caused degradation of the time resolution [71]. Early on in our development we found that the MAXIM 3760, a transimpedance preamplifier for 622 Mbps ATM applications, operated well as a front-end amplifier. This was coupled to an ECL discriminator (MAXIM 9691). An analogue signal was derived from this circuit, the charge of which was measured by an ADC and used for off-line slewing correction. However, for ALICE the time of hits in the TOF array will be digitised with an ASIC known as the HPTDC [72], with 25 ps bins and that can measure both the leading and trailing

[2]the maximum expected rate for the TOF system of ALICE (at 3.7 m from the interaction point) is 50 Hz/cm^2

edge of the input signal. Thus, the front-end electronics should encode the charge of the input signal into the width of the output signal (TOT, Time-Over-Threshold). One obvious problem of the MAXIM solution is the power used, 300 mW per channel. In addition, these amplifiers and discriminators come in discrete packages and thus the front-end card has to be relatively large. The R&D leaded to the final configuration of the front-end cards; the NINO ASIC had to satisfy the following requirements:

a) optimised to operate with 30 pF input capacitance

b) output pulse width dependent on the charge of the input signal (need not be a linear dependence)

c) fast amplifier to minimize time jitter, i.e. first stage with a peaking time of 1 ns

d) threshold of discriminator adjustable in the range 10-100 fC

e) as much as possible compact; the better configuration in this sense is eight channels per ASIC.

Moreover, the R&D had lead to a differential input in order to avoid the noise and to a Low Voltage Differential Signal (LVDS) for the output; LVDS is a differential signaling system with a common-mode voltage of about 1.25 V; the transmitter injects a small current, nominally 3.5 mA, into one wire or the other, depending on the logic level to be sent. The current passes through a resistor of about 100 Ω at the receiving end and the voltage difference across the resistor is therefore about 350 mV. The small amplitude of the signal and the tight electric and magnetic field coupling between the two wires reduces the amount of radiated electromagnetic noise. One of the most important advantages of LVDS is the possibility to transmit fast signals without signal shape distortions, on cables till 4-5 m long (that is the case of our transmission line).

The detector is connected to the input of the NINO ASIC with a short transmission line; thus the input impedance has to match the transmission line and an open loop current to voltage conversion (no feedback) has to be used. The circuit as shown in fig 3.5 satisfies these requirements. The input current pulse is fed into the source of the NMOS (M1) transistor, emerges from the drain and is again fed into the source of the second NMOS (M2) transistor. The current pulse will then emerge from the drain of M2, but the impedance at this point is very different (much larger) than at the input. This current charges the capacitance (which is the unavoidable stray capacitance associated with the transistor) on the drain; the rise time of this signal is governed by the characteristics of the transistor itself while the fall time is given by the time the capacitance C takes to be recharged (i.e. RC).

The input impedance is $(1/g_m)_{M1}$ and therefore the biasing and geometry of M1 is chosen to keep this impedance low to match the transmission line carrying the input signal. The output voltage is defined by the parasitic capacitance C and thus M2 is designed to minimize this capacitance. A block diagram of the NINO is shown in fig 3.6.

The input stage is followed by four stages of low-gain, high-bandwidth differential amplifier. A slow feedback circuit supplies current to ensure that the input stages remain correctly biased. In addition an offset is added at this point that acts as a threshold adjustment. There is a stretcher just before the LVDS output driver. The pulse width before stretching varies between 2 ns and 7 ns; the HPTDC [72] that will be used in ALICE can

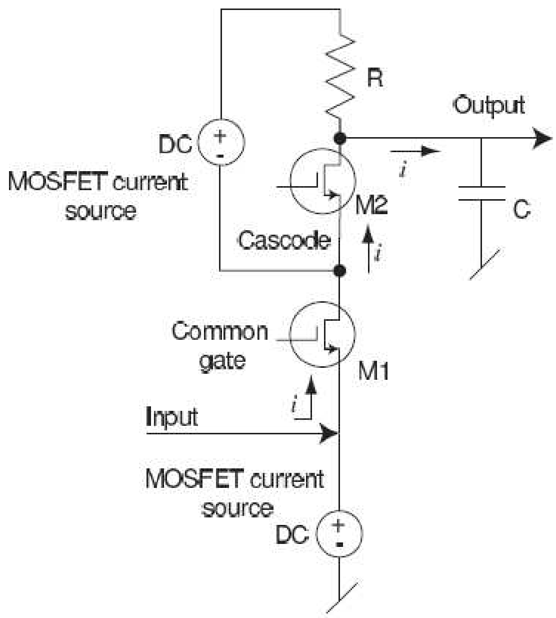

Figure 3.5: schematic input stage of the NINO ASIC

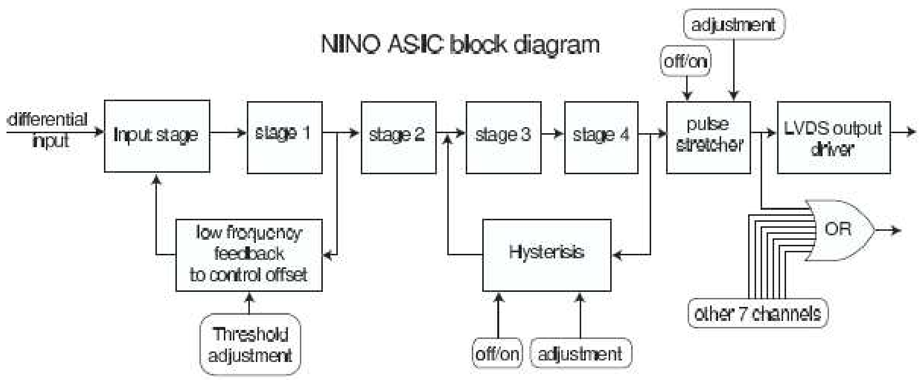

Figure 3.6: block diagram of the NINO ASIC

only measure both leading and trailing edges of an input pulse for widths greater than 6 ns; thus the pulse stretcher will increase the pulse width by 10 ns. The performance of the NINO ASIC attached to the MRPC strip was tested at the CERN T10 beam using 6 GeV/c pions. The time t0 of the incoming pion was measured by two scintillator bars read out with four

Hammamatsu photomultipliers. The time jitter of t0 was 30 ps and was subtracted in quadrature from the measurements of the time resolution of the device under test. The output of the MAXIM FEA card was ECL pulse for the leading edge and an analogue signal that was measured with a CAMAC ADC (LRS 2249W). The time of the leading edge has to be corrected for the amplitude of the signal. Thus, this correction was made using the ADC value in the case of the MAXIM FEA and using the time width for the NINO FEA. The time width of the output pulse from the NINO ASIC varies rapidly for small pulses and has a smaller variation for larger signals. This is shown in fig 3.7. Since time slewing is more evident for signals close to the threshold, this non-linear behaviour is a desired effect. We show in fig 3.8 the distributions of the measured charge. The left-hand plots are for the MAXIM 3760 circuit coupled to an ADC while the right-hand plots are the time-over-threshold (TOT) measurement made for the NINO ASIC. Note that the dynamic range increases for small input charge for the NINO ASIC TOT measurement.

In fig 3.9 it is showed a scatter plot of the time of the hit versus ADC value (for the MAXIM 3760 case) and versus TOT for the NINO ASIC. This is shown for 10.5 kV applied voltage. In fig 3.10 the efficiency and time resolution are showed. Both measurements were done with 60 fC threshold (measured using a pulser). The increased sensitivity exhibited by the NINO ASIC is most probably due to the differential input. Thus, with the NINO ASIC the MRPC strips can be operated at 500 V lower applied voltage; this makes the streamer-free range of the efficiency plateau even larger. So, there are important advantages of the NINO ASIC compared to our baseline solution, a circuit based on the MAXIM 3760. The power consumption is a factor 10 lower (40 mW/channel). The output pulse, after time stretching, matches the width requirements of the HPTDC

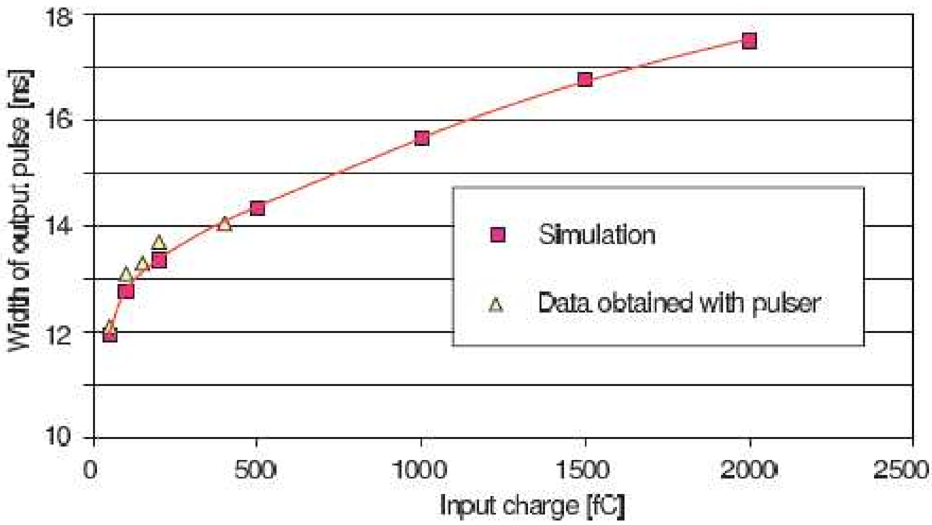

Figure 3.7: width of output pulse as a function of input charge; the expected behaviour from the simulation of the NINO ASIC is also shown

foreseen for the readout. Thus, the signal charge is measured by TOT (the time of the leading and trailing edge of the pulse).

The circuit has differential input and is differential throughout. This leads to increased sensitivity and increased immunity to cross-talk.

3.2.2 Read-Out Electronics

A compact data acquisition and power supply system housed in a water cooled special crate has been designed for the readout of the TOF (Time Of Flight) detector of the Alice experiment at CERN. The Crate called Alice-TOF-box contains a 12 slot VME64X bus that houses 2400 multi-hit 25ps TDC channels (TDC Readout Module: TRM), a local Trigger Module (LTM), a Clock Distribution Module (CPDM) and a Data Readout Module (DRM board) with two optical links and Ethernet. The same crate hosts branch controlled power supply modules

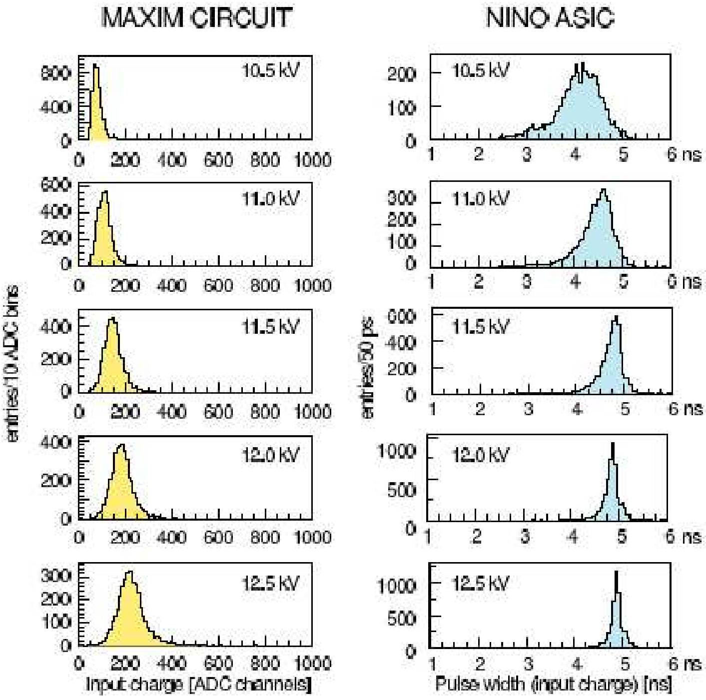

Figure 3.8: distributions of the signal charge: the left-hand spectra are obtained with the MAXIM 3760 circuit coupled to an ADC; the right-hand spectra show the TOT produced by the NINO ASIC

for the VME boards and the TOF detector front-end modules. The whole system shall be used close to the TOF detector and will work under moderate radiation and intense magnetic field (1.2 Gy/10 years TID, 5 KGauss). The TDC boards house TDC chips developed by CERN/ECP-MIC Division (HPTDC).

TDC Read-Out Module

A logic block scheme of the TRM is shown in fig 3.12. The card, a VME slave card (fig 3.13), host 30 HPTDC, organised in two separate 32-bit parallel readout chains. A central FPGA acts as readout controller, event manager and implement also the VME interface (these three functions are separately shown in fig 3.12). To make easier maintenance and to match the

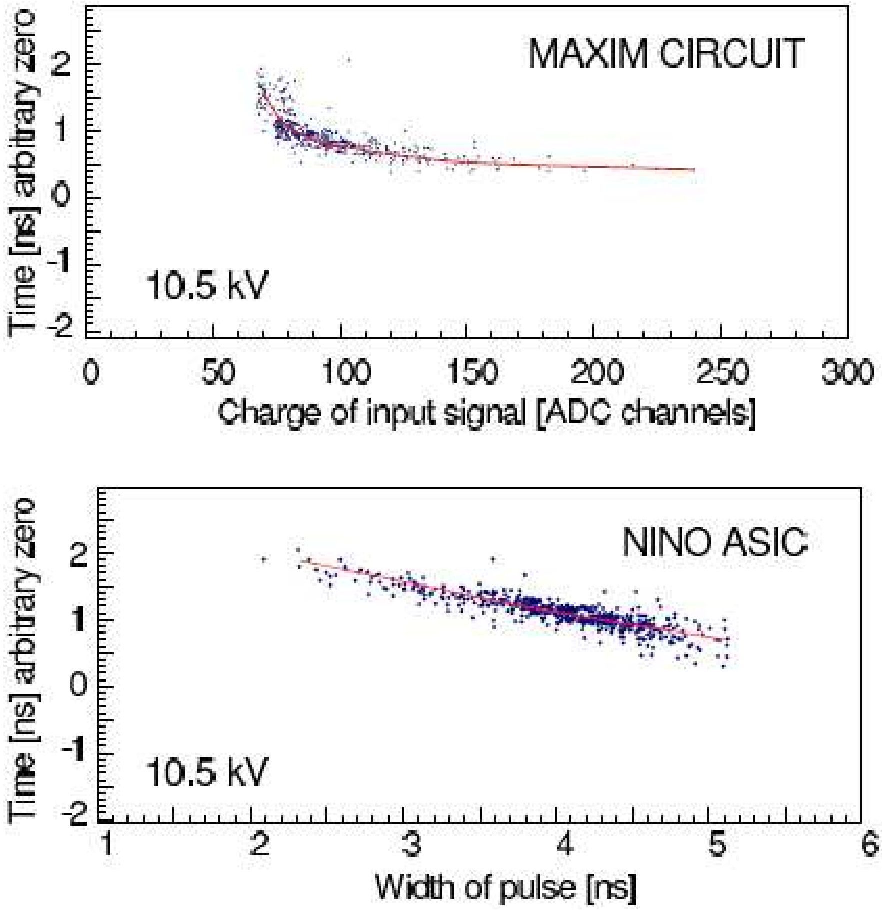

Figure 3.9: scatter plot of measured time versus charge

Front End granularity, the HPTDCs are mounted in 10 piggy-back cards, connected to both sides of a central motherboard. A central aluminium bar will guarantee the needed cooling of HPTDC.

The TOF system will provide readout for 684 TRM cards, housed in 72 custom 12 slots VME crates.

The TRM is based on a High Performance TDC (HPTDC) ASIC [73], developed by CERN/EP Microelectronic group for LHC applications, with multi-hit and multi-event capabilities. The ASIC provides relative time measurement of each hit at

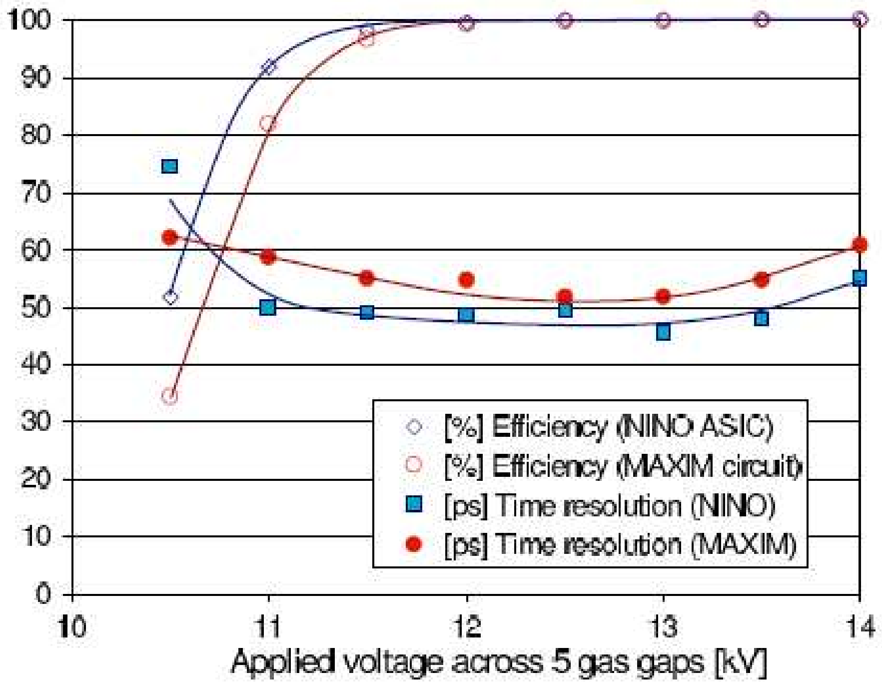

Figure 3.10: efficiency and time resolution using the MAXIM circuit and the NINO ASIC

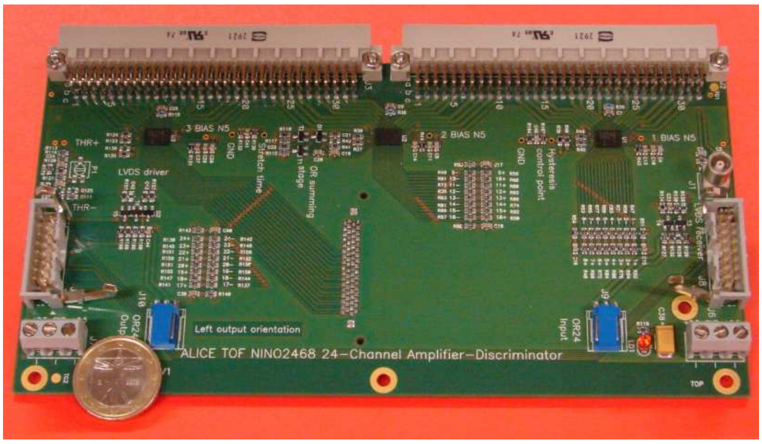

Figure 3.11: picture of the Front End ASIC card (FEA)

external trigger arrival. The time digitization is based on a clock synchronous counter and a DLL interpolator[3]. The external 40

[3]the Delay Locked Loop can be used to change the phase of a clock signal, usually

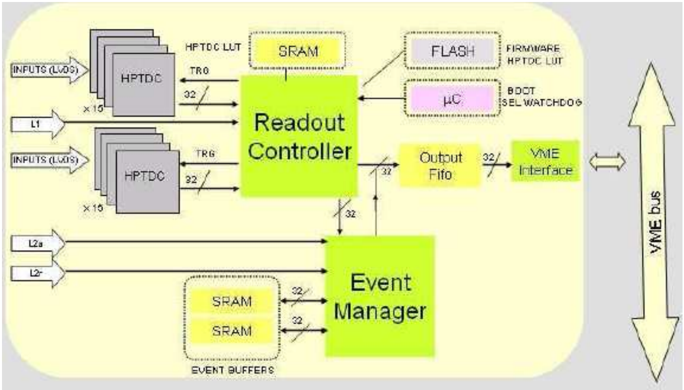

Figure 3.12: TRM logic blocks

Figure 3.13: picture of a TRM

MHz clock is internally multiplied by a PLL[4] to feed properly

to enhance the clock rise-to-data output valid timing characteristics of integrated circuits (such as DRAM devices); DLLs can also be used for clock recovery (CDR). From the outside, a DLL can be seen as a negative-delay gate placed in the clock path of a digital circuit. DLL compares the phase of one of its outputs to the input clock to generate an error signal which is then integrated and fed back as the control to all of the delay elements. The integration allows the error to go to zero while keeping the control signal, and thus the delays, where they need to be for phase lock. Since the control signal directly impacts the phase this is all that is required. The main component of a DLL is a delay chain composed of 32 delay gates connected back-to-back. The input of the chain (and thus of the DLL) is connected to the clock that is to be negatively delayed. A multiplexer is connected to each stage of the delay chain; the selector of this multiplexer is automatically updated by a control circuit to produce the negative delay effect. The output of the DLL is the resulting, negatively delayed clock signal

[4] the Phase Locked Loop is a control system that generates a signal that has a fixed

the DLL to reach the required resolution. The HPTDC has a 647 configuration bits register, plus a 40 control bits register, accessible through its JTAG interface. Digitised hits are stored in four L1 buffers, 256 hits deep and shared by 2 channels each. Matched hits with the external trigger are moved to a readout FIFO, 256 hits deep. The total amount of internal memories is 5.1 kB.

Data Read-out Module

The DRM board (block diagram shown in fig 3.14 provides the VME Master duties in the crate (data readout from TRM boards) and performs other functions, such as data transmission and communication with the Data AcQuisition (DAQ) system of ALICE experiment through Data Detector Link (DDL) [74], reception and computing of trigger signals through Timing Trigger Control receiver (TTCrx) [74], VME bus access through a slow control optical link (Slow Control Link: SCL) and remote programming of FPGA on VME boards in the crate. The DRM performs also data sniffing from DDL link providing useful online informations for detector debug and data quality monitor.

The DRM Slow Control section houses one Linux embedded Single Board Computer [74] (Mod. A1500 with 200MIPS RISC). The DRM Slow Control section can be accessed via Optical Fiber (1.25 GHz Optical link), via Ethernet 10/100 Mbit/sec and via the DDL interface. TTC section houses the TTCrx (Timing, Trigger and Control Receiver ASIC for LHC Detectors). The TTCrx acts as an interface between the Timing Trigger and Control distribution (TTC) system for LHC detectors

relation to the phase of a reference signal. A PLL circuit responds to both the frequency and the phase of the input signals, automatically raising or lowering the frequency of a controlled oscillator until it is matched to the reference in both frequency and phase. A phase-locked loop is an example of a control system using negative feedback; a PLL compares the phase of its oscillator with the incoming signal to generate an error signal which is then integrated twice to create a control signal for the “ voltage-controlled oscillator”

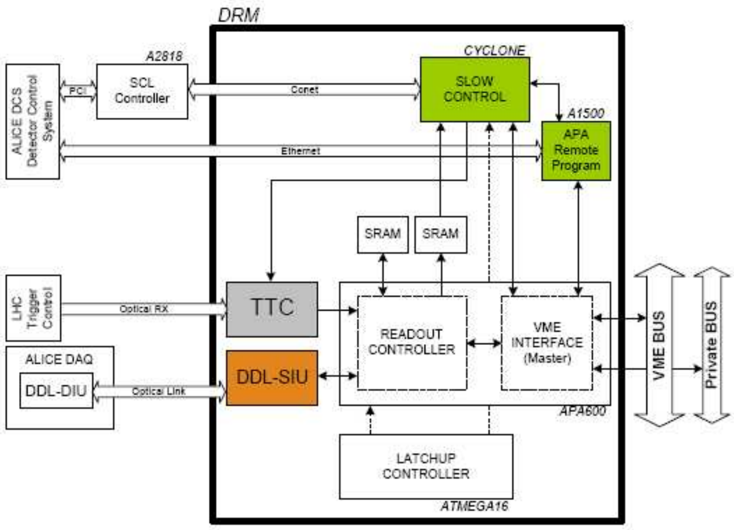

Figure 3.14: DRM board

and its receiving end users.

Figure 3.15: picture of a DRM

The ASIC delivers the clock together with control and synchronisation information to the front-end electronics controllers in the detector. The DDL-SIU section houses, on a piggy back board, the Source Interface Unit developed by the ALICE collaboration in the Detector Data Link framework. The ALICE Detector Data Link (DDL) [74] is a high-speed optical link designed to interface the readout electronics of ALICE detectors to the DAQ computers.

Local Trigger Module and Clock Distribution Module

LTM provides the signal set up for trigger, for the slow control of some detector parameters (low voltages,temperature) and for the production of the threshold voltages of the Front End Cards (FEA). Moreover each LTM provides the logical trigger logic of the FEAC signals which is then sent to the ALICE trigger section. The CPDM board is hosted only in one crate every two. It receives through the unimode optical link the LHC clock signal, translates it into a LVDS level and distributes it to the TRMs, thus providing the 24x fan out function with jitter below 10 ps. Moreover the CPDM provides the 12x fan out of the strobe pulse from the DRM, towards the pads. The CPDM is not handled via VME bus.

Power Supply

The power supply section is developed from the EASY (Embedded Assembly SYstem) modules [74] and is composed by one Mod. A1396 and two Mod. A1395, branch controlled power supply modules. The Mod. A1396 houses a GEneral COntroller device (GECO) and the front end power supply. The Mod. A1396 is connected to a branch controller board (A1676A) housed in a CAEN SY1527 Power Supply System [74], located in the experimental hall, where the magnetic field is about 60 Gauss. Four

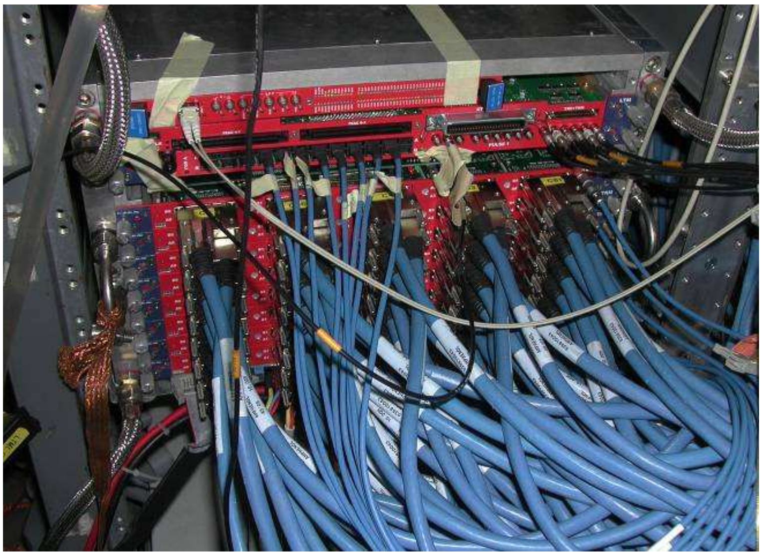

Figure 3.16: picture of a crate, with TRMs, LTM and CPDM inside

SY1527 placed around the detector house two branch controllers A1676A each, connected to 18 crates (one TOF quadrant) via EASY bus. The whole system is supplied by 12 customized 48 V AC/DC converters (Mod. A3485), designed to work in a moderately hostile area and controlled as Low Voltage (LV)channels through a GECO device. The Mod. A1396 provides eleven 2.7V/7A channels and one 5V/2A channel and has two temperature sensors; the Mod. A1395 provides one 3.3V/100A channel and has four temperature sensors.

3.3 Some results from beam tests

In the last years several prototype MRPCs and strips from the mass production have been tested at Cern with a pion/muon beam. In these tests, a lot of features have been studied, in

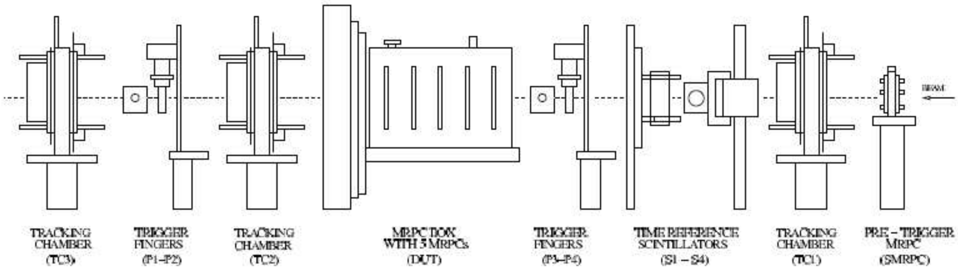

Figure 3.17: schematic layout of the experimental set-up at the T10 beam line

order to find the better configuration for the MRPC strips used in ALICE: the gap size, the gas mixture, the front-end and the read-out electronics and the cables were some of the most important ones. In this work, the tests of 2002 on some prototype strips and the one of 2006 on some strips from the mass production will be briefly described.

3.3.1 Beam Tests in 2002

During autumn 2002, seventeen double-stack MRPCs were tested at the PS-T10 beam line of the CERN Proton Synchrotron. In fig 3.17 the experimental set-up is ilustrated; it consisted of:

- a small MRPC (SMRPC), made of a single stack of glasses defining 5 gaps, each of 230 μm with 10 cm^2 active area, which acts as pre-trigger providing the start to the TDCs (Time To Digital converter) and the gate to the ADCs (Analog to Digital Converter)
- three tracking chambers (TC1, TC2, TC3), each consisting of 2 planes (10 $\times$ 20 cm^2) of strips with 4 mm pitch, to provide information on the position of the beam; the precision of the TCs is about 1 mm in both the coordinates

- two pairs (P1-P2 and P3-P4) of crossed scintillators, whose coincidence defines a 1 cm^2 area and provides the trigger
- two fast scintillator bars ($2\times2\times10$ cm^3), each equipped with two photomultipliers (S1, S2, S3 and S4), discriminated by Constant Fraction Discriminators, to provide an accurate time reference
- the device under test (DUT), i.e. up to 5 MRPC strips, closed in an aluminium box with external dimensions of 19.5 cm $\times$ 48 cm $\times$ 129 cm

The chambers were filled with a gas mixture of 90% $C_2F_4H_2$, 5% $S\ F_6$ and 5% $C_4\ H_{10}$. The measurements have been made using a 7 GeV/c beam of negative particles (π and μ). A mechanical frame was used to move the aluminium box with millimetric accuracy. This allowed to change the position of the beam on different pads by remote control. During these tests particular care was devoted to the study of the uniformity of response of the devices by centering the beam on many different pads, randomly distributed along each MRPC strip. Fig 3.18 shows the efficiency and the time resolution of over 100 pads belonging to the 17 chambers, measured at a fixed high voltage value of 13 kV. The upper histogram shows the distribution of the efficiency values, with a mean of 99.6%, the lower one refers to the distribution of the time resolution values, with a mean of 62.9 ps.

Fig 3.19 shows an example of high voltage scan along one MRPC: the two plots show, respectively, the efficiency and the time resolution as a function of high voltage, for different beam positions along the strip. It should be noted that each curve corresponds to a different read-out pad. In the HV range between 12 and 13 kV, the mean efficiency is 99.9% and the mean time resolution is 50 ps. All the tested MRPCs showed a very good uniformity and a long streamer-free plateau.

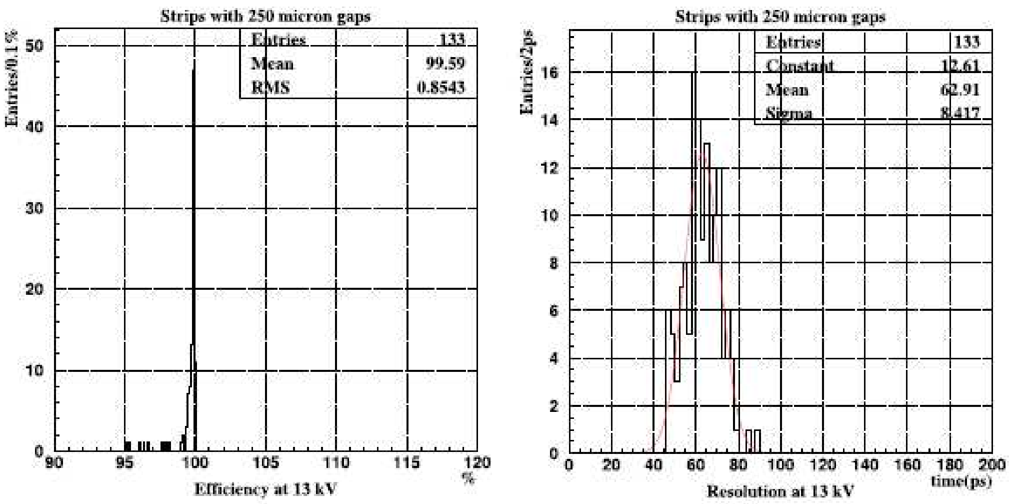

Figure 3.18: efficiency and time resolution distributions for all 17 MRPCs tested in October 2002

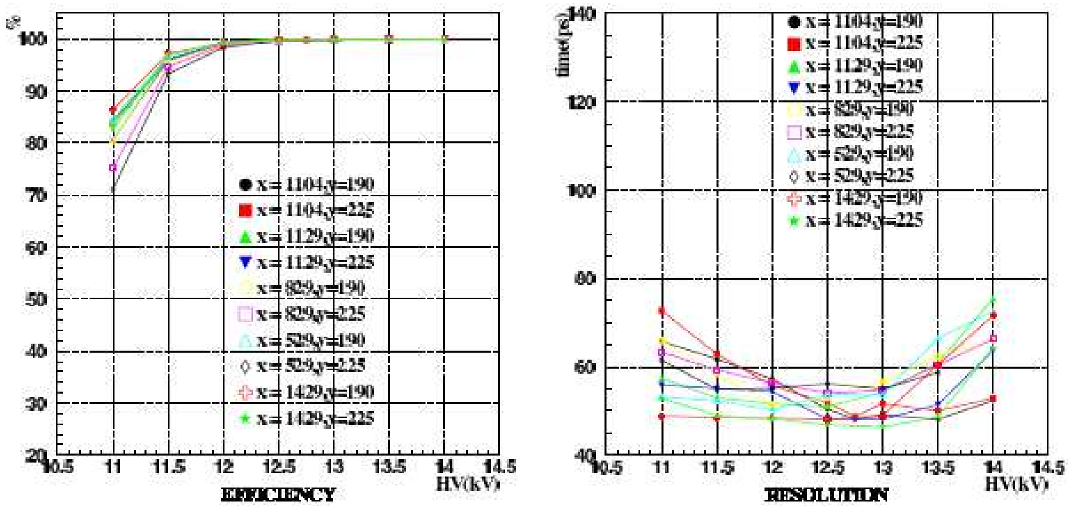

Figure 3.19: example of uniformity study along one MRPC strip in terms of efficiency and time resolution measured in different positions along the strip efficiency and time resolution distributions for all 17 MRPCs tested in October 2002

ALICE experiment will run for many years and the detectors will be irradiated by a very large number of particles. Hence age-

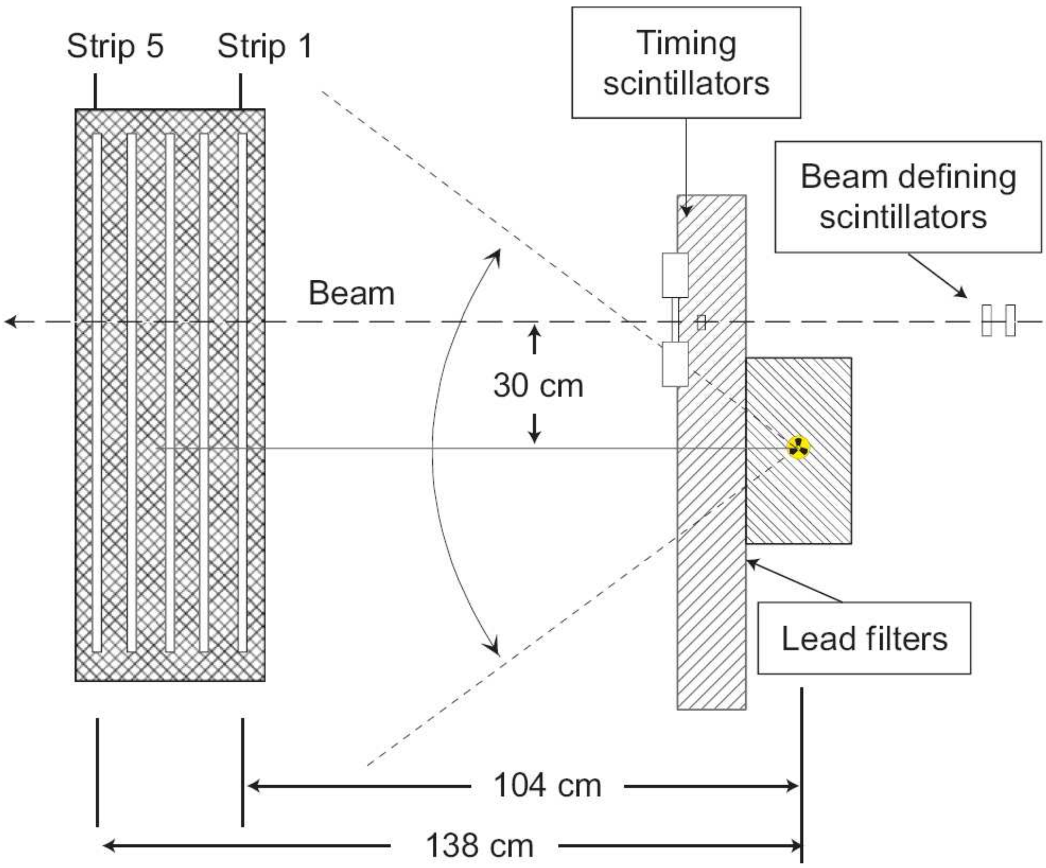

Figure 3.20: example of uniformity study along one MRPC strip in terms of efficiency and time resolution measured in different positions along the strip efficiency and time resolution distributions for all 17 MRPCs tested in October 2002

ing tests were required to study a possible degradation of the behaviour of the MPRCs. Two strips (CH1 and CH2) have beeen irradiated at the CERN Gamma Irradiation Facility (GIF), located in the X5 area of the West Hall. This facility allows a device to be irradiated with 662 keV photons from a 740 GBq ^{137}Cs source [75]. In fig 3.20 the GIF set-up is shown, while in fig 3.21 and 3.22 the efficiency and the time resolution of 5 strips with the irradiation source on and off are presented [75].

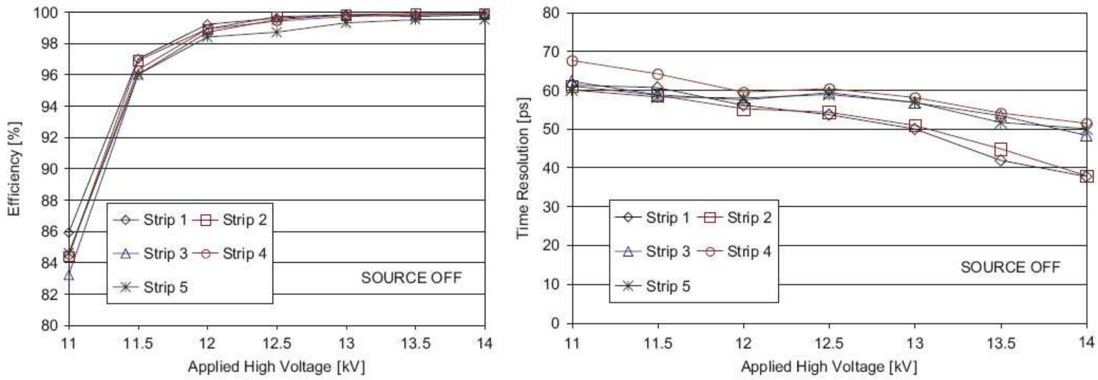

Figure 3.21: efficiency and time resolution measured with the GIF source off

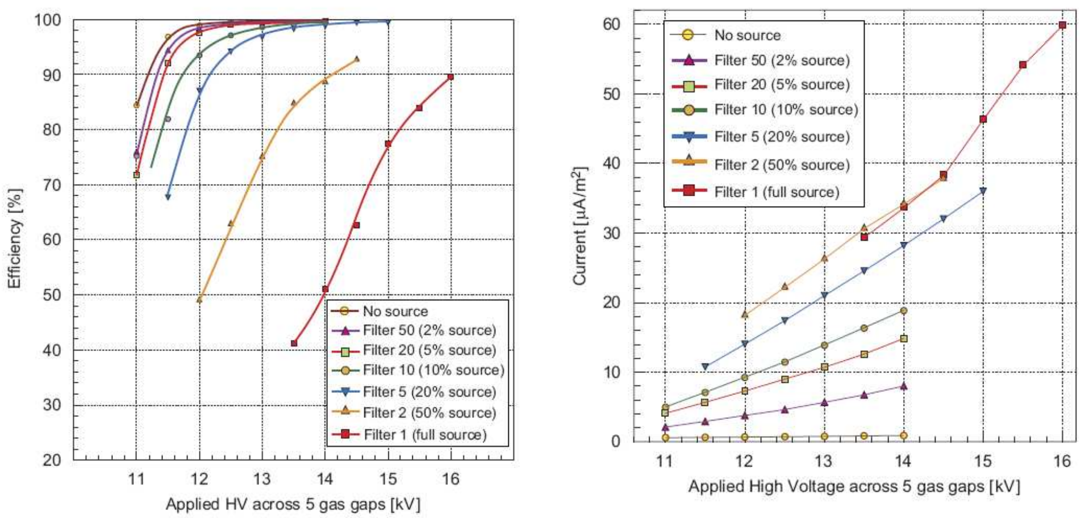

Figure 3.22: efficiency measured with the GIF source on, for one of the 5 strip; the current drawn by this strip versus the applied high voltage is also shown

3.3.2 Beam Tests in 2006

During the last two years the MRPCs mass production was carried out in the INFN TOF laboratories in Bologna. To simplify, automate and speed up the MRPC assembly, a series of procedures were developed. A test of a sample of 10 MRPCs randomly chosen from the 1638 ones of the mass production was carried

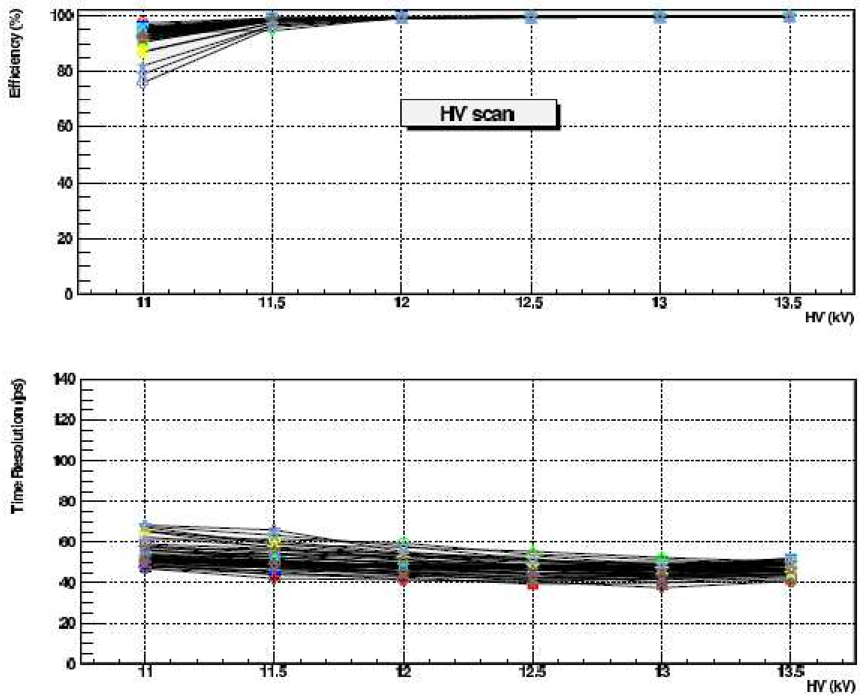

Figure 3.23: efficiency and time resolution as a function of the applied voltage for 55 readout pads randomly distributed on 10 MRPCs

on during the autumn of 2006 using the final electronic chain from the front-end card with the NINO-ASIC to the readout modules with the HPTDCs.

The tests were performed in the experimental area located at the PS-T10 beam line of the CERN Proton Syncrotron. The experimental set-up consisted of:

- two fast scintillator bars ($2 \times 2 \times 10$ cm^3), each equipped with two photomultipliers to provide an accurate time reference
- two pairs of crossed scintillators, whose coincidence defines a 1 cm^2 area and provides the trigger
- a device under test, i.e. an aluminium box (external dimensions of $19.5 \times 48 \times 129$ cm^3) hosting 5 MRPCs.

A mechanical frame was used to move the box with millimetric accuracy. This allowed to position the beam on different readout pads by remote control. The aluminium box was filled with the MRPC standard gas mixture: 90% $C_2\,F_4\,H_2$, 5% $S\,F_6$, 5% $C_4\,H_{10}$.

The uniformity of response of the chambers was studied first by centering the beam on many different readout pads, randomly distributed along each MRPCs. The efficiency and time resolution as a function of the applied voltage for 55 channels belonging to the 10 MRPCs are shown in fig 3.23. It should be noted that in the HV range between 12.0 and 13.5 kV, the mean efficiency is higher than 99% and the mean time resolution is 50 ps. This means a very good uniformity and a long streamer-free plateau. Then a scan over 159 readout pads was performed by fixing the high voltage value to 13.0 kV. The results are plotted in fig 3.24 where the efficiency (on the left) and the time resolution (on the right) are presented. As it can be seen the mean efficiency is 99.6% and the time resolution is about 48 ps. The RMS of the time resolution distribution (4.7 ps) gives an estimate of the uniformity of the devices.

The strip B19, produced and tested at PS in 2004, was tested again in 2006. This MRPC was used as reference in the cosmic ray telescope in Bologna continuosly running since 2 years. As it can be noted, the detector's response was not affected by a so long " ageing" process.

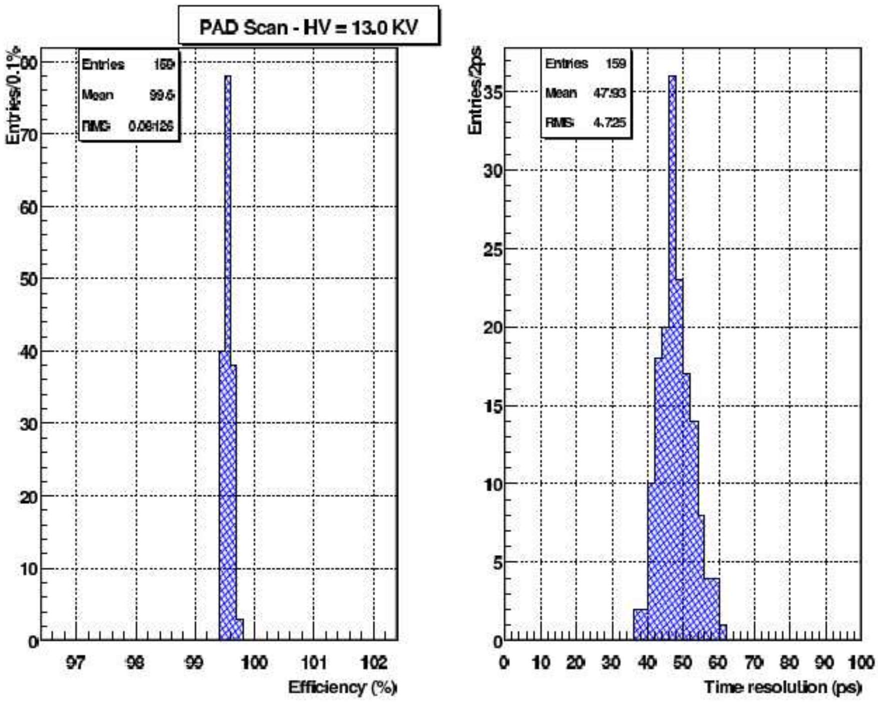

Figure 3.24: efficiency and time resolution distributions for 159 readout pads at a fixed voltage of 13.0 kV

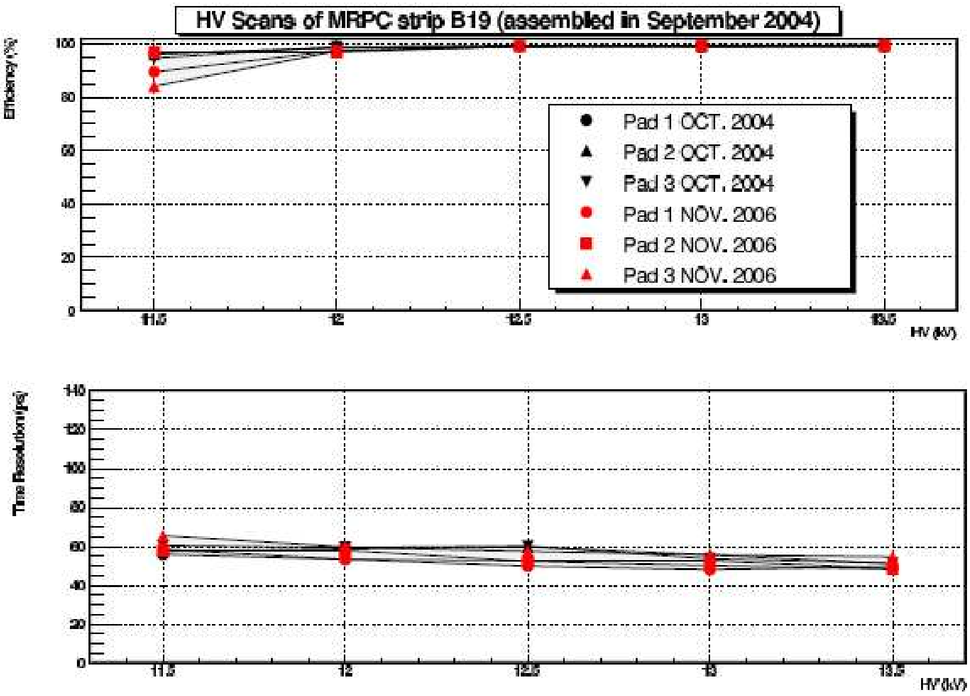

Figure 3.25: efficiency and time resolution for the MRPC B19 used as reference in the cosmic ray telescope in Bologna

Chapter 4

From the Strips to the Supermodules

In this chapter the construction of the MRPC strips, their assembling in the modules and the final assembling of the supermodules are presented; the tests performed on all the components are shown. These tests are performed in order to ensure high quality performances of a system like the Time Of Flight, in LHC collisions environment, where the multiplicity will reach thousands of particles. Very important tests on the mechanical parts and on front-end and readout electronics are performed.

4.1 Construction of a double-stack MRPC

The active area of MRPC used in the TOF of ALICE is 7.4 $\times$ 120 cm^2 (see fig 4.1); the signal pads are 96 per each strip (positioned in two raws along the strip) and their dimension is 3.5 $\times$ 2.5 cm^2. In fig 4.1 the two raws of pads are shown, while in fig 4.2 it is shown the honeycomb panel that has to be glued on the cathode Printed Circuit Board (PCB) and that is responsible of the mechanical rigidity of the strip.

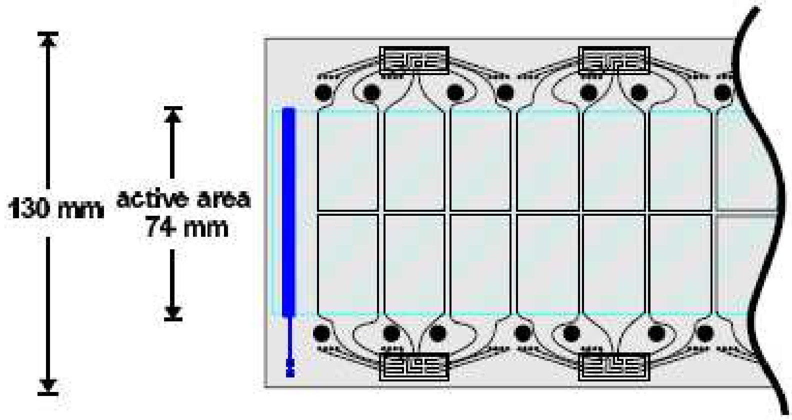

Figure 4.1: pads for the signal catching

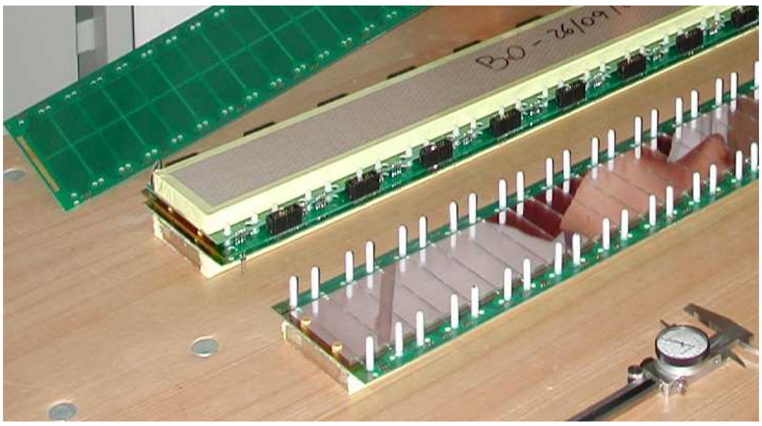

Figure 4.2: honeycomb panel for the rigidity of the strip

In fig 4.1 we can also see the little pins that provide compactness and the transport of the signal from the electrodes to the *front-end* cards, towards 32 connectors soldered on the PCB; we can see a strip after the construction and another one not assembled in fig 4.3.

We can divide the construction of a MRPC in two steps; the first one is devoted to the preparation of all the components

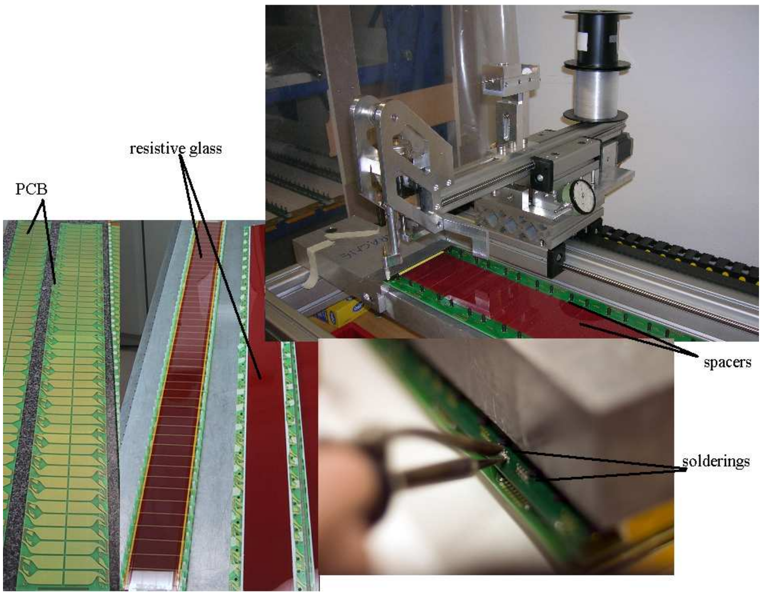

Figure 4.3: strip before and after the construction

and the second one is the assembling of the strip. The first step provides for:

- glueing of a honeycomb panel on the external surface of the two PCB (PCB-bottom and PCB-top) with the 96 signal pads
- insertion in the PCB-bottom of nylon pins, used to hold the *fishing-line* spacer for the cration of 250 μm gaps[1]
- glueing of a mylar film to the central PCB on the pad side, in order to insulate the pads from the high voltage; then two 550 mm glass sheets are fixed on both sides of the central PCB;
- cleaning of external glasses (painted with high resistivity acrylic paint) and removal of possible paint lump from the

[1]some studies have been made to find the better geometry of the fishing-line spacer and the better compromise between detecting efficiency and uniformity of the gap

edges of the glasses[2]

- washing of the internal glasses that make the two qstacks; in fig 4.4 the washing system is showed with the four washing tanks: one ultrasound tank that allows a careful cleaning; than there are two tanks for the cold rinse of the glasses and another one to dry them (at ~ 50 degrees); the facility has a water filtering sytem that allows the use of demineralized water during the entire cycle

- gluing of the acrylic painted glasses on the PCB with a conducting epoxy resin spread on the little copper strips on the edges of the glasses[3]

The second step of the construction of a MRPC strip is the proper assembly of the strip. When the PCB-bottom with its red glas is ready, it is put on the automatic machinery for the fishing-line placing; after the disposition of the first layer, the other glasses are inserted. This is done other four times in order to do the first stack. Then the central PCB[4] is glued on the first stack and the step to build the second stack begins. In the end the PCB-top closes the strip and five lead bricks (50 kg) are placed on the strip to ensure a uniform pressure all along. Final insertion and soldering of pins in each PCB (see solderings in fig 4.3), provide mechanical rigidity and allow, at the same time, to transmit the signals from the external PCBs to the central one. On the central PCB, 32 connectors for flat cables[5], providing signal transmission to the front-end electronic cards, are finally soldered. The high voltage connection is made at both ends of

[2]this is a very important step, in order to avoid streamers between the edges of the two red glasses of the same stack (the distance between them is about 4 mm)

[3]this resin allows a perfect adhesion of the glass on the PCB and a perfect conducting contact; no degradation in a gaseous environment has been found

[4]this PCB has two red glasses glued on the two surfaces

[5]during the beam tests some studies on the signal cables from PCB to front-end cards have been performed

the strip via a trace, on the surface of the PCBs, connected to the painted glass layer with a conductive adhesive.

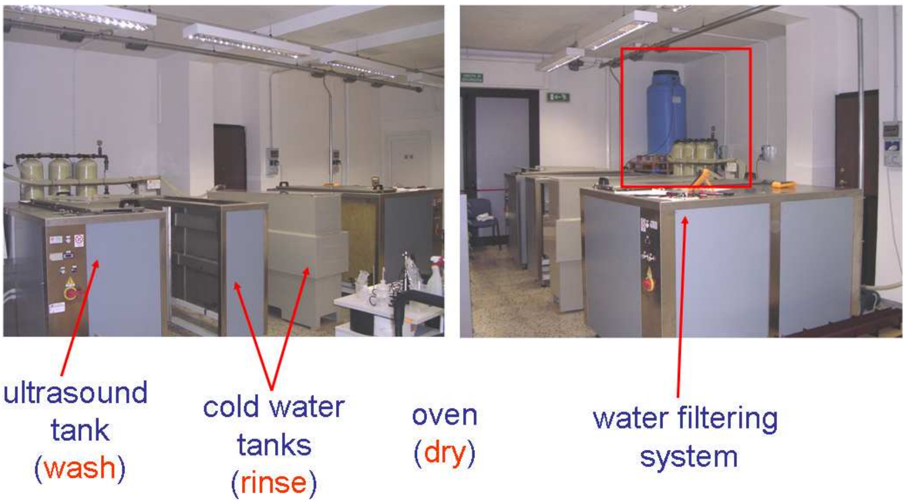

Figure 4.4: the resistive glass characterization system

4.1.1 Tests performed on the strips

A very important point is the uniformity of performances of the strips in all their parts: a test on the resistivity of the glasses and on the gaps size is performed. It is very important also to check the correct behaviour of the HV connections, to avoid the possibility of dark currents in the gaps; finally, the connections of the signal lines are tested. A sample of strips is also tested on the cosmic rays facility of the INFN Bologna Laboratories. Before the assembling of the strips inside the modules, the latter are tested, in order to check their gas tightness and the good status of the HV connections. When the modules are ready, with all the strips inside and all the connections (pulser line, HV and signal cables) completed, other important tests are performed: a new HV test and a pulser test in order to find possible dead channels and eventually to recover them. The overall fraction of rejected chambers is at the percent level.

Gap Width and resistivity

It is very important to ensure the uniformity of the strips; a different width of the gas gaps, in some points of the strip, could change the arrangement of the charge towards the plates, making the performance of the MRPC worse. In fig 4.5 the set up for this test is shown: the strip is placed on a guide structure, hosting a *CCD* camera. A Labview project is used to acquire the image and to measure the luminosity distribution in 8 different position of the strip.

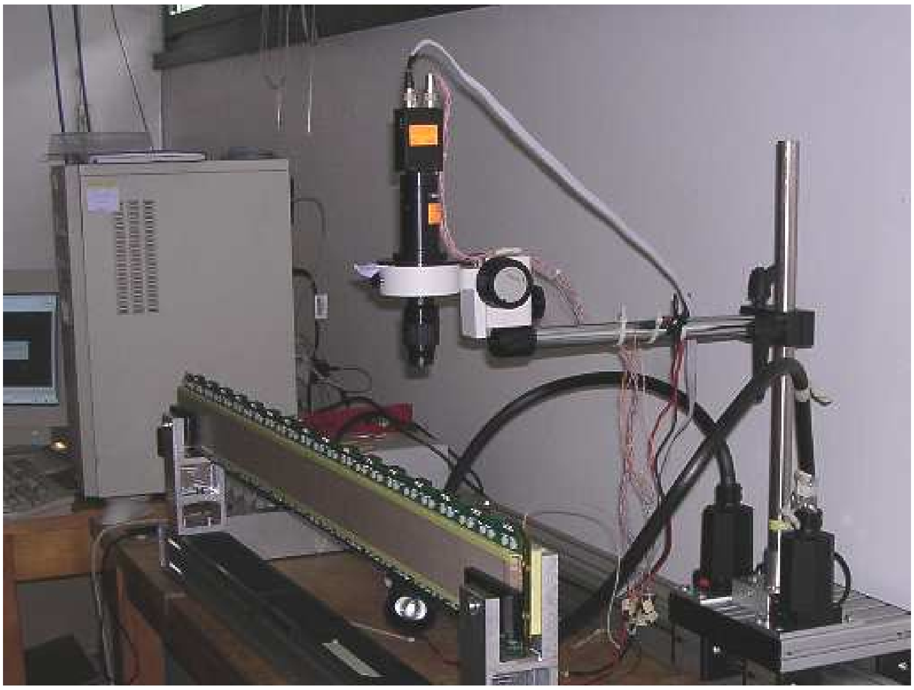

Figure 4.5: set-up of the test on the gas gaps size

The first step is ligthing up a point of the strip and catching the image; the software measures the luminosity of the different

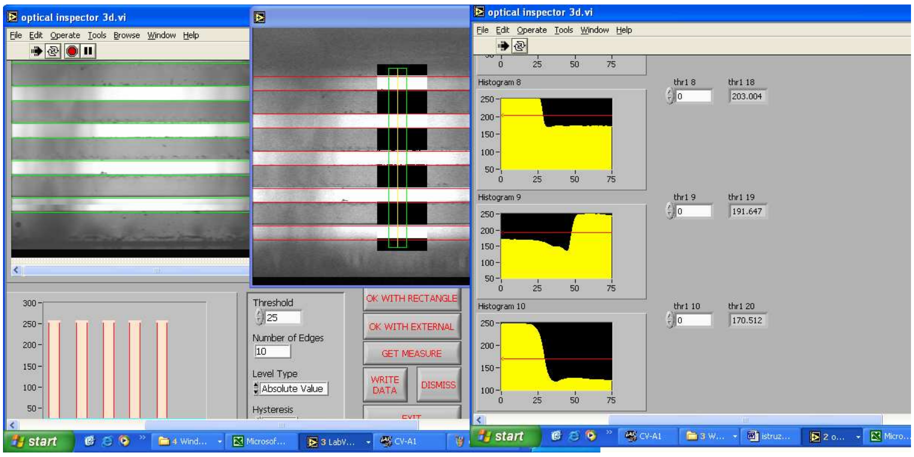

Figure 4.6: image acquisition and luminosity distribution of the light on a gap

parts of the strips (glasses and gaps) and, by an integral of this distribution, it can discriminate between dark areas (glasses) and clear ones (gaps). The result of this operation is a histogram that represents the luminosity distribution of these areas. The number of pixels representing the distance from a dark area to another (i.e. between a glass and the next one) is converted in the numerical values of the gap dimensions, thanks to a conversion factor; the latter is the mean thickness of glasses($\sim$ 400 μm). This operation is made in eight different points of the strip. In fig 4.6 some steps of the Labview analysis are shown, while in fig 4.7 an histogram of the width of some strips shows the mean value of 250 μm of the gap size and the accepted range of measures.

The uniformity of the strip is related also to the resistive paint of the glasses glued on the PCBs. The resistivity of the glasses has to be of the order of magnitude of some MΩ. The first operation on the glasses is to wash them in order to avoid impurities that could change the resistivity in some points; then glass is placed in an stove in order to dry the paint and to set the resistivity at the maximum value; after this step the

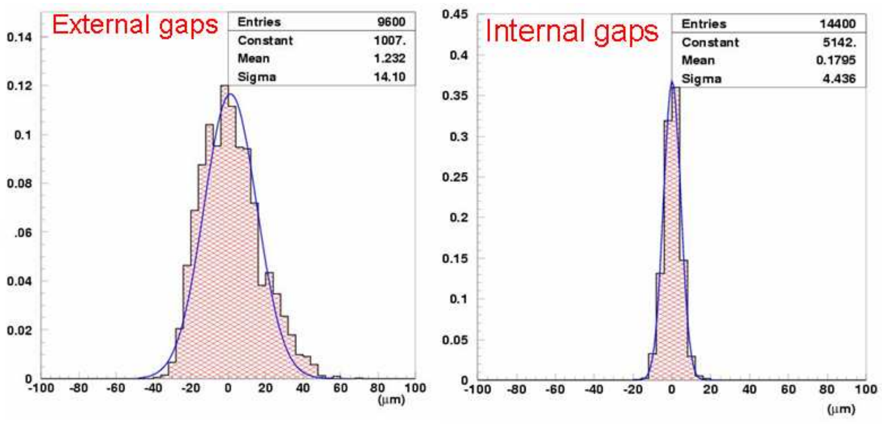

Figure 4.7: range of accepted width of the gaps

resistivity is measured in five different points in order to test the uniformity. When the strips are assembled and soldered, the resistivity is again measured at the edges of the glass; the latter operation allows to check the integrity of the glasses, after the construction; for istance, a high value of resistivity could be a warning for a glass breaking in a certain point).

Signal and High Voltage connections

Signal connections: a possible problem during the soldering of signal connections (open or short circuits between anode and cathode, missing 50 Ω resistance on PCB, etc) can be checked with a wrong rensponse of a circuit planned for these tests and interfaced with a Labview software. In fig 4.8 the signal connectors soldered on the PCBs are showed.

High Voltage connections: PCBs are made by small conductive plates where cables are soldered in order to connect the strips to the HV connectors of modules; the aim of this test is to check the possible onset of dark currents among the electrodes when the high voltage is applied. In the plot of fig 4.9 it is possibile

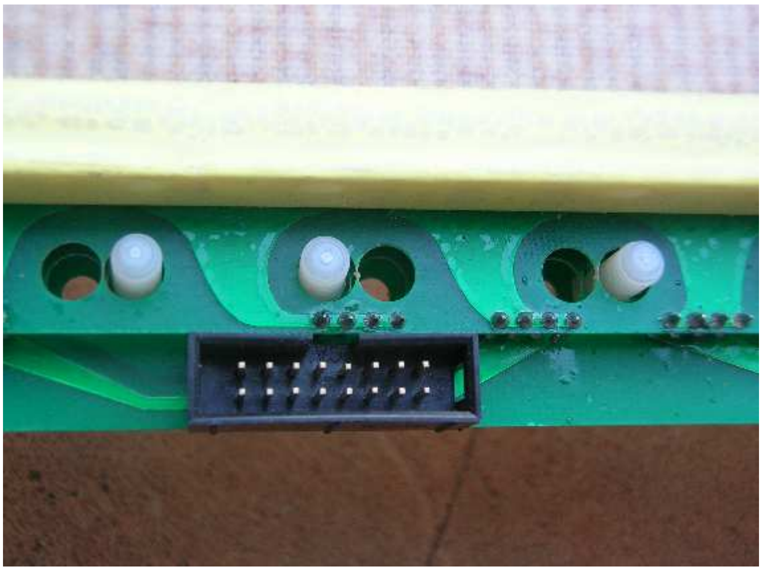

Figure 4.8: signal connector: each connector reads the signal coming from 3 pads

to see the current versus the atmosphere humidity; for humidity values close to 50%, the accepted current values are 2-3 μA; none of the strips has been rejected after this test.

Cosmic Rays Tests

The 1638 strips needed for the TOF have been assembled during two years; a sample of these strips were tested, in order to ensure regular performances of strips constructed in different periods and to study the consequences of possible deficiencies of manufacture; in the fig 4.10a the cosmic rays facility is shown. Five strips are placed one up another, in a special box, with NINO ASIC front-end cards plugged-in. These cards are the same used in ALICE TOF. The central strips are periodically changed, after being selected among the stored ones; instead, the most external strips are never changed and they are used as reference for the testing and as trigger system. In fig 4.10b

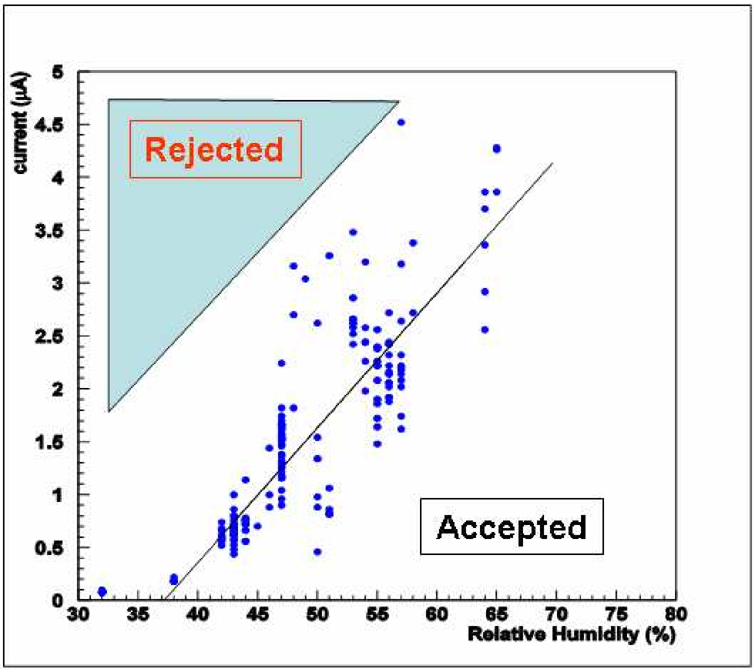

Figure 4.9: HV test

some results of efficiency and time resolution of a sample are shown; they are compared with the values measured at Protosynchrotron at CERN.

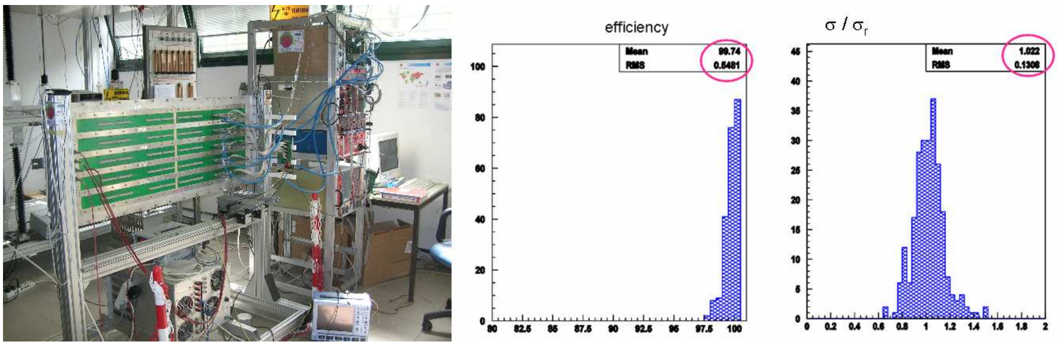

Figure 4.10: a) cosmic rays facility; b) efficiency and time resolution measured at PS (σ = time resolution of the strips tested in Bologna; σ_r = reference PS time resolution

4.2 Modules with MRPCs inside

One supermodule is made with five modules: a central one with 15 strips inside, two intermediate and two external, both with 19 strips. The module is made with a G10 vetronite box that hosts the strips; the dimension of the boxes are different, depending on the module: the central one is 117 cm long, the intermediate one 137 cm and the external one 177 cm. The cover of the module is a metal plate[6] that hosts the Interface Card, where the flat cables coming from the strips and the front-end cards are connected; the inner structure of the box is covered with an aluminuim film, in order to create a Faraday cage.

4.2.1 Tests performed on the modules

After that strips are checked and selected, the high voltage cables are soldered to the PCBs and some other little operations are performed in order to assemble the strips in the modules. As said before, the modules are boxes made by an aluminum basement with an interface card (used to connect the strips to the front-end electronic cards) glued on the top and by a G10 vetronite cover. There are five different modules, geometrically designed to cope with the ALICE space frame architecture (central, intermediate and external); the central one has 15 strips, while the intermediate and the external have 19 strips. In fig 4.11 it is possible to see the base components of the module and a central module with strips inserted and connected inside.

[6]the inner structure of the plate is honeycomb, in order to be strong, but with a less weight

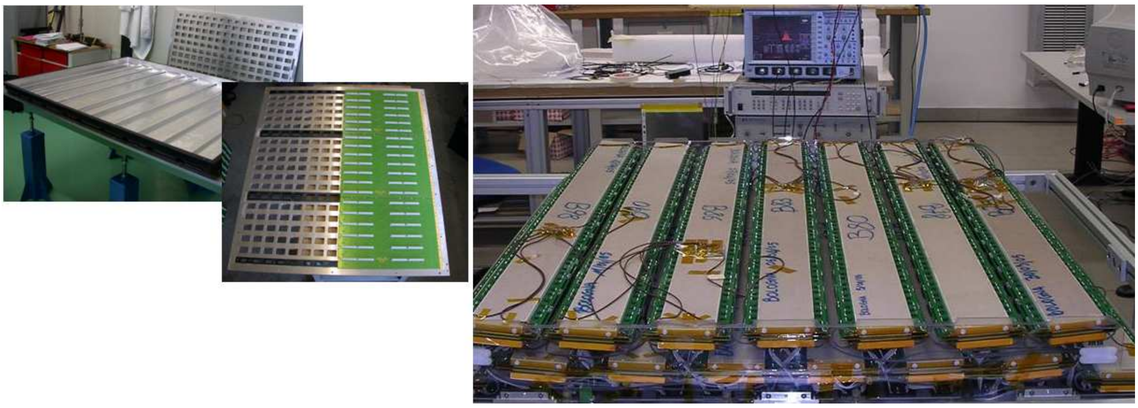

Figure 4.11: parts of the module and an assembled module with the MRPCs inside

Gas Leakage

A very important check to perform on the module is the search for leakage of gas from some points of the module before and after the assembling of the strips inside; the test is carried out using compressed air; a software can monitor the gas pressure inside the module, thanks to a manometer. If the decrease of pressure is lower than 1mb/hour, the module can be considered good.

HV Connections

As the one performed on the strips, the aim of this test is to check the correct performance of the device that provides the voltage to the strips; the HV is provided to the connectors on the two sides of the module. It is possible to monitor dark currents between the electrodes. Two kinds of tests are carried in air: one at HV = 8 kV without strips inside the module, in order to check the quality of the modules' connectors and another one at HV =3 kV with strips inside. Current values of the order of mA are accepted. The strips are connected inside the module,

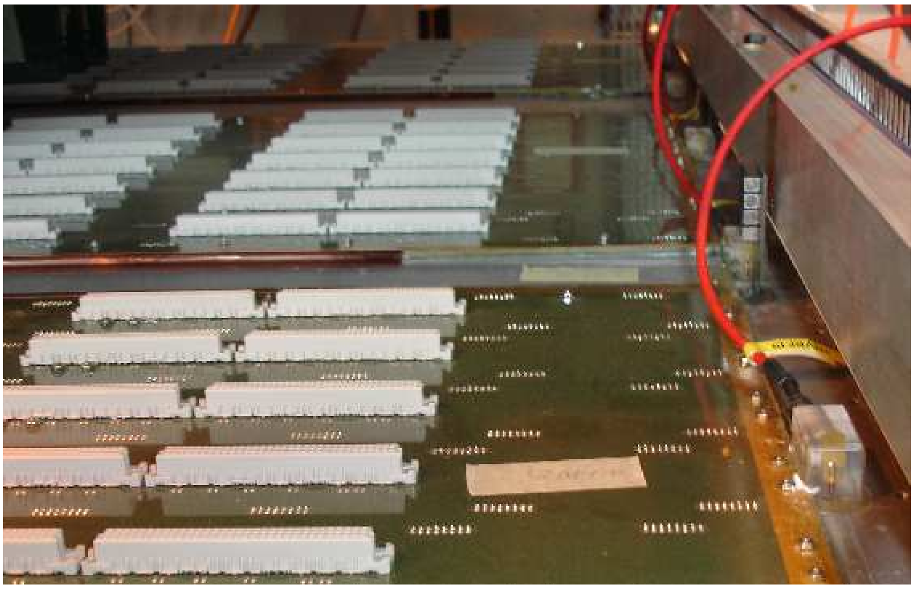

Figure 4.12: HV connectors of a module with strips inside

to the High Voltage distributors, in groups of four; measuring the capacity of the electrodes, it is possible to check if some problems on the continuity of the HV line distribution occurred after the assembling of the strips inside the module. Looking at the value of capacity, it is possible to know if all strips are connected in the right way: the capacity of each single strip is measured before inserting the strip in the module; as the strips are connected in parallel, the total capacity has to be equal to the sum of capacities of the single strips. If this is not the case ($C_{tot} \neq \sum_i C_i$), there are some problems on the HV connections. In fig 4.12 the HV connectors are shown.

Pulser Test

It is needed to check that no hardware problems occurred, such as bad connected signal cables; a square wave signal with amplitude of 5-10 V is pulsed to pads and the efficiency of each single channel is checked by a trigger signal. The output is read through front-end cards and the possible presence of dead channels is studied. In fig 4.13 the FEAs plugged on the module to monitor the pulsed pads are shown.

Figure 4.13: pulser test on a module

4.3 Supermodules

When the modules are declared good, they are sent to the CERN laboratory to be arranged inside a Supermodule (SM). A second level of quality assurance tests concern the TOF modules. The gas tightness is a fundamental demand; this is checked in Bologna after the MRPC insertion, when they arrive at CERN and after the SM assembly operations. Accepted leakage rates are less than 1 mb/h (the average measured value is less then 0.2 mb/h). The signal connection between the MRPCs and the front-end channels is checked, injecting a pulse directly on the MRPC via a special trace on the cathode printed circuit. This pulse will induce a signal on the pads and as a consequence on the full readout chain. This check is performed after the module assembly in Bologna and after the transport to CERN. Once at CERN, all the modules are operated under cosmic rays in the Cosmic Ray Facility shown in fig 4.14 to study their global preformances. The facility contains a stack of five modules; two arrays of scintillator tiles with MRS APD light readout [76] placed at the top and at the bottom of the stack are used to tag cosmic rays. Modules on this facility undergo a one-week gas and HV conditioning; once the working voltage is reached a map of the modules is done with dedicated cosmic runs.

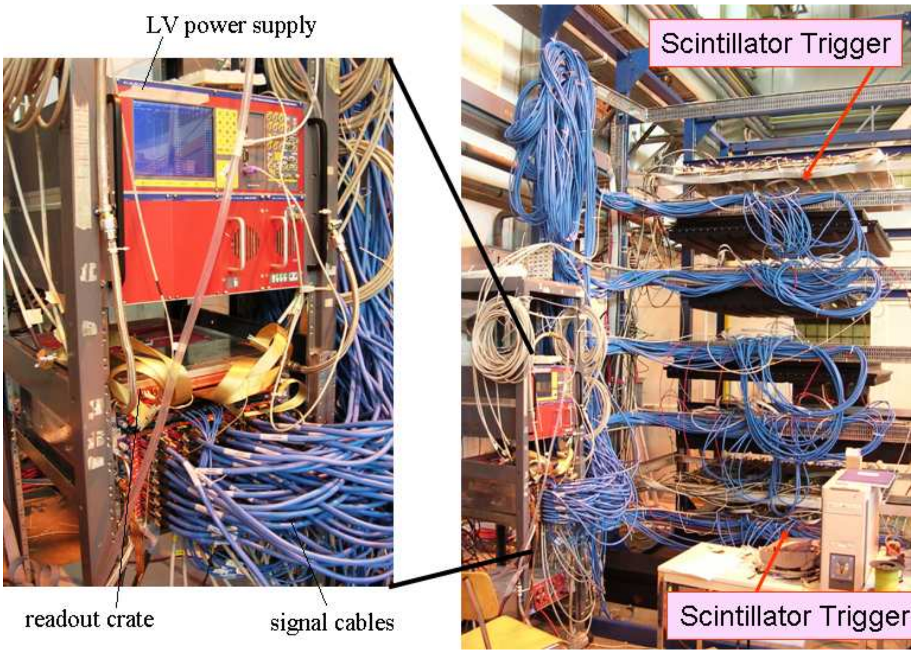

Figure 4.14: picture of the Cosmic Ray Facility at CERN with a stack of 5 TOF modules

Figure 4.15: modules on the assembly table

4.3.1 Assembling of a Supermodule

A SM is assembled arranging the 5 modules on an assembly table and joining them together with aluminium supports (fig 4.15). Two couples of read-out crates are installed at the two edges of the SM. The first step of the construction is mounting of the mechanical structures on the five modules; after having filled the crates with all the read-out boards and after the insertion of the FEAs on the interface cards (4 FEAs per each MRPC strip), the cabling starts: pulser cables, HV cables and signal cables are plugged in. In fig 4.16 some SM details are showed: the cooling pipes, the signal cables and the read-out crate; in fig 4.17 the four FEAs per each strip are visible.

When the cabling is over, the FEAs are glued to the cooling pipes, by some conducting pieces and the FEACs are installed (8 per each quarter of SM). When these steps are over, the areas corresponding to the five modules are covered and the 9m long SM (that looks completed as in fig 4.19) is ready to be tested.

4.3.2 Tests before the assembling of the Supermodule

Before the assembling of a Supermodule, we have to do some tests on the modules (as said before, again tightness and pulser and a cosmic rays test). A very important step is also testing the electronics, before mounting the crates on the two edges of the detector.

Tests on crates and readout electronics

As said in the previous chapter, the ALICE TOF crates are custom VME 9U crates [77], each one containing a 12-slot VME64X bus. Two of these crates are placed at each end of a SM and house a Data Readout Module (DRM), that acts as VME master, a Local Trigger Module (LTM) for trigger purposes, a Clock and Pulser Distribution Module (CPDM) hosted only in one

Figure 4.16: SM details

Figure 4.17: FEAs plugged on the modules

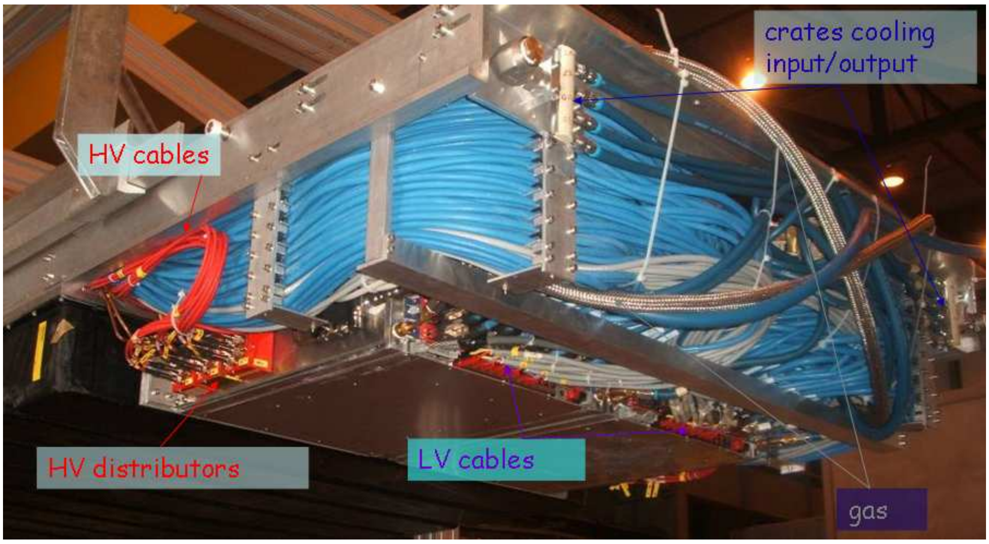

Figure 4.18: details of a SM in the crate area

crate every two, and 9 or 10 TDC Readout Modules (TRMs). The high-current low voltage for the VME boards is supplied by DCDC Converter modules placed inside the crate and designed to operate in a magnetic field (up to 5kGauss) and moderate radiation environment. Each crate fully equipped with all the VME boards is burned out and stressed for at least one week before being accepted. The crate performances including the

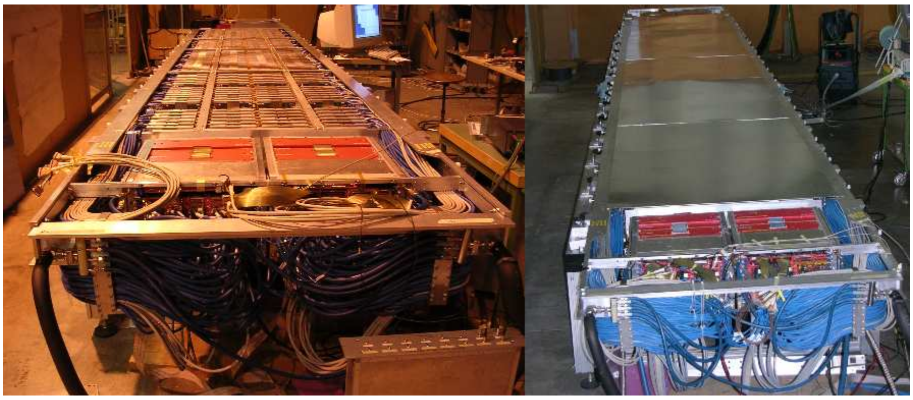

Figure 4.19: a complete SM; this is the first SM assembled on september 2006; a SM weighs 1.4 ton, it is 9.3 m long and it has 8736 elctronic channels

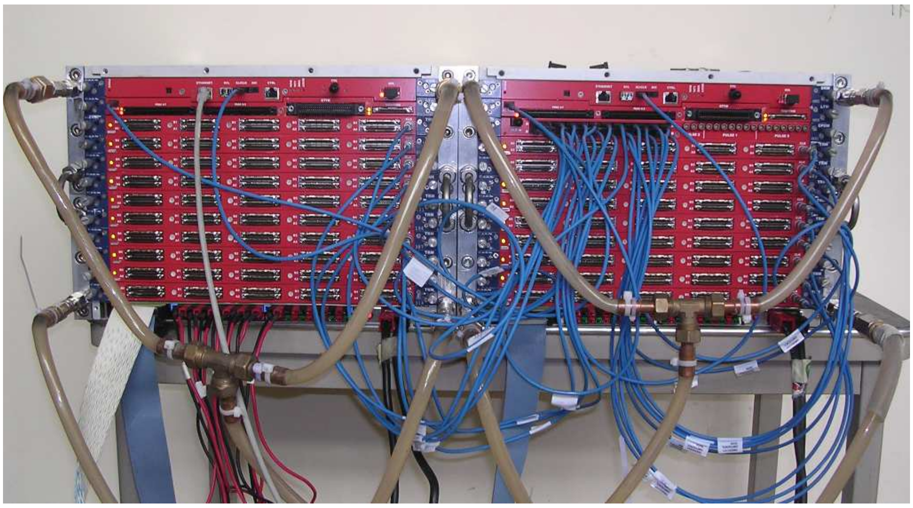

Figure 4.20: picture of the set-up for the tests on the crates and the telnet to the branch controller

readout electronics and the cooling system are checked during this commissioning test. In fig 4.20 the set up to test the crates is shown.

4.3.3 Tests on the Supermodule

During and after cabling a new set of tests starts: gas system, cooling system, LV and HV system, pulser line.

Gas and Cooling system

Gas system: gas-pipe tightness is checked before and after connecting the pipes to the modules. The pipes are filled with compressed air with an overpressure up to 100 mb; no leakage should be check.

Cooling system: the front-end cards and the crate cooling pipes are first tested with air pressure at about 100 mb once the assembly of the SM is completed; if ok, the two complete systems are tested with water at 10 bar for 20 minutes. Several tests have shown that both crates and FEAs (FEAs cooling in fig 4.21) can be cooled to temperatures below the 25 ^{o}C limit required inside the ALICE magnet. In fig 4.21 it is possible to see the temperature lowering when the cooling system is on.

LV and HV system

LV system: because of different cable lengths connecting the FEAs with the crates, all the LV channels have to be tuned in order to feed each FEA with the correct voltage. The LTM capability to provide the signal for the setting of the threshold voltages for more than 90 FEAs is also checked at this time.

HV test: HV up to 3kV is applied to all the MRPCs; besides, all cables and all HV distributors are tested before being plugged on the modules (with a HV up to 14 kV). In fig 4.22 the HV cables and the HV distributors are shown.

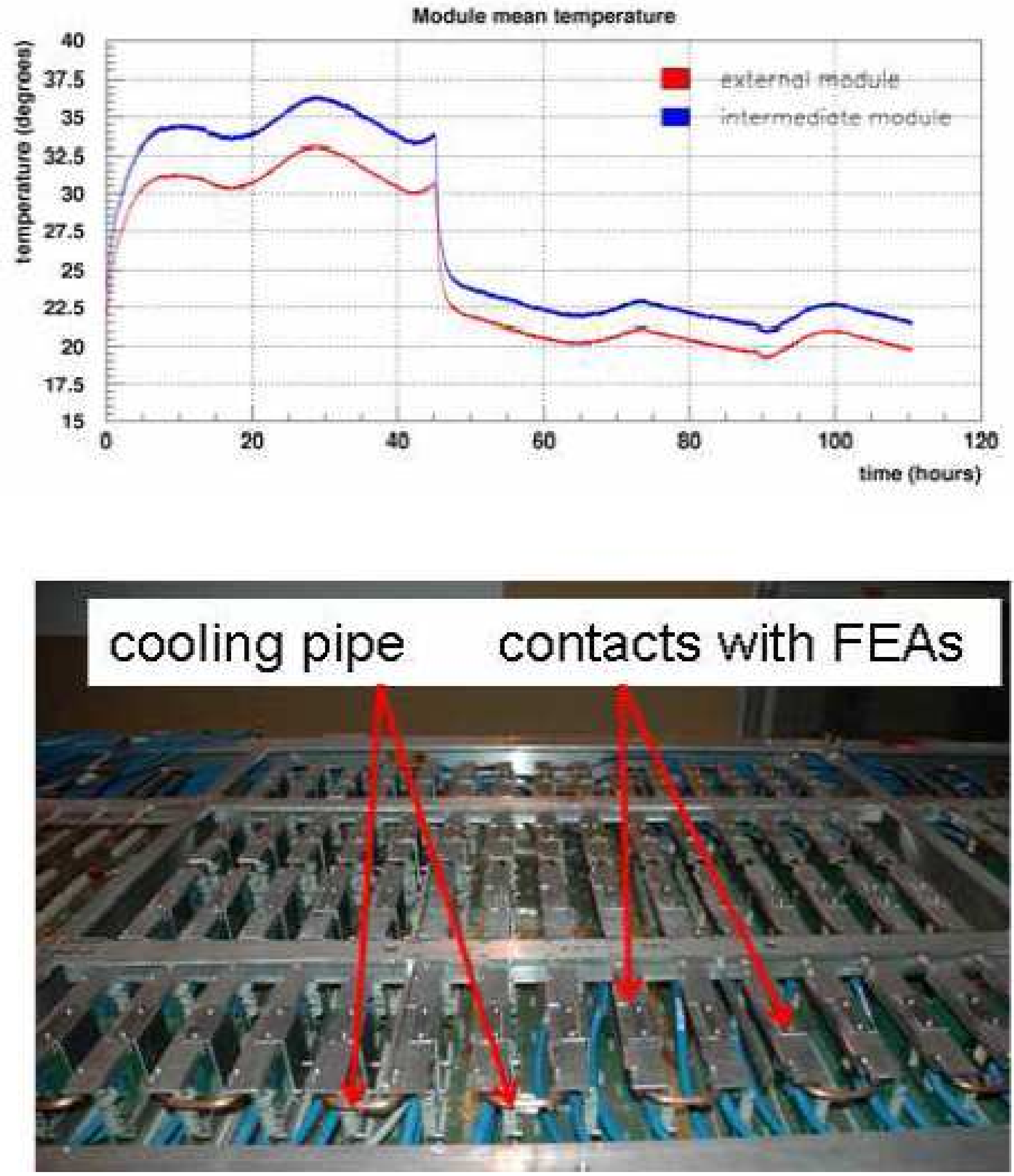

Figure 4.21: cooling system on for two modules

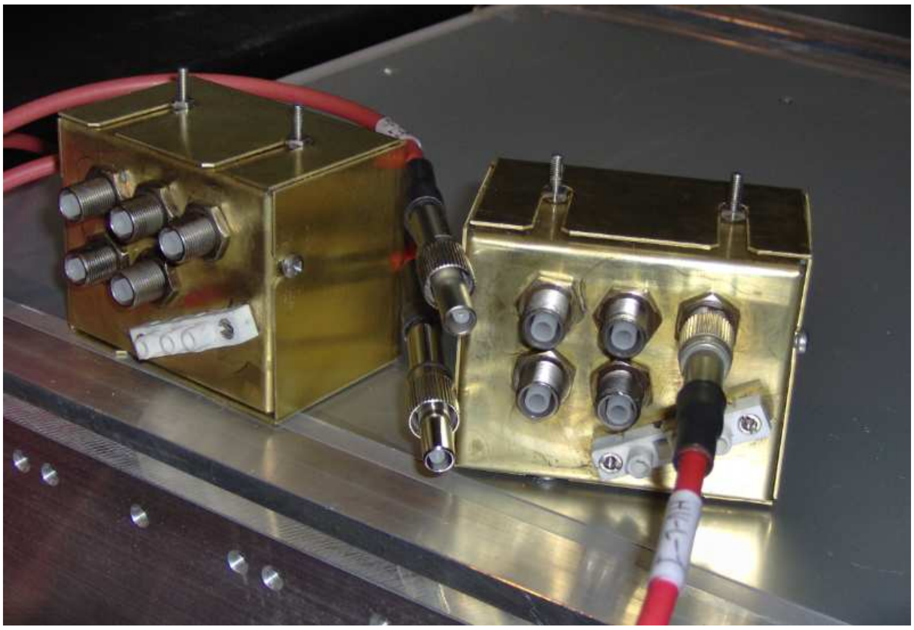

Figure 4.22: HV cables and distributors

Pulser test

This new pulser test is performed inducing a pulse signal directly on the MRPC pickup pads and checking the presence of the corresponding hits on the TDCs at the end of the electronic readout chain, when the Supermodule is already assembled. Fig 4.23 shows the results of a pulser test over a full SM (4 crates); from the plot only two dead channels can be seen. Complementary to these tests are the noise tests, where data for a total time of about 1 second are collected without pulsing the detector, searching for hot electronic channels. Most of bad and hot channels could be restored; the fraction of the remaining channels after the test of 11 SMs (96096 channels) is at the level of few channels over a thousand.

As in the case of most of the other tests, the pulser test is repeated once the SM is installed in the magnet, as part of the commissioning procedure. In fig 4.24 it is possible to see the number of dead channels before and after the installation; we

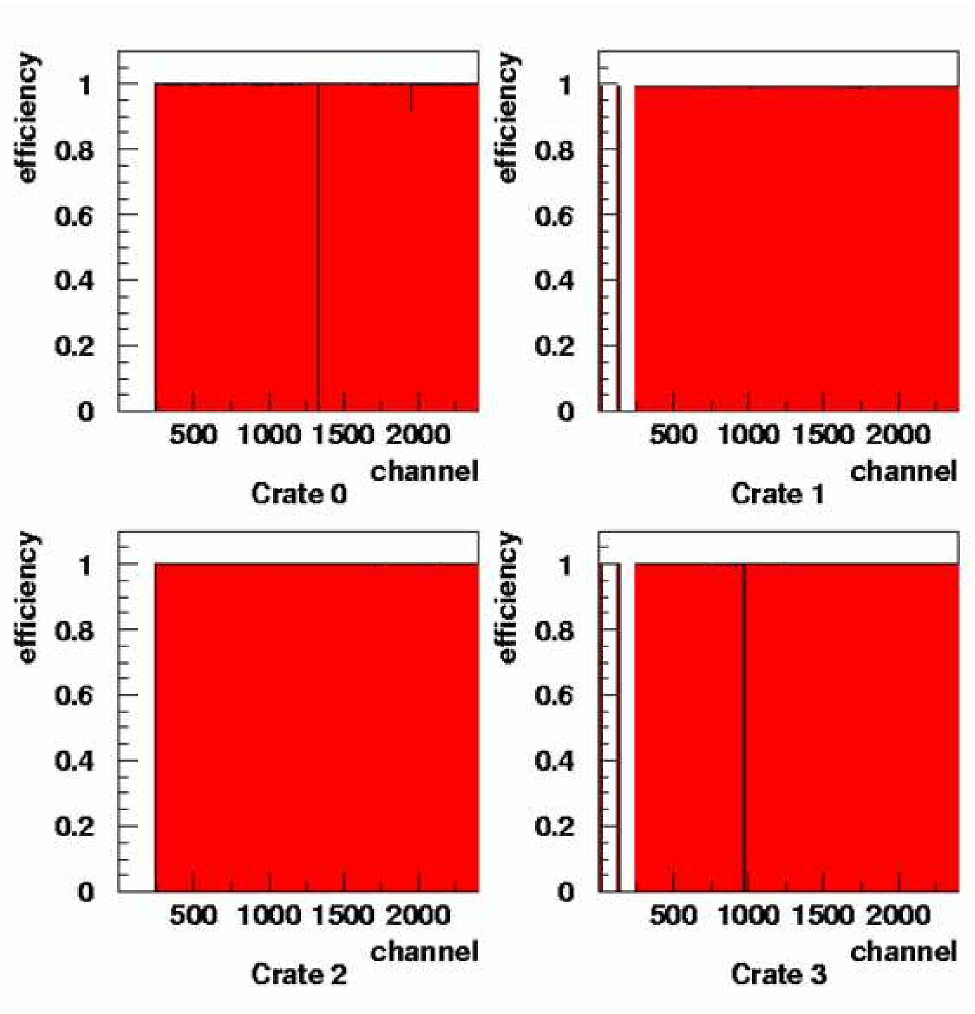

Figure 4.23: result of pulser test on SM10; from the plot only 2 dead channels over a total of 8736 can be seen

can see that the operation of installing the SM in the magnet doesn't cause an increase of dead channels.

The TOF will contribute to the ALICE first level trigger decision, taking the OR signals of couples of daisy-chained FEAs. So, OR tests are performed on the SMs in order to check the proper operation of the TOF trigger chain. In fig 4.25 we can see some results from the OR tst on a SM.

In the next section the monitoring application used to per-

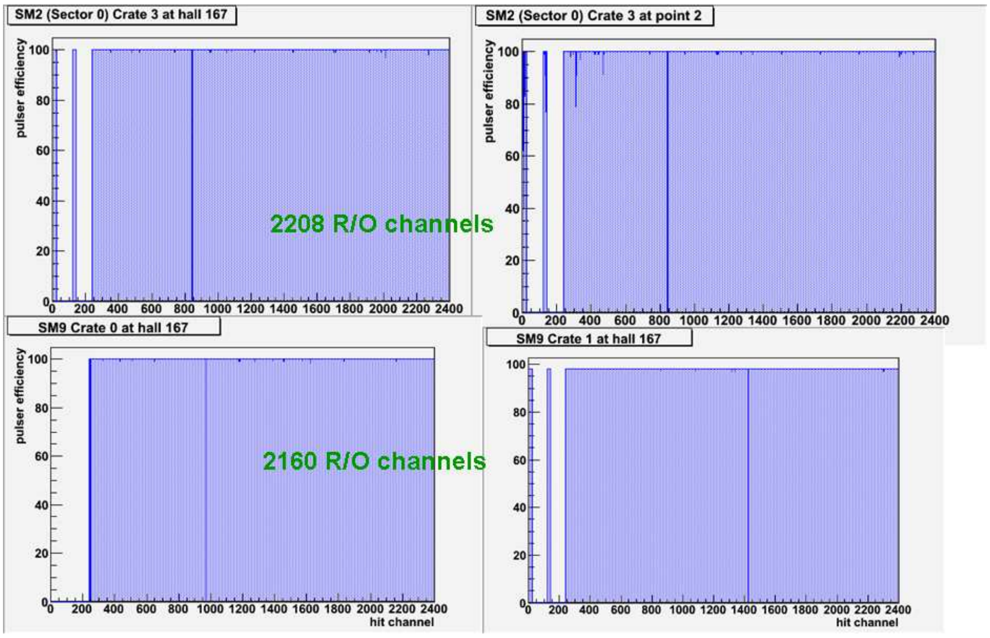

Figure 4.24: result of pulser test after the installation of the SMs in the magnet: total dead channels in SM# 1,2,3,4,5,6,7,8,9 (=78.6 Kch) is about 0.1%

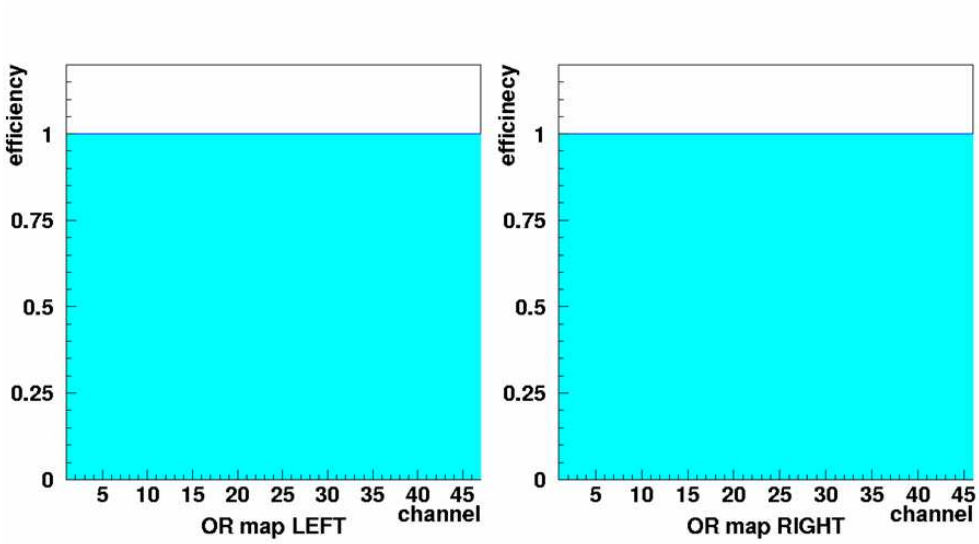

Figure 4.25: OR test: each channel represents the OR signal coming from a FEAC connected to a group of 10 or 12 FEAs (depending on the position of the FEAC in the SM)

form pulser, noise and OR tests is described.

MOOD: an interactive monitoring tool

The online data quality monitoring is an important part of the ALICE DAQ sofware framework (DATE, Data Acquisition and Test Environment) [78]. It allows to detect faulty conditions or bad detector configurations as soon as possible during data taking. Moreover, it is also very useful to have a quick look into the detector behaviour during detector commissioning. For these purposes, an online monitoring application called MOOD (Monitor Of Online Data) has been developed within the ALICE collaboration. MOOD is written in C++ and it is based on the ROOT framework [79] which provides the Graphical User Interface (GUI) and the analysis tools such as histograms and graphs. The use of the DATE monitoring library provides the needed interface to the DAQ and therefore to the raw data stream. MOOD is an interactive application with a plugable structure in which classes containing the detector specific functionalities are loaded at runtime. Specialized MOOD " modules" have been developed in order to monitor the TOF raw data stream produced in a wide set of test environments and have been heavily used since more than one year. All MOOD-TOF modules share a fast and error-safe[7] decoder and a light interactive GUI to present in a set of online histograms the detector status. In fig 4.26 an example of MOOD histograms is showed.

[7]the ALICE-TOF decoding routines have been developed in order to detect data inconsistencies; this functionality prevents unpredictable decoder behaviours due to wrong or corrupted data

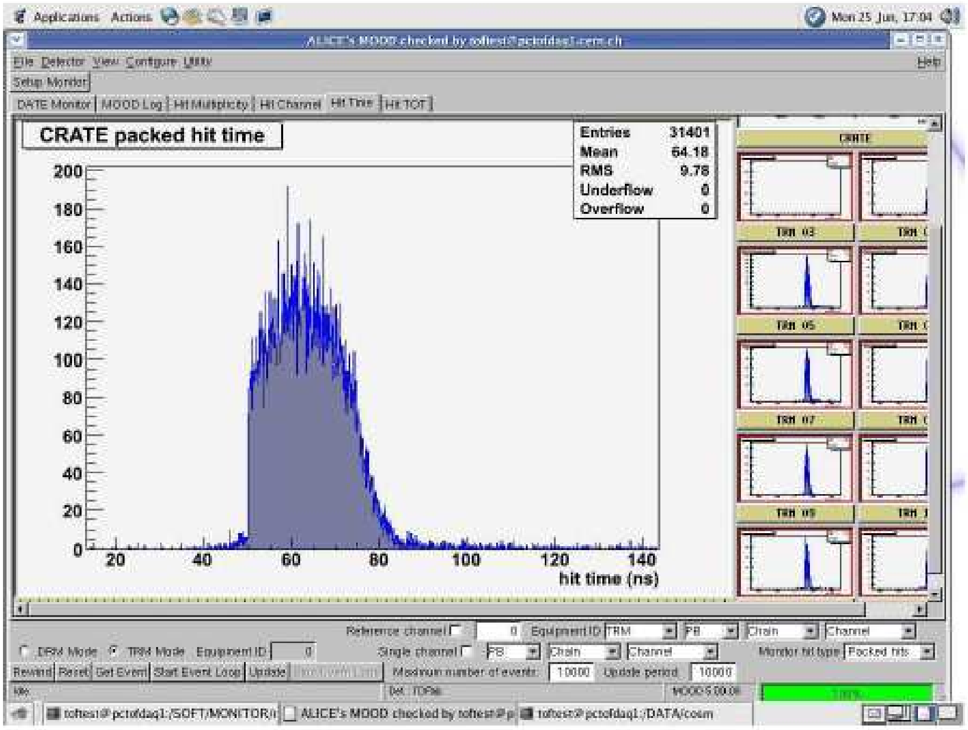

Figure 4.26: screenshot of MOOD-TOF module while monitoring the data taking in the cosmic-ray test facility. The main histogram shows the time distribution of the channels under test; a clearly visible sharp cut in the spectrum signals that the readout electronics has not been properly configured in this case

4.3.4 Tests on the FEACs

This test is performed in University of Salerno Laboratories. In fig 4.27 a picture of FEAC and its scheme is showed.

FEACs have an important task in the SM set-up; they provide the voltage to power on the FEAs and allow to comunicate with them, in order to set the threshold voltages on the discriminator and collect the OR signal from the channels of the daisy-chained FEAs (this is an important signal for the trigger of the experiment); besides, they can monitor the temperature of different areas of the detector, by a temperature sensor inserted in the circuit. The tests performed on the FEACs are:

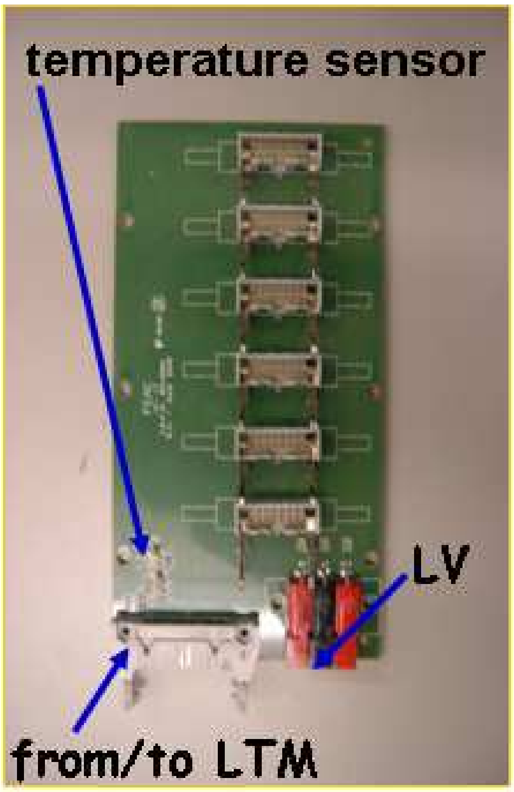

Figure 4.27: Front End ASIC Controller

circuit lines, transmission of the LVDS (Low Voltage Differential Signal) and temperature and calibration V(T,LV).

Circuit lines and LVDS: the first one is useful to check open and short circuits in the circuit lines of FEAC, in order to ensure a good power supply working (test on ground and LV lines) and the right working of OR signals transmission line and thresholds setting lines. In fig 4.28 a circuit made to perform this test is showed. LVDS is the kind of differential signal outcoming from FEAs; the test is carried out sending to FEAC a LVDS signal generated with a FPGA (Field Programmable Gate Array). The output is read with an oscilloscope (see fig 4.29) in order to check the absence of distortions, reductions of the amplitude and crosstalk along the ciruit lines.

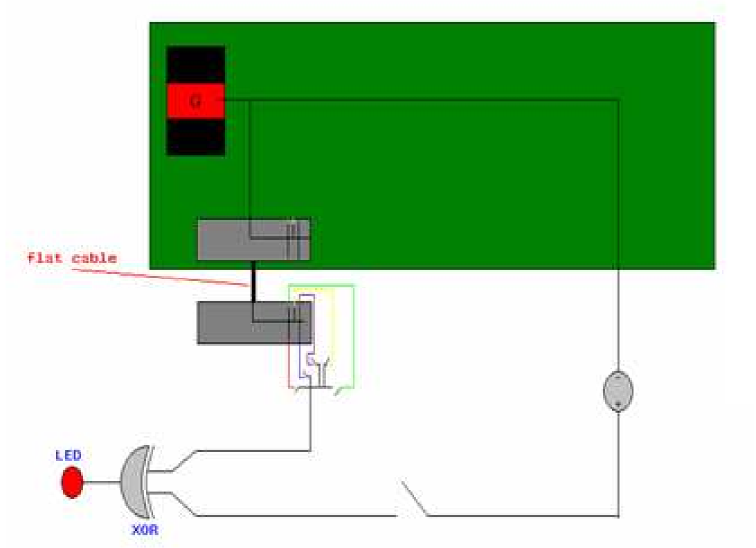

Figure 4.28: circuit used to test the circuit lines of the FEAC

Temperature: FEAC has a low-voltage analog temperature sensor, that works in a range of about fifty Celsius degrees. The test is performed reading the temperature sensor voltage, after having put FEAC at three different values of temperatures: ∼5°C, ∼25°C and ∼35°C. With the achieved data it is possible to check the right working of cards at different temperature values and to get a calibration curve, as showed in fig 4.30; we

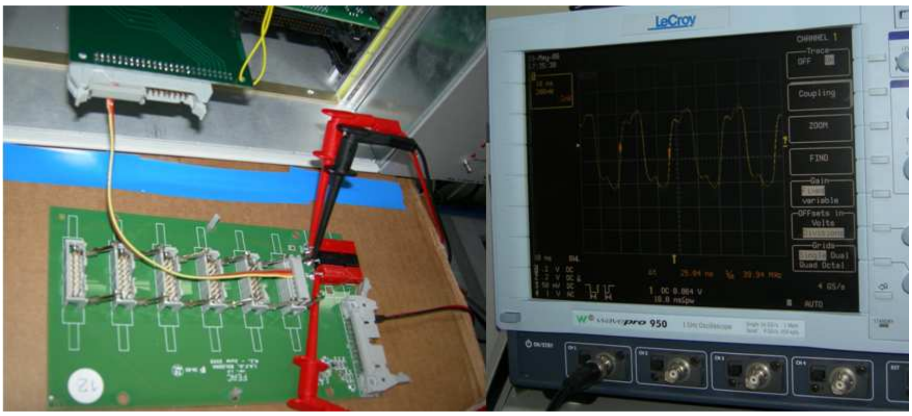

Figure 4.29: LVDS coming out from a FPGA and read with an oscilloscope

can see also the histogram of the difference between the temperature measured by a thermometer and that one measured by the FEAC sensor, in the three ranges considered. This test is very important to have a good temperature monitoring system inside the supermodules, whose electronic cards will work hard for many years.

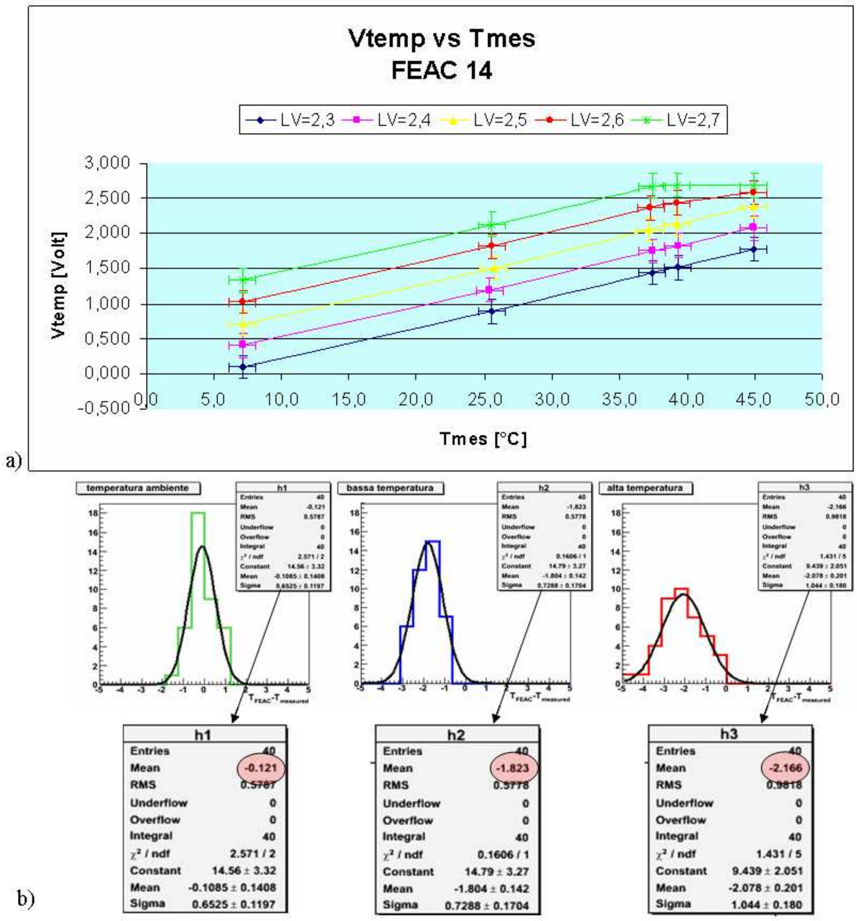

Figure 4.30: a) calibration curve; b) histograms with performance of temperature sensor

After a preliminary period of tests, three Labview applications have been made in order to make the tests easier and faster. In fig 4.32, 4.33 and 4.34 the applications for circuit lines, the LVDS and the temperature are respectively showed.

Figure 4.31: set-up to test the FEACs at different temperature values

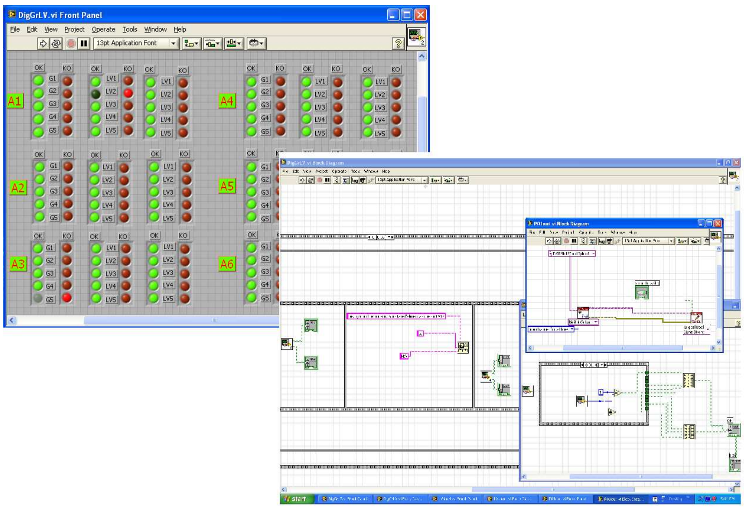

Figure 4.32: Labview application for circuit lines test

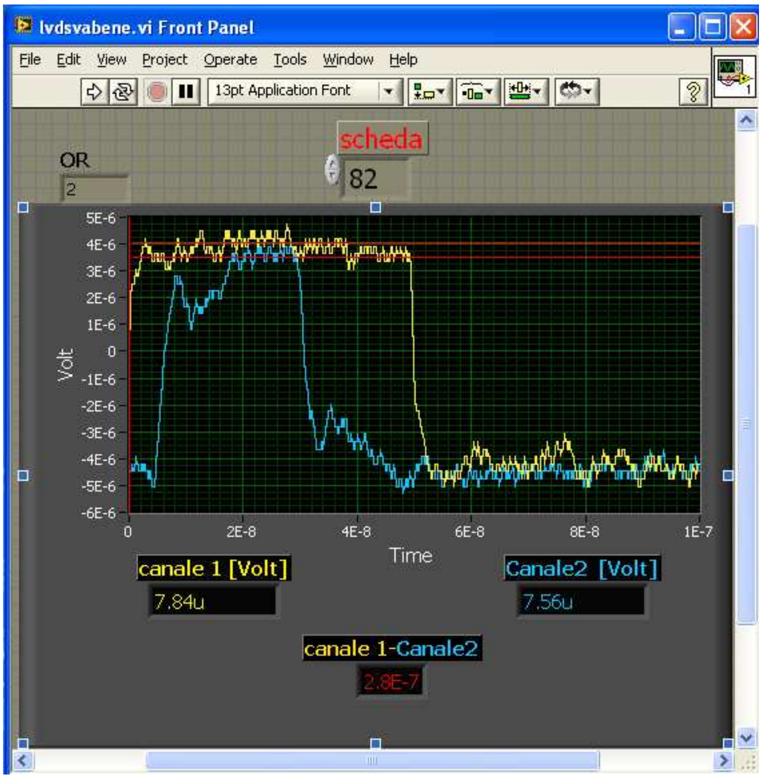

Figure 4.33: Labview application for LVDS transmission test

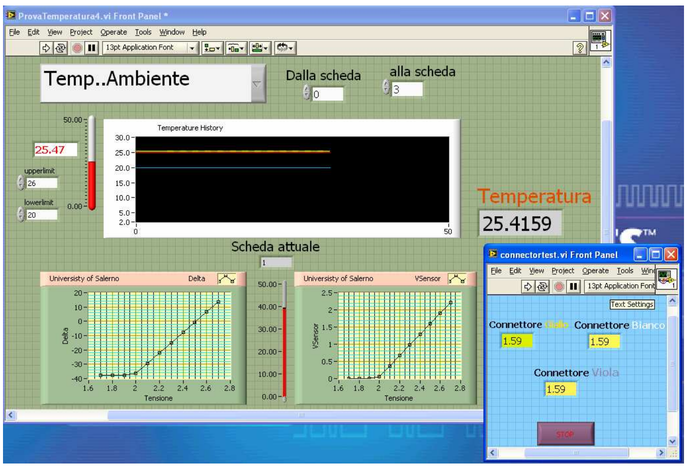

Figure 4.34: Labview application for temperature test

4.4 Commissioning in the magnet

In fig 4.35 the ALICE magnet with 14 SMs installed is shown. The installation of a SM is a complicated and delicate operation; it is performed with the help of some mechanical structures used to bring the SM, to rotate it and to achieve the right angle, in order to install the SM in the 18 different sectors of the TOF frame. After the installation the commissioning stage starts, i.e. final cabling, cooling and gas tightness tests and power on and read-out tests.

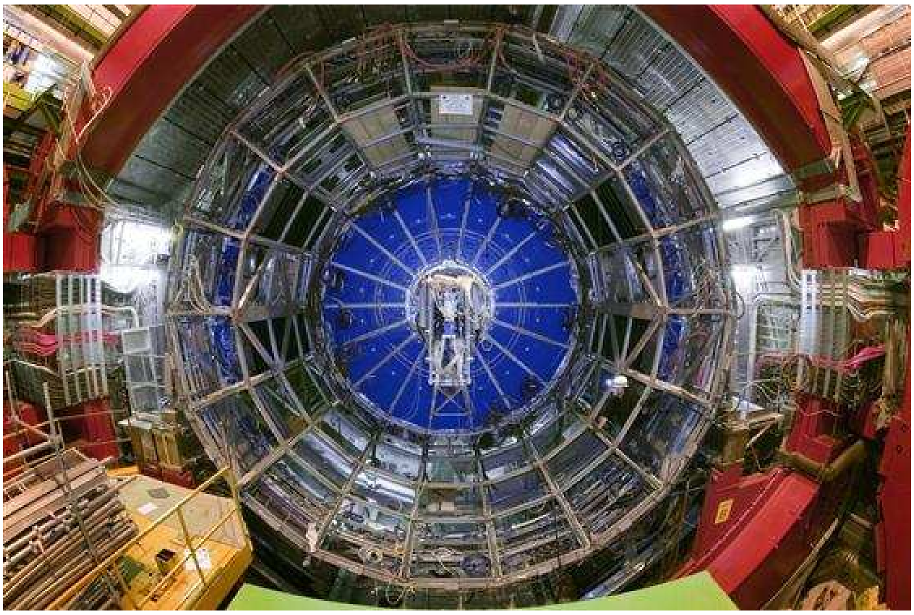

Figure 4.35: some SMs installed in the magnet

In fig 4.36 the three structures for the SMs installation are shown.

Figure 4.36: tools used to install the SMs in the ALICE magnet

4.4.1 First steps of commissioning

The cabling in the magnet consists in plugging:

- plugging HV cables coming from ALICE services system in the SM distributors
- plugging power cables to provide 48 V to switch the crates on
- plugging brunch control cables, used to monitor and power on all the LV channels of the crates
- connecting gas ALICE pipes to the SMs connectors
- connecting cooling pipes to the SMs connectors

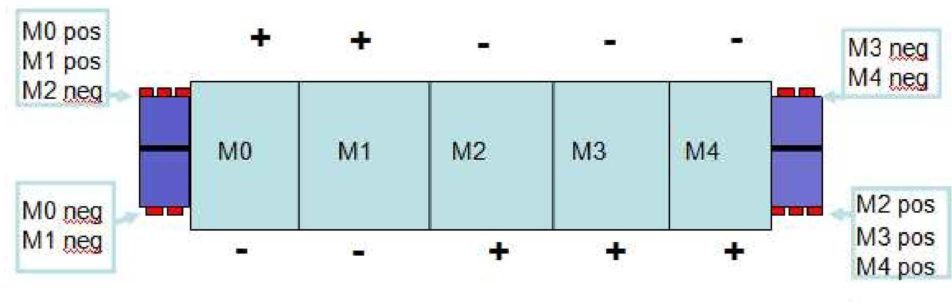

Figure 4.37: scheme of positive and negative HV ditributors on the SMs

after each operation some tests on the connected cables and pipes are performed in order to complete the commissioning phase. In fig 4.37 the HV distribution in a SM is showed; instead in fig 4.38 is showed the screen with the LV channels list that can be used, via branch control, to switch on/off the LV system and all the boards of the crates (DRMs, LTMs, CPDMs and TRMs).

4.4.2 Fibres and connectors

This section summerizes the installation of the passive hardware elements (optical fibres, patch panels and tubes) of different categories of optical links at the experimental area Point 2 used by ALICE (fig 4.39). These elements of the infrastructure will be shared by the following optical links: the Detector Data Link (DDL), the Trigger Timing and Control (TTC), the TRD detector readout and pre-trigger, the TOF detector control , the TOF precision clocks, the ITS SDD readout, the ITS SPD control and readout and the pixel trigger control.

The DDL is constituted by two multimode ($50\mu/125\mu$) opti-

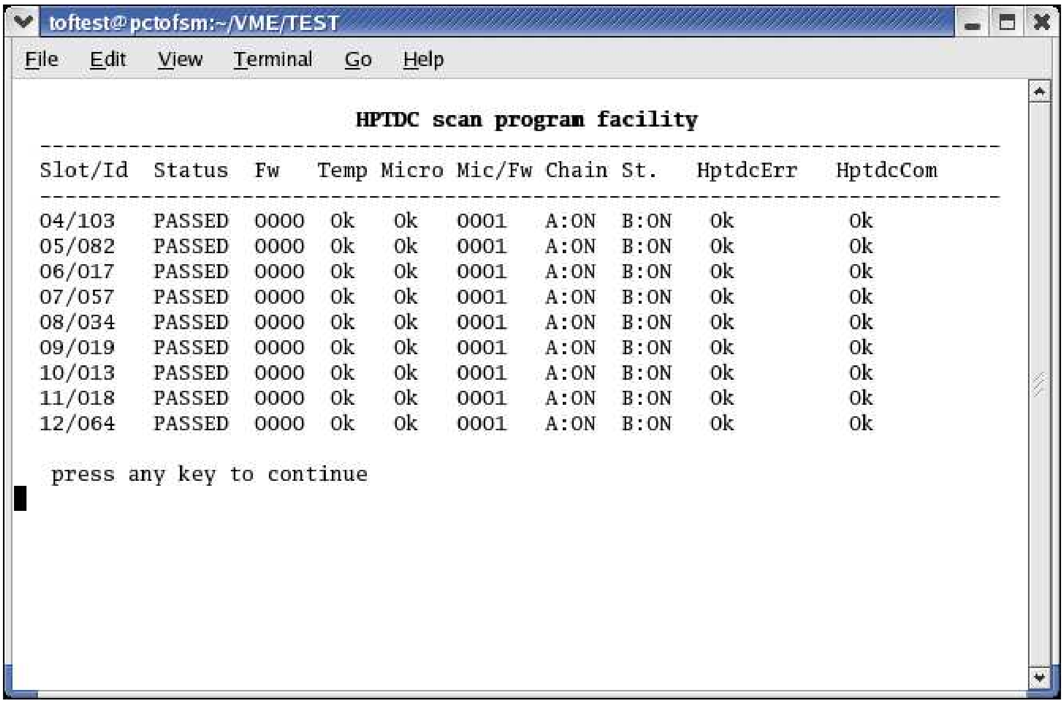

Figure 4.38: telnet to the LV channels via branch control

cal fibres. The connectors are of two different types:

- all the patch panels will be equipped with E2000 connectors
- all the DDL host bus adapters in the computers and all the DDL link cards on the detectors will use LC connectors

The TTC is constituted by one single mode optical fibre. The connectors are all of the ST type. The TRD readout link is constituted by one multimode ($50\mu/125\mu$) optical fibre. The connectors are of two different types:

- the patch panels on the backframe will be equipped with E2000 connectors
- the patch panels in the racks in the C area will be equipped with LC connectors

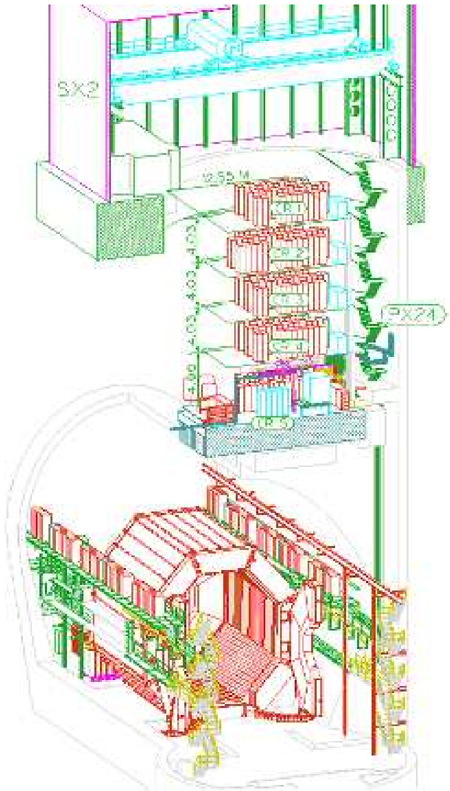

Figure 4.39: the ALICE acces shaft and experimental area

- all the TRD sender on the detectors and all the TRD receivers on the GTUs will use LC connectors

The TOF slow control is constituted by two multimode ($50\mu/125\mu$) optical fibres. The connectors are of two different types:

- all the patch panels will be equipped with E2000 connectors
- the other end of the patch cords will use LC connectors

The TOF clock is constituted by one single mode optical fibre. The connectors are of two different types:

- all the patch panels will be equipped with E2000 connectors

- all the TOF clocks sender and all the TTC receiver chips on teh detectors will use ST/PC connectors

The ITS SPD detector control and readout is constituted by three singlemode optical fibres. The connectors will be of two different types:

- MU on the detector side and the corresponding patch panel on the detector
- LC on the router side and E2000 on hte correspondingpatch panel

The ITS SDD detector readout is constituted by three singlemode optical fibres. The connectors will be of three different types:

- MU on the detector side and the corresponding patch panel
- LC on the CARLOSrx side
- MPO for 12 fibres (ribbon or cable) in all the patch panels

4.4.3 DDL Layout

The DDL optical fibres constitute the physical layer for the transfer of physics data from the detectors to the Data Acquisition (DAQ) and High-Level Trigger (HLT) systems and for the transfer of some control and configuration data from the DAQ to the detectors electronics. The core of the ALICE is installed in the counting room CR1 located in the acces shaft PX24. The core of the ALICE HLT system is installed in the counting rooms CR2 and CR3 located in the acces shaft PX24 (see fig 4.40). Every DDL is fully-duplex: its physical layer is constituted by two optical fibres. Four groups of DDL fibres were used by ALICE in the different periods of test, first commissioning and experiment. The DDL used for data transfer during the global commissioning period of the whole experiment are been laid down between the experimental hall UX25 and the DAQ counting room (PX24/CR1). Most of these fibres are made of three sections:

- a patch cord from DDL link card located on the detector to a patch panel located close to the detector
- a fixed section from the patch panel on the detector in UX25 up to a patch panel located in room PX24/CR1
- a patch cord from the patch panel laocted in room PX24/CR1 up to a computer located in the same room

The other DDL (such as the ones originated from the TPC on the Side A) are made of five sections:

- a patch cord from DDL link card located on the detector to a patch panel located on the mini-frame[8]
- a fixed section between two patch panels located on the mini-frame
- a patch cord from the patch panel on the mini-frame to a fixed patch panel located in UX25
- a fixed section from the patch panel in UX25 up to a patch panel located in room PX24/CR1

[8] inside the ALICE magnet, there are some structures in which the detectors are installed: the space-frame is the central part of the frame, the back frame is the frame in the direction of the forward detectors and the baby-frame is the one in the direction of the magnet doors; the mini-frame is the frame that hosts the services for V0, T0, PMD, ITS and TPC

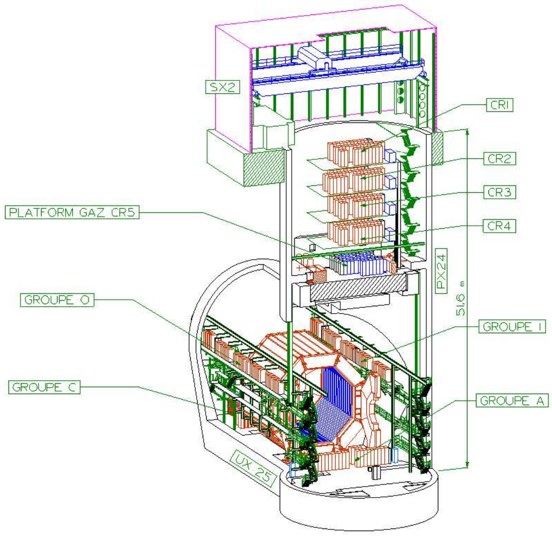

Figure 4.40: location of racks in the ALICE experimental area

- a patch cord from the patch panel located in room PX24/CR1 up to a computer located in the same room

Chapter 5

A Study on the Pad Clusters Using First Cosmic Muon DATA

In this chapter some analysis results of the data from the cosmic rays runs performed in December 2007 and February - March 2008 are shown. An analysis on the clusterization process of hit pads has been performed in order to improve the tracking of the cosmic muons in the TOF detector. The information of the Time Over Threshold (TOT) has been used to better estimate the position of the muon impact point on the TOF sensitive elements. This analysis can be used also during the data analysis of ALICE experiment. In fig 5.1 a muon crossing one of the TOF supermodules is shown.

5.1 Cosmic Rays Run

Before starting the LHC p-p and Pb-Pb collision runs, an intense activity on the commissioning of the TOF detector has started both on the integration of the TOF in the ALICE apparatus and on the performance test of the installed supermodules. A "natural" relativistic particle source, i.e. cosmic rays, has been used in order to check the quality of the detectors and the integration in the DAQ and Detector Control (DCS) Systems. In fig 5.2 and 5.3 the DCS platform, written with PVSSII software, for the TOF supermodules is shown. It is possible to see the panel with all crates of the SMs; for each crate, there is the possibility to switch on all the LV channel for front-end and read-out electronics: the PVSS project includes the automatic sequence for switching ON/OFF the boards of the crates (it is very important to respect it, in order to avoid problems to the HPTDC chains of the TRMs); but it is also possible to do it manually if necessary. To monitor the current relative to each board and the status of the card inside the board is also implemented.

The PVSS project allows to monitor and to act on each supermodule and on the services (i.e. gas system and cooling system); in the fig 5.3 the panel with the two supermodules used during the December 2007 run (SM00 and SM08[1]) is shown, with the relative status. In this case an error status on the infrastructure was simulated, in order to check the quality of the DCS monitoring system. The cosmic runs have been very useful to find bugs in the system and also to perform the integration of the sub-detectors; some runs including different sub-detectors have been successfully performed. On December 2007 SM00 and SM08 were included in the runs. On February - March 2008 other SMs have partecipated to the runs: SM0, SM1, SM7, SM8, SM10 and SM16. Both on December and March, the tracking detectors ITS and TRD have been present and their integration in the DAQ system was successfully performed. The main ALICE tracking-system, i.e. the TPC detector, was not present during the runs. The trigger to record data have been done by

[1]SM# is the number of the TOF sector inside the frame sector; this number increases according to the azimuthal angle value (ϕ)

the ACORDE scintillators, located on the upper octant of the barrel magnet as shown in fig 5.4.

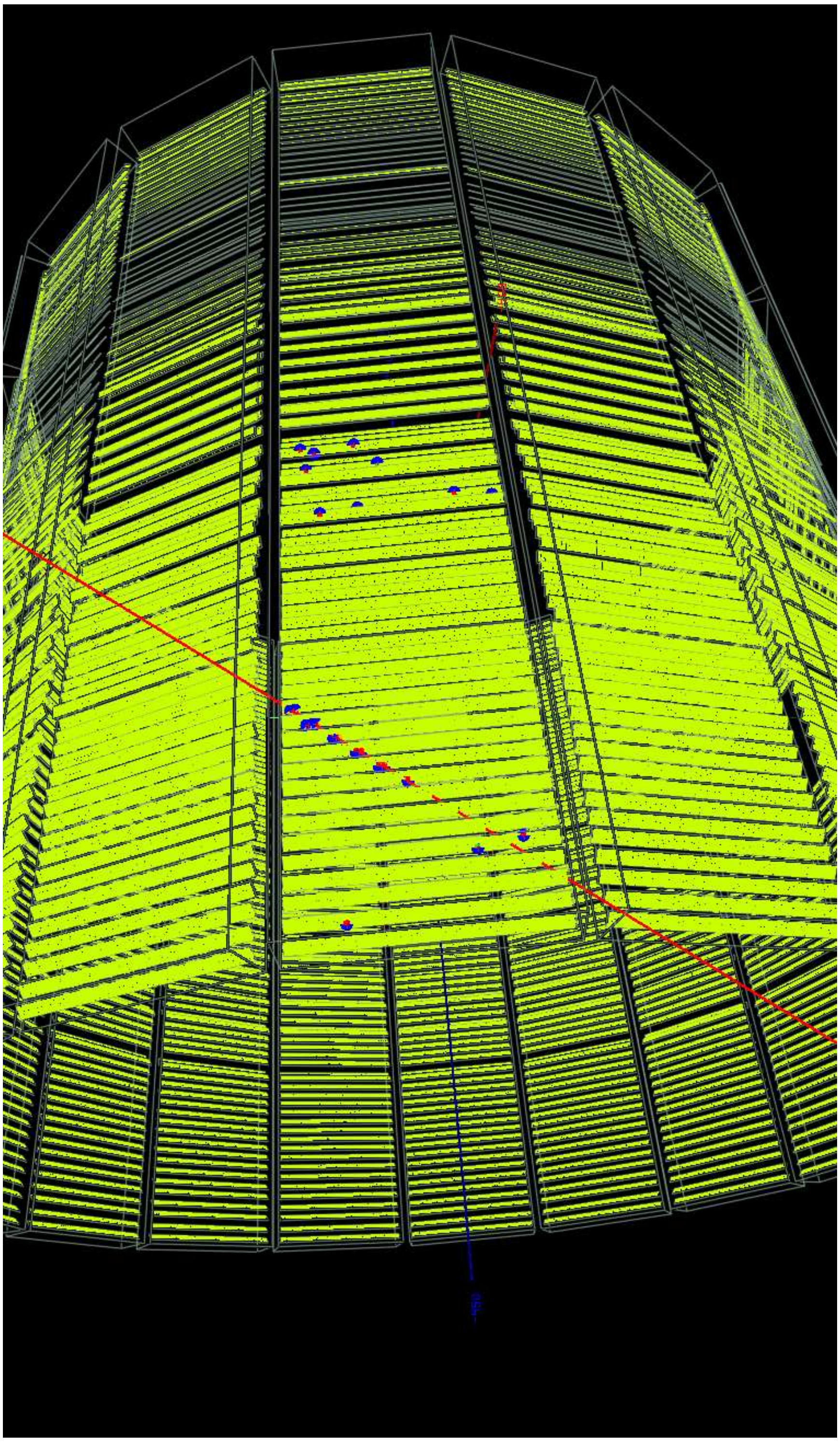

Figure 5.1: event display showing a cosmic muon crossing one of the TOF supermodules. In yellow the TOF stips are shown; the red line is the muon reconstructed track, while the coulored points are the hit pads

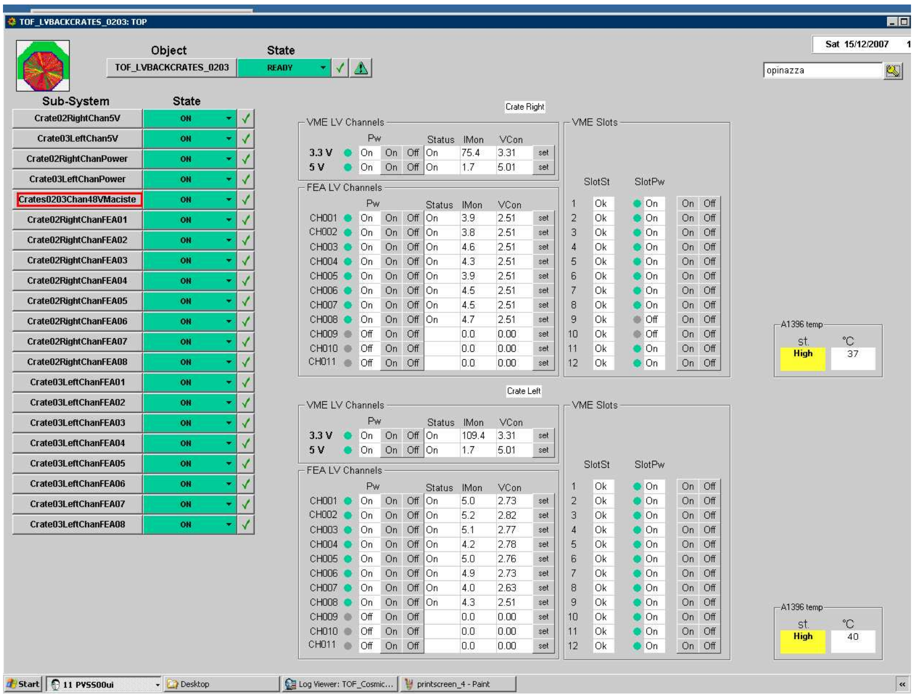

Figure 5.2: PVSSII project for TOF system

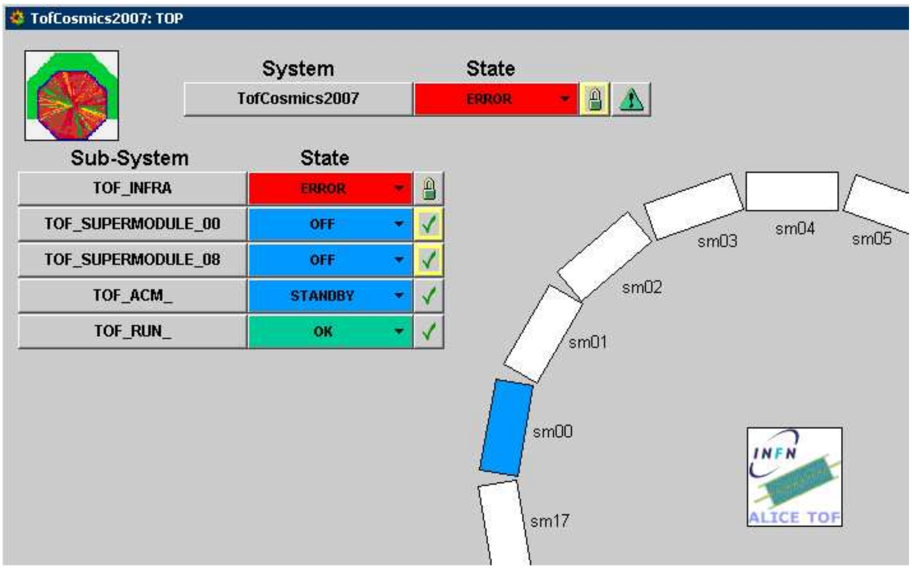

Figure 5.3: PVSSII project for TOF system

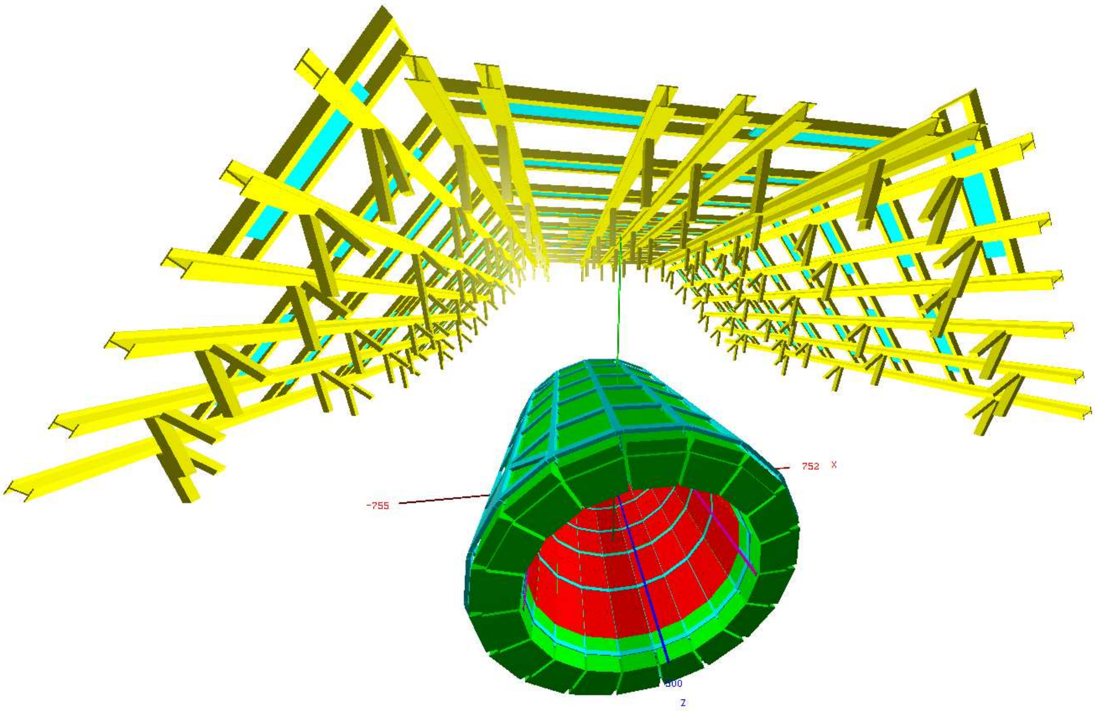

Figure 5.4: a perspective of ACORDE and TOF. The yellow elements represent the carring structure for the sensitive elements of ACORDE (the blue ones). The inner cylindrical shell represents the TRD detector, while the green external one is the TOF

5.2 Reconstruction

Most of the ALICE detectors are tracking detectors. Each charged particle going through the detectors leaves a number of discrete signals that measure the position of the points in space where it has passed. The task of the reconstruction algorithms is to assign these space points to tracks and to reconstruct their kinematic parameters. This operation is called track finding. In ALICE a track-finding efficiency for tracks down to $p_t = 100$ MeV c^{-1} is required, even at the highest track density, with occupancy of the electronics channels exceeding 40% in the TPC inner rows at the maximum expected track multiplicity. Given this situation, most of the development is done for Pb-Pb central events, since lower multiplicities are considered an easier problem once the high-multiplicity ones can be handled. However, the opposite may be true for some quantities, such as the main vertex position, where the high track multiplicity will help to reduce the statistical error. A preliminar study of the tracking in the TPC has been done, using a classical approach where cluster finding precedes tracking. Clusters in pad-row and time directions provide the space points that are used for tracking with the Kalman filter [80].

The overall tracking starts with the track seeding in the outermost pad rows of the TPC. Different combinations of the pad rows were used with and without a primary vertex constraint. Typically more than one step is done, starting with a rough vertex constraint, i.e. imposing a primary vertex with a resolution of a few centimetres and then relaxing it. Then the track candidates are propagated in the TPC using Kalman filtering. When continuing the tracks from the TPC to the ITS during the first pass, it is imposed a rather strict vertex constraint with a resolution of the order of 100 μm or better. The other pass is done without a vertex constraint in order to reconstruct the tracks coming from the secondary vertices well separated from the interaction point. At this point, the estimates of the track parameters and their covariance matrices in the vicinity of the interaction point are obtained. The next step is to proceed with the Kalman filter in the outward direction. During this second propagation, the space points with large χ^2 contributions are removed from the track fit. In this way the track parameters and their covariance matrices at the outer TPC radius are obtained. Then, it is needed to continue the Kalman filter into the TRD detector and then to propagate the tracks towards the outer detectors, TOF, HMPID, and PHOS.

The starting sample for the track-TOF signal-matching procedure consists of all the TPC tracks which can be successfully extrapolated from the TPC outer wall (at a radius $R \sim 2.6$ m) to the TOF inner radius ($R \sim 3.7$ m). Track extrapolation to the TOF is performed by track reconstruction in the TRD. In general, the use of the TRD spatial information allows one to further constrain the track trajectory, thereby improving the quality of the track extrapolation and its association to the time signals on the TOF system. However, owing to the quality criteria applied during track reconstruction in the TRD, which cause the track extrapolation to be stopped when regions with a relevant amount of passive material are crossed (in particular, close to the boundaries between TRD modules), a sizable fraction of the tracks releasing a signal on the Time of Flight system actually fails to be extrapolated to the TOF inner radius. As that would imply a significant loss of efficiency in the TOF PID procedure, a further extrapolation step is applied to recover the tracks stopped during the TRD reconstruction. In this case, the extrapolation is performed without applying the requirements mentioned above, and using average values of the density and the radiation length of the material crossed to take into account the effects from energy loss and multiple scattering. Following this procedure, nearly 100% of the TPC tracks which have released a signal on the TOF system are eventually included in the starting sample of the track-TOF signal matching algorithm. In terms of the performance of the matching algorithm, the inclusion of the latter set of tracks translates to a substantial gain in the association efficiency (a factor $\sim$ 1.3-2, depending on the track momentum), with only a limited increase (a factor $\sim$ 1.1) in the rate of fake associations. Note that an extrapolation procedure complementing the one performed by the TRD track reconstruction will be even more necessary in the case of a reduced geometrical acceptance of the TRD, as foreseen for the experiment start-up phase.

After extrapolation to the TOF inner radius, the tracks are sorted according to their curvature, so that the matching procedure is first applied to the highest momentum tracks. The ordering in momentum contributes in reducing the contamination from fake associations. After that, a window $[d\varphi, dz]$ in the azimuthal and longitudinal coordinates (which depends on the track parameters and their errors) is opened for each track, and TOF pads that have given a signal are searched for within this window. These pads are preselected as candidates for the association. The matching procedure is then organized in two stages:

- In the first step, each track is propagated through the TOF detector, until its extrapolation crosses one of the preselected TOF pads. The time signal of this pad is then associated to the track.

- In the second step, the same procedure, but with a looser criterion, is applied to all those tracks whose extrapolation did not fall within the active area of any of the preselected TOF pads. In particular, the TOF signal closest to the track trajectory is associated, provided that its distance is smaller than a predefined value d_{max}. In Pb–Pb collisions, a distance $d_{\text{max}} = 3$ cm, which optimizes the ratio between the matching efficiency and contamination in central events, is used. In the case of pp collisions, which are characterized by a much lower charged track density, a more inclusive cut is applied, $d_{\text{max}} = 9$ cm.

During both steps, the association of the tracks is performed according to the ordering in momentum mentioned above; moreover, once a TOF signal is assigned to a track, it is flagged to prevent any further association to other tracks, to avoid ambiguous track-time assignments.

5.3 New Clusterization Algorithm for TOF Signals

As said in the previous section, the last step of the reconstruction is the propagation of the tracks towards the outer detectors, to associate their measurements to the reconstructed tracks. For this reason, it is important to have a precise method to associate the fired pads to the tracks coming from the tracking systems. The method currently used performs associations like TOF hit pad - track and it gives very good performances in terms of tracking and PID efficiency (see fig 5.104 and 5.108 in [82]). Anyway this algorithm can be further improved by recovering the correlations between two, three or four signals collected by neighbouring pads on the same TOF MRPC strip. To understand this point it is important to recall how the MRPCs work. A charged particle passes through the gas volume of the chamber and ionizes the gas mixture; thanks to an electric field applied to the electrodes, the positive ions and the electrons go towards the electrodes, where the signal is collected and sent to the FEA cards. In fig 5.5 an example of this process is shown: since the TOF sensitive elements are read by a 2×48 pad matrix, it is possible to have two cases: in the first one (shown on the left of fig 5.5), the particle produces an avalanche that is collected on the pad corresponding to the crossed volume; in the second case (shown on the right of fig 5.5), the avalanche give signals on more pads. When the signal is induced on more than one pad, we have a cluster of hit pads.

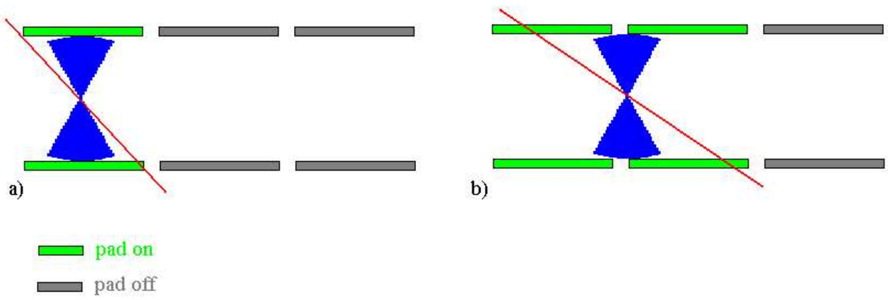

Figure 5.5: a) one charged particle gives signal on one pad; b) one charged particle gives signal on more than one pad

The analysis on the cosmic events described in the following could improve the track-TOF signal-matching procedure performance.

In fig 5.6 and 5.7 the event used for the analysis is shown: in particular the set of TOF points on SM10 are the ones chosen to describe this study.

To better understand the aim of the analysis, we need to clarify the physical conditions of ALICE detector, in the LHC collisions environment and in the cosmic rays one. We have a tracking system consisting of ITS, TPC and TRD detectors. As said in the previous paragraph, an algorithm performs the tracks reconstruction and after having propagated the tracks outside the TPC, we can look for hit pads on the TOF array, which can be associated to the reconstructed tracks.

In the cosmic runs the situation is more clear than the LHC

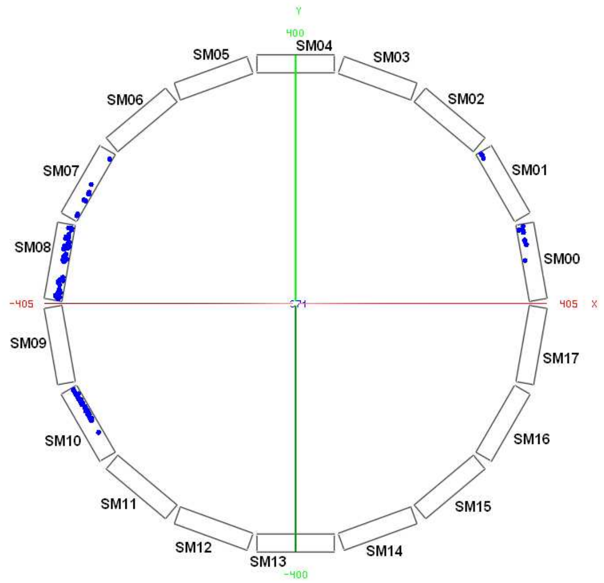

Figure 5.6: one of the events taken during the cosmic ray run of March 2008

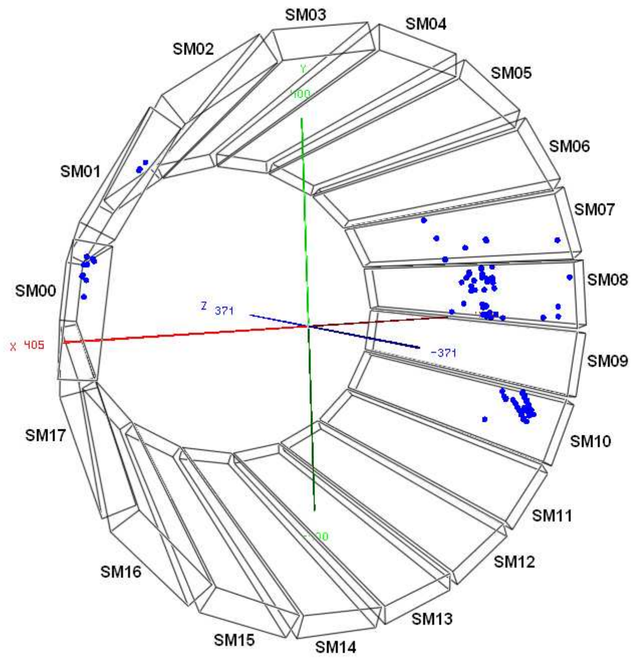

Figure 5.7: event from cosmic ray of March 2008

collisions one, because of the low rate of particles and the kind of physical phenomenon. When a cluster of fired pads is present, we can say that this cluster is relative to one track. In fig 5.8 the SMs installed and ready to take data during the two cosmic rays runs are shown; apparently the TOF configuration was not so propitious (especially during the December run), because of the SMs' positions respect to the ACORDE trigger surface (see fig 5.4) and beacuse of the missing TPC detector. Looking at several triggered cosmic events, some alligned points on the TOF, that are possible to associate to muon tracks, have been found (see fig 5.9); in these cases, we can use the strips of the TOF system as a tracker and we can perform a careful analysis to introduce the TOF clusterization procedure.

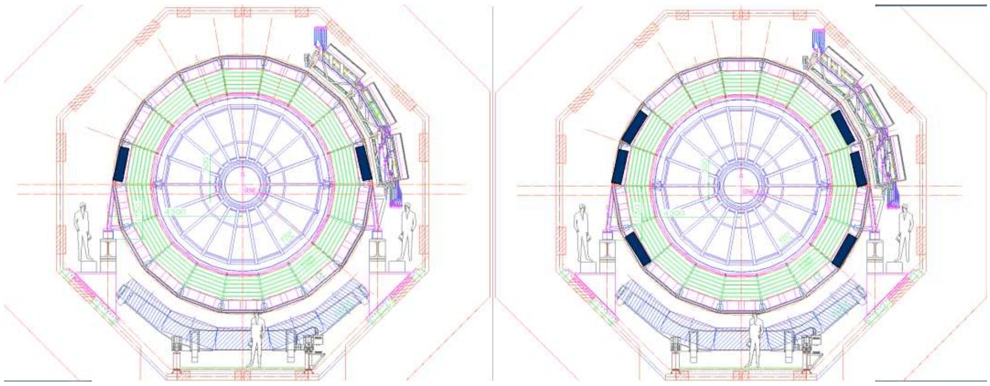

Figure 5.8: SMs present during the cosmic rays runs of December 2007 (left) and February-March 2008 (right)

The ALICE TOF detector is equipped with a very sophisticate fron-end and read-out electronics. In particular, each electronic channel is able to measure the time-of-flight, i.e. the leading edge, and the time-over-threshold (*tot*) for each signal. As just said in §3.2.1, the *tot* measurement is strictly related to the charge of the electronic signal (see figg 3.7, 3.8, 3.9). And the charge collected by each pad interested by the same event is related to the position of the event on the strip pad (see fig 2.25 in [81]).

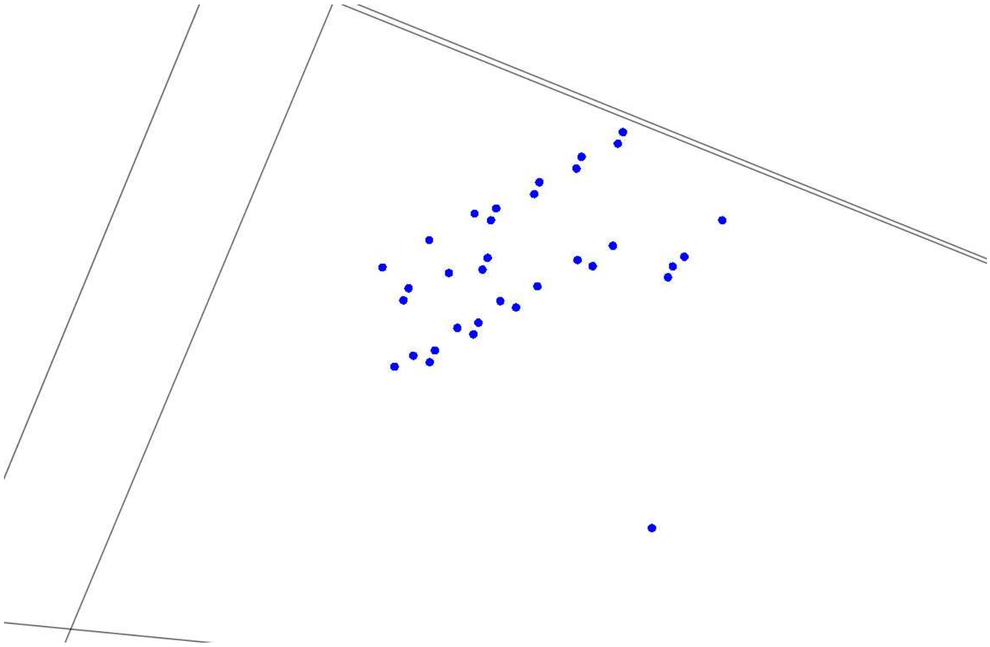

Figure 5.9: TOF digits for one cosmic rays event during the Februray-March 2008run

Let us consider:

- n, the number of pads (on one strip) interested by the same event;
- q_i, the *tot* measurement of i-th pad;
- t_i, the tof measurement of i-th pad;
- $(x_i,\ y_i,\ z_i)$, the coordinates of the i-th pad in the ALICE reference frame;

then, the position of the event can be found as the mean of the hit pad positions weighted by the *tot* measurement, as shown in the following formula:

$$(< x >, < y >, < z >) = \frac{\sum_{i=1}^{n}(x_i, y_i, z_i) \times q_i}{\sum_{i=1}^{n} q_i} \tag{5.1}$$

and similarly for the *tof* measurement of the event:

$$< t >= \frac{\sum_{i=1}^{n} t_i \times q_i}{\sum_{i=1}^{n} q_i}. \tag{5.2}$$

The following measurements set [x_i, y_i, z_i, q_i, t_i] is called TOF digit, while [<x>, <y>, <z>, <t>] is called TOF cluster.

Now, it has to be defined an algorithm to evaluate the better method to associate TOF signals (digits or clusters) to the reconstructed tracks.

Let it be:

- N, the number of the TOF strips interested by signals consistent with a straight line;
- $n(j)$, the number of TOF digits on the j-th strip;
- $q_i(j)$, the i-th *tot* measurement on the j-th strip;
- $(x_i(j), y_i(j), z_i(j))$, the i-th pad coordinates of the j-th strip in the ALICE reference frame;
- (<x>(j), <y>(j), <z>(j)), the position cluster found on the j-th strip, according to the weighted mean procedure described in eq.5.1[2].

Now we consider the TOF signals coming from N-1 strips; for each set of TOF informations, i.e. digits and clusters, let's fit to a 3D straight line and propagate each fitted line till the plane of the N-th strip.

Let's call:

- $P_D \equiv (x_D, y_D, z_D)$ the intersection point coordinates for $\sum_{j=1}^{N-1}$n(j) TOF digits fitted line with the plane of the N-th strip (if it exists);

[2] <t>(j) is the *tof* cluster found on the j-th strip

- $P_C \equiv (x_C, y_C, z_C)$ the intersection point coordinates for N-1 TOF clusters fitted line with the plane of the N-th strip (if it exists);
- $P_N \equiv (<x>(N), <y>(N), <z>(N))$ the TOF cluster position on the N-th strip.

A good parameter chosen to validate the clusterization method is the minimum between the distances (P_D,P_N) and (P_C,P_N):

$$\min(|P_D - P_N|, |P_C - P_N|) \tag{5.3}$$

5.3.1 Analysis

In fig 5.9 the TOF digits of the event taken into account are shown. We can note clearly at least two set of points distributed along two different (quasi parallel) straight lines: in fig 5.10 the same event of fig 5.9 is shown, with two boxes to point out the TOF digit sets we have taken into account in our analysis. Let's choose the TOF digit set with " A" label in the fig 5.10. In this case, the number of the strips reasonably crossed by a muon track is N=6 and the number of digits per each strip is n=(2,2,2,3,1,1). Let's chose the TOF digits on the first 5 strips, starting from the upper corner on the right, in order to fit a 3D straight line.

In fig 5.11 the TOF digit fit is shown; the green points are the digits involved in the fit, while the blue points ones are the digits not taken into account.

The same is shown in fig 5.12, where also the pads correspondings to the digits are shown, in order to have a first idea of the distance of the intersection point of the fitting line with the pad from the center of the pad. In fig 5.13 a detail of the fig 5.12 on the TOF digit of the 6-th strip is shown: the crossing of the fitted line on the hit pad is clear.

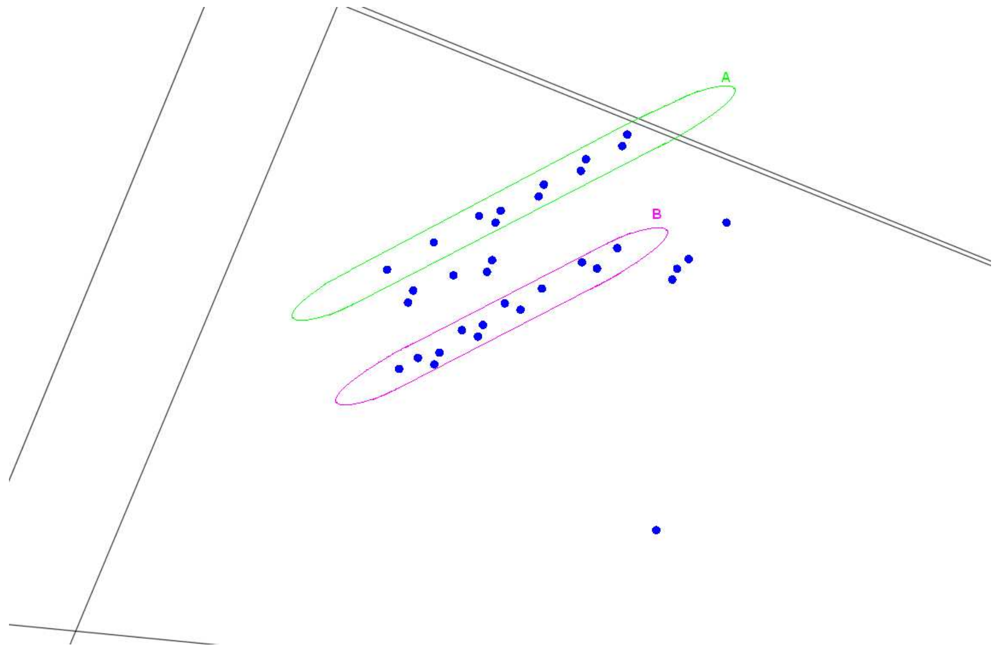

Figure 5.10: TOF digits for one cosmic rays event during the Februray-March 2008run chosen for the analysis

In fig 5.14 the TOF clusters obtained with the clusterization procedure described in the previous paragraph are shown as red crosses together with the related TOF digits (blue points)

In fig 5.15 the TOF cluster fit is shown: as in fig 5.14, the green points are the clusters involved in the fit and the red crosses are the clusters of the event. As fig 5.12, in fig 5.16 the TOF pads are also shown and a detail on the 6-th strip is shown in fig 5.17. In the fig 5.15, 5.16 and 5.17 the same is showed for the case of the fit performed using the new class with the weighted mean.

Now we can compare the results. In fig 5.18 the fit results are shown with the TOF hit pads: in purple the fit line of the TOF clusters, in orange the fit line of the TOF digits and, as usual, the green boxes are the TOF hit pads. In fig 5.19 a detail of the fig 5.18 on the 6-th strip (the one not taken into account for the fit) is shown: the centre of the hit pad is marked by black. It is

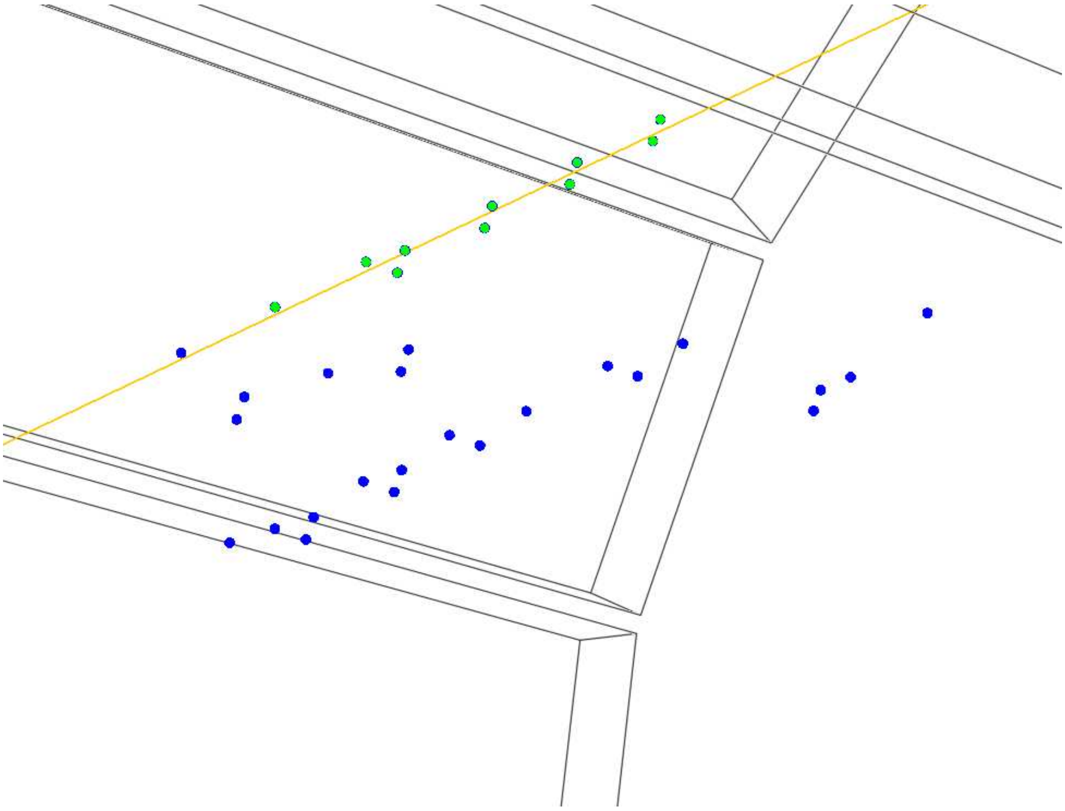

Figure 5.11: fit of the digits

cleraly visible that the purple line crosses the hit pad closer to the pad centre than the orange line. This qualitative estimation is confirmed by the numerical results of the algorithm that we implemented in eq (5.3):

$|P_D$-$P_N|$=9.1 mm; $|P_D$-$P_N|$=6.9 mm

$$\Rightarrow \min(|P_D - P_N|, |P_D - P_N|) = 6.9 \text{ mm}$$

We repeated the same analysis on the TOF digit set labelled as " B" in the fig 5.10

In fig 5.20 are shown the TOF digits (blue points), the TOF clusters (red crosses), the hit pads (green boxes) and the fit lines for TOF clusters (purple) and TOF digits (orange). In the fig

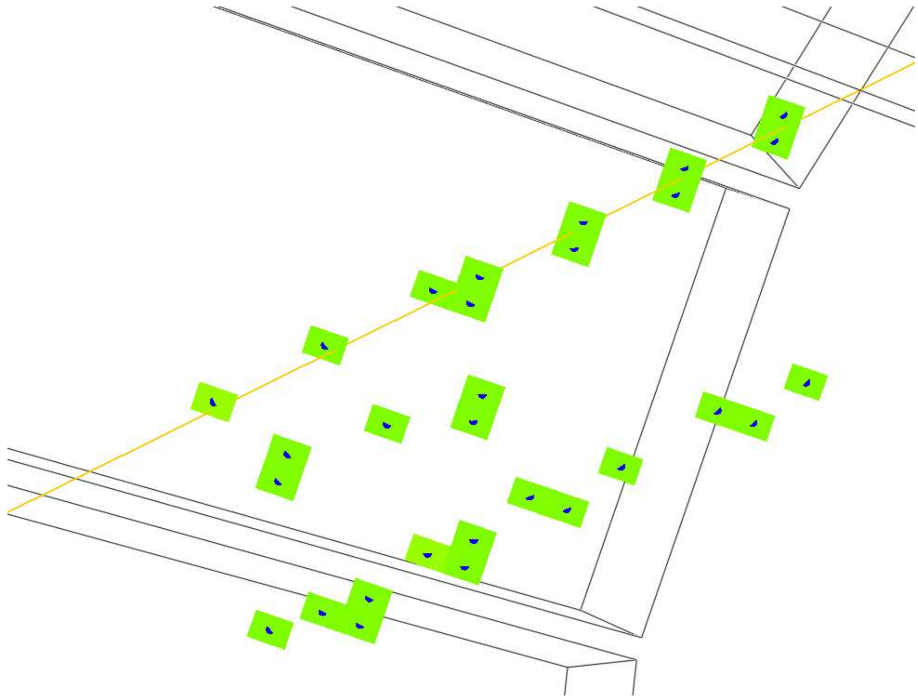

Figure 5.12: fit of the digits and the pads corresponding to the digits

5.21 a detail of fig 5.20 is shown: it is clear that the purple line crosses the hit pad, while the orange one doesn't.

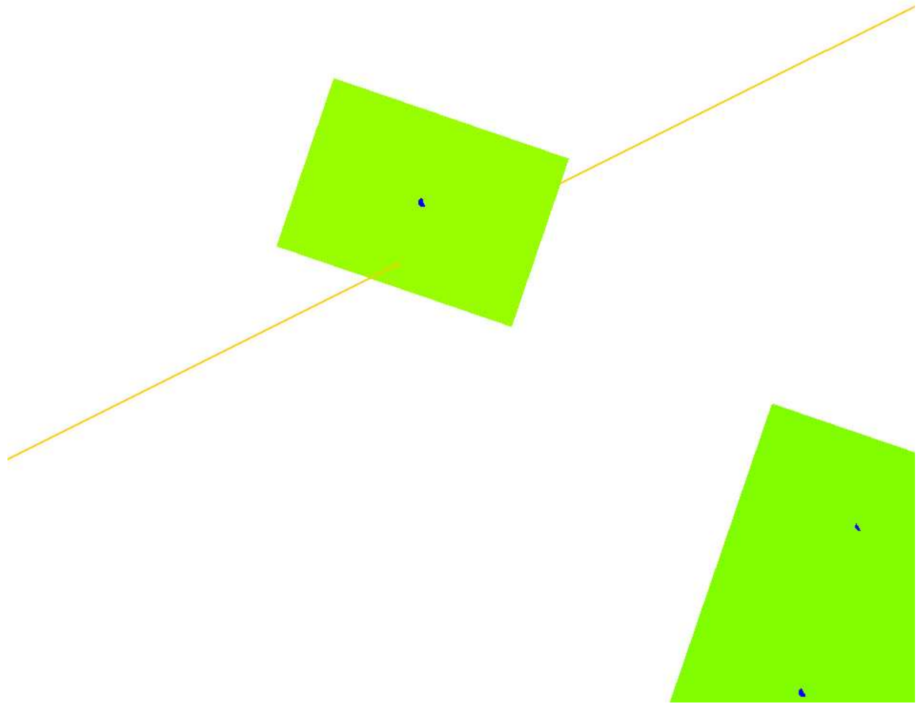

Figure 5.13: a detail of fig 5.12 on the TOF digit of the 6-th strip

5.4 Conclusion

This study has been performed on two muon tracks and in these two cases the result is an improvement of the reconstruction using the weighted mean; as well as having a smaller distance between the center of the pad and the intersection point of the fitting line with the plane of the pads, it is possible to note that the propagation of the fitting line intersects the pad only in the analysis done with the weighted mean. Obviously the behaviour is not always this one and the study has not been performed with a big statistics, but the result obtained gives an indication of the possible improvement of the tracking reconstruction, introducing the method of the weighted mean in the step of the propagation of the tracks on the TOF system.

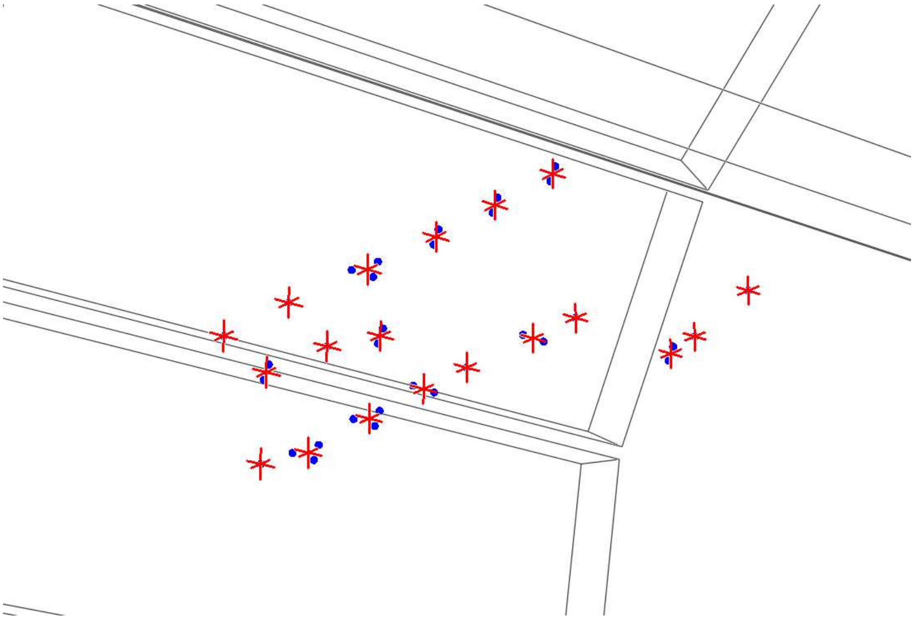

Figure 5.14: TOF digits and TOF clusters obtained with the clusterization procedure

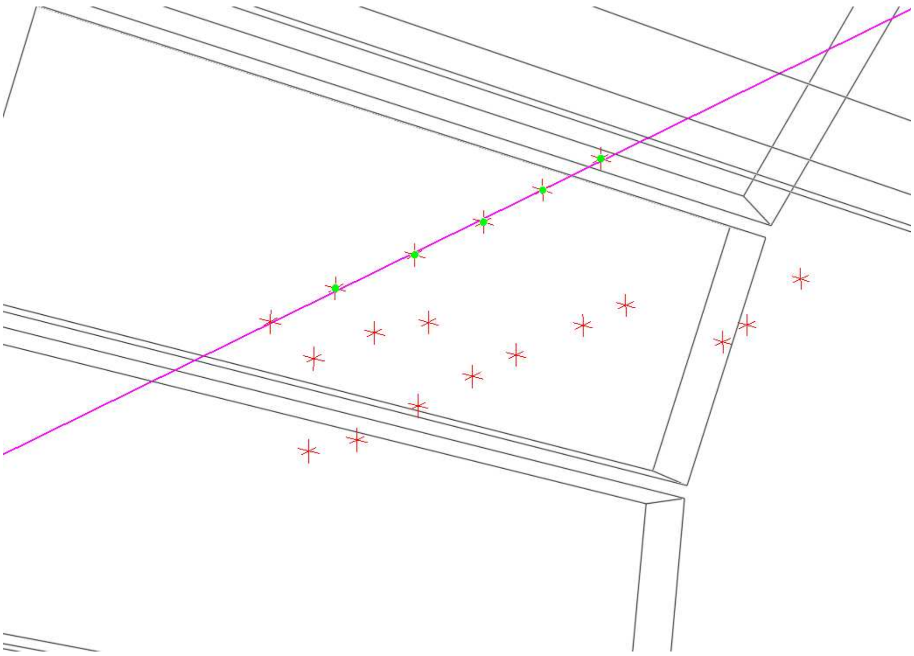

Figure 5.15: fit of the clusters

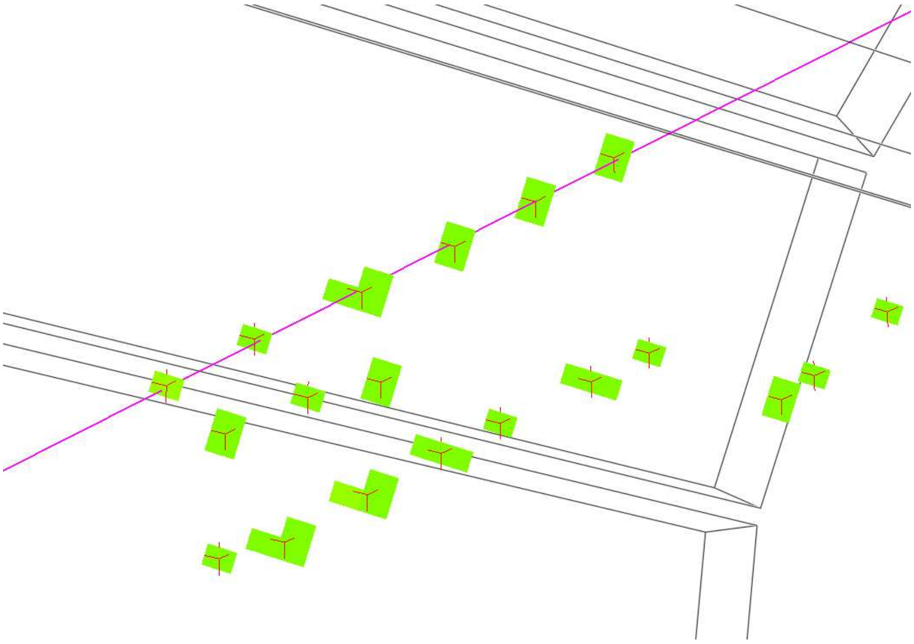

Figure 5.16: fit of the clusters and the pads corresponding to the digits

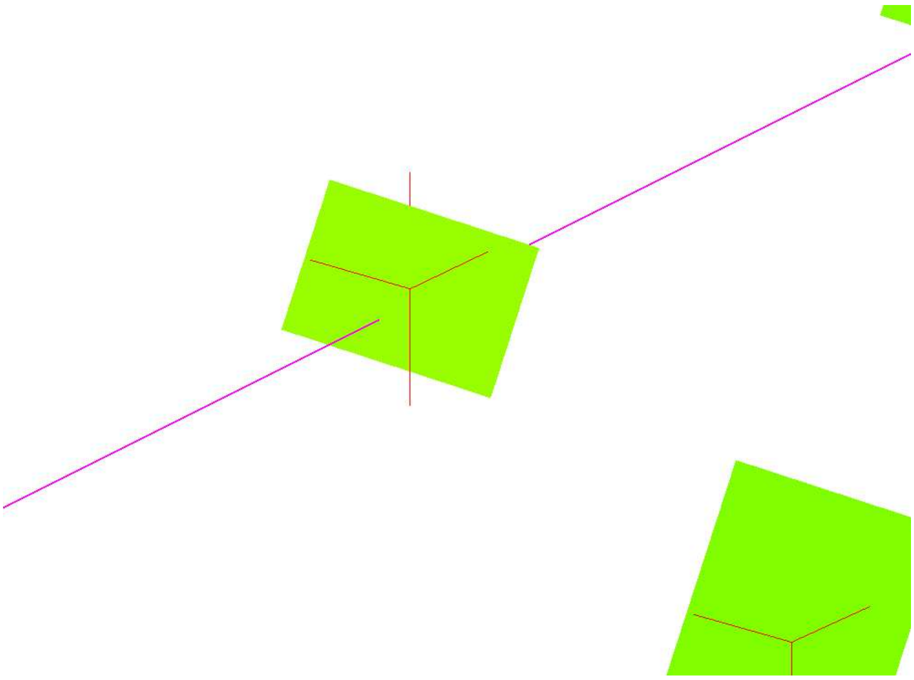

Figure 5.17: a detail of fig 5.16

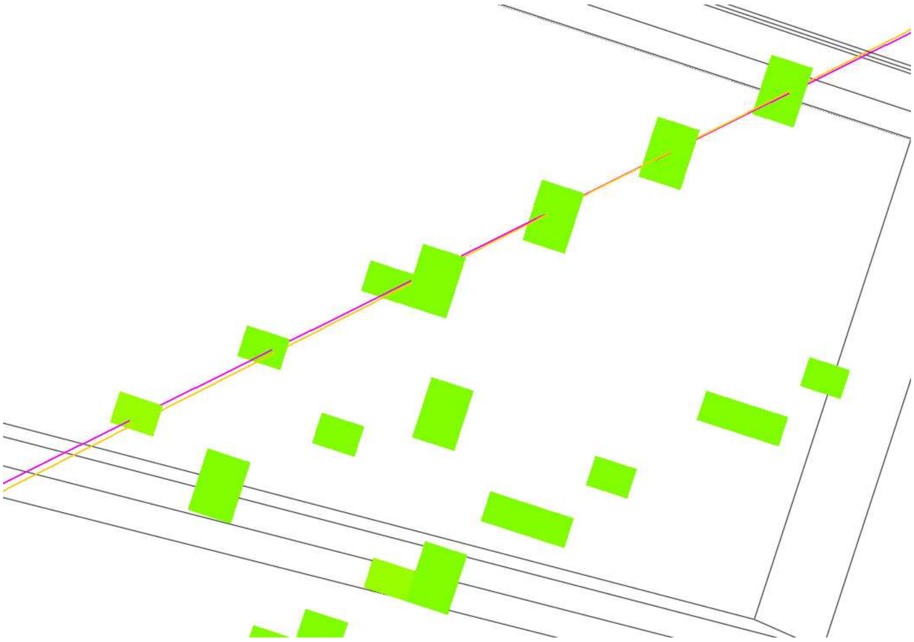

Figure 5.18: comparison between the fit line of TOF clusters and TOF digits

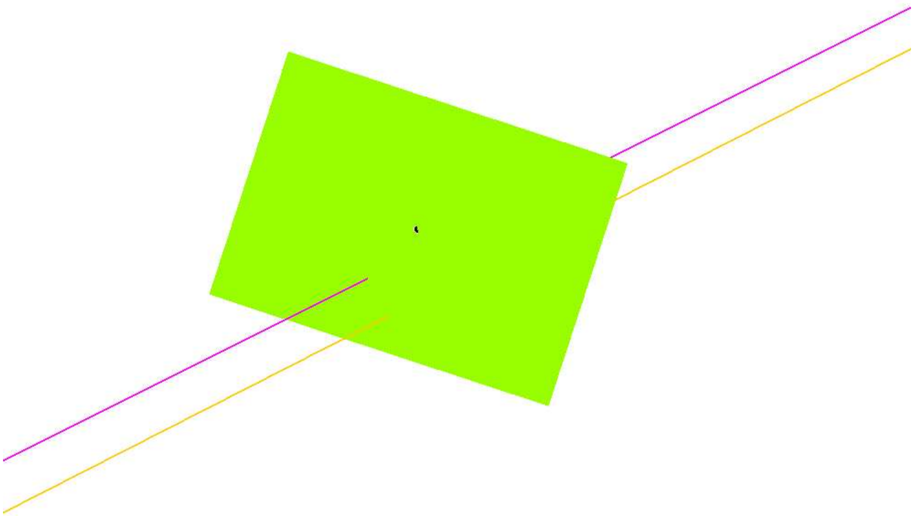

Figure 5.19: a detail of fig 5.18

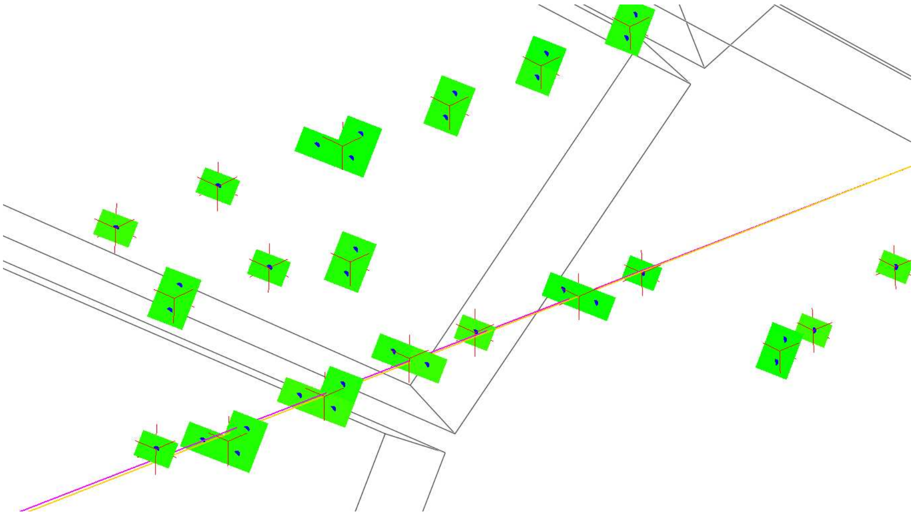

Figure 5.20: comparison between the fitting line for TOF clusters and TOF digits

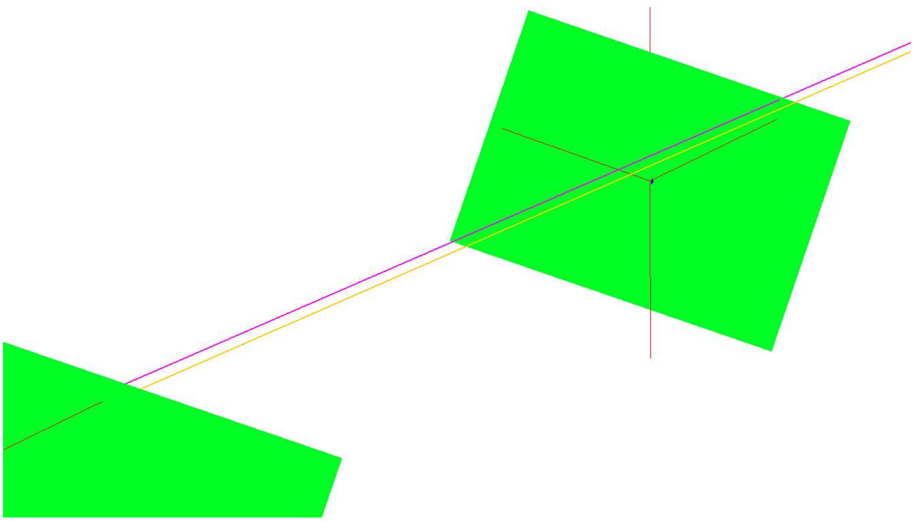

Figure 5.21: a detail of fig 5.20

Appendix A

Macro for the fit performed with the method of the weighted mean

It is important to compare the two fits in order to know if the new method introduced in the Aliroot class is useful to improve the reconstruction. For this it is necessary to calculate the distance between the intersection of the propagation of the fitting line with the pad and the center of the pad not involved in the fit; obviously, if this distance is smaller in the case of the fit performed using the weighted mean, the new method is useful for our aim. A macro has been written in order to do this operation: the equation of a line is needed to indentify the fitting line and the equation of a plane is needed to identify the exact position of the fired pad respect to the fitting line. The macro is showed in the following. The equation of the plane is calculated in this way: after having done a draw of the strip, the center of three pads (over the 96) that represent the three point defining a plane are identified (in particular the chosen pads are (0,0) (0,1) and (47,0). In fig A.1 the order of the software numbering of the pads in a strip is showed.

The macro contains the method “ distance” to calculate the distance from the center of the pad to the intersection point of

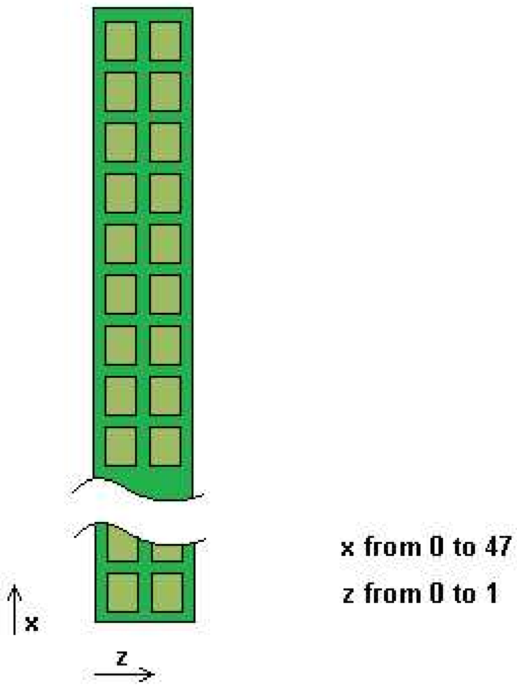

Figure A.1: numbering of the pads inside a strip

the fitting line with the plane of the strip.

In the fig A.4, A.3, A.2 the methods of the macro to calculate the distance between the center of the pad and the intersection point of the fitting line with the pad is showed. In the first one, the parameters of the fitting line (intercept and angular coefficient) are assigned and the equation of a line is written. The methods " IntersezioneRettaPiano " and " Distance" find the equation of a plane for three points (that are three pads of a strip and in particular the first two pads and the last one, using the pad numbering of the software chain) and calculate the distance center of the pad - intersection point of the line with the plane of the pad.

```
Double_t Distance(Double_t *intersectionPoint, Float_t *posPad)
{

  Double_t dummy = (intersectionPoint[0] - posPad[0])*(intersectionPoint[0] - posPad[0]);
  dummy += (intersectionPoint[1] - posPad[1])*(intersectionPoint[1] - posPad[1]);
  dummy += (intersectionPoint[2] - posPad[2])*(intersectionPoint[2] - posPad[2]);

  return TMath::Sqrt(dummy);

}
```

Figure A.2: method "Distance"

```
 Double_t intersectionPoint[3] = {0., 0., 0.};

 IntersezioneRettaPiano(intersectionPoint, point1, point2, point3, y0, Ay, z0, Az);
 /*
 printf("\n");
 for (Int_t ii=0; ii<3; ii++) printf(" %f ", intersectionPoint[ii]);
 printf("\n");
 */

 Float_t pointPad[3];
 vol[3] = iPadZ; vol[4] = iPadX;
 tofGeom->GetPosPar(vol, pointPad);

  Double_t distance = Distance(intersectionPoint, pointPad);

  return distance;

}


void IntersezioneRettaPiano(Double_t *intersectionPoint,
                            Float_t *point1, Float_t *point2, Float_t *point3,
                            Double_t y0, Double_t Ay, Double_t z0, Double_t Az)
{
  /*
  printf("\n");
  for (Int_t ii=0; ii<3; ii++) printf(" %f ", point1[ii]);
  printf("\n");
  for (Int_t ii=0; ii<3; ii++) printf(" %f ", point2[ii]);
  printf("\n");
  for (Int_t ii=0; ii<3; ii++) printf(" %f ", point3[ii]);
  printf("\n");
  */
  Double_t aa = (
                (point2[1] - point1[1])*(point3[2] - point1[2]) - (point3[1] - point1[1])*(point2[2] - point1[2])
                );
  Double_t bb = (
                (point2[0] - point1[0])*(point3[2] - point1[2]) - (point3[0] - point1[0])*(point2[2] - point1[2])
                );
  Double_t cc = (
                (point2[0] - point1[0])*(point3[1] - point1[1]) - (point3[0] - point1[0])*(point2[1] - point1[1])
                );
  /*
  printf("  aa = %f\n", aa);
  printf("  bb = %f\n", bb);
  printf("  cc = %f\n", cc);
  */

  /*
    Sistema di equazioni:
   (x - point1[0])*aa - (y - point1[1])*bb + (z - point1[2])*cc = 0.; // piano


   y = y0 + Ay*x; // inizio retta...
   z = z0 + Az*x; // ...fine retta
   (x - point1[0])*aa - (y0 + Ay*x - point1[1])*bb + (z0 + Az*x - point1[2])*cc = 0.;

   (aa - Ay*bb + Az*cc)*x - (point1[0]*aa + (y0 - point1[1])*bb - (z0 - point1[2])*cc) = 0.;
  */

  intersectionPoint[0] = (point1[0]*aa + (y0 - point1[1])*bb - (z0 - point1[2])*cc) / (aa - Ay*bb + Az*cc);
  intersectionPoint[1] = y0 + Ay*intersectionPoint[0];
  intersectionPoint[2] = z0 + Az*intersectionPoint[0];

}
```

Figure A.3: method " IntersezioneRettaPiano "

```
#if !defined(__CINT__) || defined(__MAKECINT__)

//c++ include file
#include "Riostream.h"

// root include files
#include "TMath.h"

// AliROOT include files

// TOF in AliROOT: include files
#include "AliTOFGeometry.h"

#else

#endif

Double_t parametroDiMinimo(Int_t *vol, Double_t *parameters);

Double_t parametroDiMinimo(Int_t iSector=10, Int_t iPlate=4, Int_t iStrip=12, Int_t iPadZ=1, Int_t iPadX=16,
                           Double_t y0=-659.336267, Double_t Ay=-1.452458,
                           Double_t z0=-1026.929802, Double_t Az=-2.142748);

void IntersezioneRettaPiano(Double_t *intersectionPoint,
                            Float_t *point1, Float_t *point2, Float_t *point3,
                            Double_t y0, Double_t Ay, Double_t z0, Double_t Az);

Double_t Distance(Double_t *intersectionPoint, Float_t *posPad);

//___________________________________________________________________

Double_t parametroDiMinimo(Int_t *vol, Double_t *parameters)
{
  parametroDiMinimo(vol[0], vol[1], vol[2], vol[3], vol[4],
                    parameters[0], parameters[1], parameters[2], parameters[3]);

}

Double_t parametroDiMinimo(Int_t iSector, Int_t iPlate, Int_t iStrip, Int_t iPadZ, Int_t iPadX,
                           Double_t y0, Double_t Ay, Double_t z0, Double_t Az)
{

  AliTOFGeometry *tofGeom = new AliTOFGeometry();

  Float_t point1[3] = {0., 0., 0.};
  Float_t point2[3] = {0., 0., 0.};
  Float_t point3[3] = {0., 0., 0.};

  Int_t vol[5] = {iSector, iPlate, iStrip, 0, 0};
  tofGeom->GetPosPar(vol, point1);
  vol[4] = 47;
  tofGeom->GetPosPar(vol, point2);
  vol[3] = 1; vol[4] = 0;
  tofGeom->GetPosPar(vol, point3);
  /*
  printf("\n");
  for (Int_t ii=0; ii<3; ii++) printf(" %f ", point1[ii]);
  printf("\n");
  for (Int_t ii=0; ii<3; ii++) printf(" %f ", point2[ii]);
  printf("\n");
  for (Int_t ii=0; ii<3; ii++) printf(" %f ", point3[ii]);
  printf("\n");
  */
```

Figure A.4: method to write the equation of a line

Bibliography

[1] A.S. Khvorostukhin, *LatticeQCD contraints on the nuclear equation of state*, Eur. Phys. J.,C48 (2006) 531-543

[2] F. Karsch and E. Laermann *Thermodynamics and in-medium hadron properties from lattice QCD in Quark-Gluon Plasma 3* World Scinetific Singapore (2004) 1

[3] A.D. Linde *Infrared problem in the thermodynamics of the Yang-Mills gas* Phys. Lett. B96 (1980) 289

[4] P. Arnold and C.-X.Zhai *Three loop free energy for pure gage QCD* Phys. Rev. D50 (1994) 7603

[5] C.-X. Zhai and B. Kastening *Renormalization group summation and the free energy of hot QCD* Phys. Rev. D52 (1995) 7232

[6] E. Braaten and R. Pisarsk*Damping rate of a scalar particle in hot scalar QED* Nucl. Phys. B 337 (1990) 569

[7] F. Karsch and E. Laermann*Susceptibilities, the specific heat, and a cumulant in two-flavor QCD* Phys. Rev. D 50 (1994) 6954

[8] T. Renk , R. A. Schneider , and W. Weise *QCD Thermo dynamics and Fireball Evolution in URHICs* arXiv: hep-ph/0202079v1 (2002)

[9] G. Odyniec *Quark Gluon Plasma - Recent Advances* Int.J.Mod.Phys. A17 (2002) 3107-3122

[10] P.V. Ruuskanen *Photons and lepton pairs: the deep probes of quark-gluon plasma* Particle Production in Highly Excited Matter, NATO ASI Series, Series B:Physics Vol. 303 (1992)

[11] R. Hagedorn, Nuovo Cim. Suppl. 3 (1965) 147

[12] F. Becattini and U. Heinz, Z. Phys. C 76 (1997) 269

[13] J. Rafelsky and B. Muller, Phys. Rev.Lett. 48 (1982) 1066

[14] J. Rafelsky, Phys. Rept. 88 (1982) 331

[15] S. A Bass *QGP theory: Status and Perspectives* Pramana J. of Phys. Vol. 60 4 (2003) 593-612

[16] D. d'Enterria, arXiv: nucl-ex/0302016

[17] L. Van Hove, Phys., Lett. B118 (1982) 138, L. Van Hove, Z. Phys. c21 (1983) 93

[18] J. Kapustra, et al., Phys. Lett. B163 (1985) 253

[19] H. Von Gerdsorff, Nucl. Phys. A461 (1987) 251c

[20] PHENIX Collaboration et al., Phys. Rev. C69 (2004) 034909

[21] WA97 Collaboration, F.Antinori et al., Eur. Phys. J. C14 (2000) 633

[22] R.S. Fries, B. Muller, D.K. Srivastava, Phys. Rev. Lett. 90 (2003) 132301

[23] B.G. Zakharov, JETP Lett. 80 (2004) 1

[24] J.K. Apusta, P. Lichard, D. Seibert, Phys. Rev. D44 (1991) 2774

[25] C. Song Phys. Rev. C47 (1993) 2861

[26] D.K. Srivastava, B. Sinha, M Gyulassy and X.N. Wang, Phys. Lett. B276 (1992) 285

[27] S. Chakrabarty, J. Alam, S. Raha, B. Sinha and D.K. Srivastava, Phys. Rev. D46 (1992) 3802

[28] K. Adeox ey al., Nucl. Instrum. Meth A499 (2003) 469

[29] S.S. Adler et al., Phys. Rev. Lett. 94 (2005) 232301

[30] M.L. Mangano *Phenomenology of Quarkonium production in hadronic collisions* hep-ph/9507353

[31] R. Vogt, Phys. Rep. 310 (1999) 197

[32] J.P.Blaizot, J.Y.Ollitault, Phys. Rev. Lett. 77 (1996) 1703

[33] M. Wisocky *J/ψ suppression in the QGP* Journal of Physics, G. Nucl. Part. Phys. 31 (2005) S291-S295

[34] S.Gupta and H.Satz, Phys. Lett. B283 (1992) 439

[35] J. Cleymans and R.L.Thews, Z.Phys. C45 (1990) 391

[36] T.Matsui and H.Satz, Phys. Lett. B178 (1986) 416

[37] R.L. Thews and M.L. Mangano, Phys. Rev. C73 (2006) 014904

[38] L. Grandchamp and R. Rapp, Phys. Lett. B523 (2001) 60

[39] A.Andronic et al., Phys. Lett. B571 (2003) 36

[40] A.M. Rossi et al.,Nucl. Phys. B84 (1975) 269

[41] T.Alexopoulos et al., Phys. Rev. D48 (1993) 984

[42] STAR Collaboration C. Adler et al., Phys. Lett. B595 (2004) 143

[43] J. Rafelsky, Phys. Rep. 88 (1982) 331

[44] WA97 Collaboration E.Andersen et al., Phys. Rev. B449 (1999) 401

[45] STAR Collaboration C.Adler et al., Phys. Rev. Lett. 90 (2003) 082302

[46] STAR Collaboration J.Adams, Phys. Rev. Lett. 91 (2003) 072304

[47] STAR Collaboration J.Adams, Phys. Rev. Lett. 93 (2004) 252301

[48] O.Ollitrault, Phys. Rev. D46, 229 (1992)

[49] H.Sorge, Phys. Rev. Lett, 82 (1999) 2048

[50] P.F.Kolb, J.Solfrank and U.Heinz, Phys. Rev. C62 (2000) 054909

[51] PHENIX Collaboration S.S. Adams et al., Phys. Rev. Lett. 91 (2003) 182301

[52] P.Huovinen, P.Kolb, U.Heinz, P.V.Ruuskanen and A.S.Voloshin, Phys. Lett. B503 (2001) 58

[53] STAR Collaboration J.Adams, Phys. Rev. Lett. 92 (2004) 052302

[54] F. Gastineau and J. Aichelin *Hanbury Brown Twiss correlation functions from event generators:A reliable approach to determine the size of the emitting source in ultrarelativistic heavy ion collisions?* PHYSICAL REVIEW C, VOLUME 65, 014901

[55] G.Goldhaber, S.Goldhaber, W.Lee and A.Pais, Phys. Rev. 120 (1960) 300

[56] U.Heinz and B.V.Jacak, Ann. Rev. Nucl. Part. Sci. 49 (1999) 529

[57] S.Pratt, Phys. Rev. D33 (1986) 1314

[58] U.Heinz, B.Tomasik, U.A.Wiedeman and Y.F.Wu, Phys. Rev. Lett. B382 (1996) 181

[59] P.Huovinen, P.Kolb, U.Heinz,P.V.Ruuskanen and A.S.Voloshin, Phys. Lett. B503 (2001) 58

[60] V.S.Pantuev *Evidence of finite sQGP formation time at RHIC* arXiv:hep-ph/0604268 v1

[61] E.Shuryak *Toward the theory of strongly coupled Quark-Gluon Plasma (sQGP)* and references therein

[62] PHENIX Collaboration K.Adcox et al., Phys. Rev. Lett. 88 (2002)022301

[63] M.Harrison, T.Ludlam and S.Ozaki, Nucl. Instrum. Meth.A499 (2003) 235

[64] K.M.Potter, LHC Project Report 36 (1996) and references therein

[65] N.Armesto and C.Pajares, Int. J. Mod. Phys. A15 (2000) 2019

[66] K.J.Eskola, P.V.Ruuskanen, S.S.Rasanen and K.Tuominen, Nucl. Phys. B570 (2000) 379

[67] M.Nardi J.Physics Conf. Ser. 5 (2005) 148

[68] M.Bejidian et al., CERN Yellow Book of the Workshop Hard Probes of Heavy Ion Collisions at the LHC (2003) hep-ph/0311048

[69] B.Mohanty and J.Serrean, Phys. Rept. 414 (2005) 263

[70] E. Badura et al. *Pestov Spark Counter prototype development for the CERN-LHC ALICE experiment* Nucl. Inst. and Meth. A372 (1996) 352-353

[71] ALICE Collaboration *Time of Flight system, Technical Design Report* CERN/LHCC 2000-012 ALICE TDR 8 (2000)

[72] M.Mota, J.Christiansen, S.Debieux, V.Ryjov, P.Moreira, A.Marchioro *A flexible multi-channel high resolution time-to-digital converter ASIC* IEEE Nuclear Science Symposium (2000)

[73] A.Alice, P.Antonioli, A.Mati, S.Meneghini, M.Pieracci, M.Ricci and C.Tintori *Radiation tests of key components of the ALICE TOF TDC Readout Module*

[74] L.Colombioni, M.Lippi, A.Mati, G.Passuello, S.Pietrucci, M.Pieracci, G.Selmi and C.Tintori *Compact data acquisition and power supply system designed for hostile environment condition concerning radiation and magnetic field* and references therein

[75] A.Alici, G.Cara Romeo, Jinsook Kim, D.Hatzifotiadou, Y.Sun, G.Valenti, M.C.S.Williams, D.Yakorev, A.Zichichi *Aging and rate effects of the Multigap RPC studied at the Gamma Irradiation Facility at CERN* Nucl. Instr. and Meth. in Physics Research A 579 (2007) 979-988

[76] A.Akindinov et al., Nucl. Phys. B158 (2006) 78-82

[77] L.Colombioni, M.Lippi, A.Mati, G.Passuello, S.Pietrucci, M.Pieracci, G.Selmi and C.Tintori Sep. 2005, prepared for 11th Workshop on Electronics for LHC and Future Experiments (LECC2005), Heidelberg, Germany 12-16 september 2005

[78] ALICE DAQ Project, ALICE DAQ and ECS user's guide ALICE-INT-2005-015

[79] R.Brun et al., ROOT user's guide 5.16, http://root.cern.ch

[80] P. Billoir, Nucl. Instrum. Meth. A255 (1984) 352/ P. Billoir et al., Nucl. Instrum. Meth. A241 (1984) 115/ P. Billoir, Comut. Phys.Commun. 57 (1989) 390/ R.Fruhwirth, Nucl. Instrum. Meth. A262 (1987) 444

[81] ALICE Collaboration *Time of Flight system, Addendum to the Technical Design Report* CERN/LHCC Addendum to ALICE TDR 8 (2002)

[82] ALICE Collaboration *ALICE: Physics Performance Report, Vol. II* Journal of Physics G:Nuclear and Particle Physics 32 (2006) 1295-2040